Engineering Tunable Strain in 2D Materials and their Device Heterostructures

Jordan Fonseca

A dissertation

submitted in partial fulfillment of the

requirements for the degree of

Doctor of Philosophy

University of Washington

2024

Reading Committee:

Xiaodong Xu, Chair
Jiun-Haw Chu
David Cobden

Program Authorized to Offer Degree:

Physics

University of Washington

Abstract

Engineering Tunable Strain in 2D Materials and their Device Heterostructures

Jordan Fonseca

Chair of the Supervisory Committee:
Professor Xiaodong Xu
Department of Physics

In the past 20 years, 2D van der Waals materials have garnered broad interest across a wide range of scientific and engineering disciplines. They provide a highly tunable platform for exploring emergent quantum phenomena in solid state systems. Their low defect density, atomic thickness, and high surface-to-volume ratio make them stand out in two ways in particular:

First, their charge carrier density can be tuned dramatically with only an electrostatic gate. Moiré superlattices formed by stacking 2D crystals with either a twist angle or lattice mismatch have provided a highly tunable platform for exploring remarkably rich physical phenomena. Since the moiré pattern arises from interfering lattices, its wavelength and symmetry are highly sensitive to the effects of strain, which modifies the lattice parameters of the constituent layers. The combination of a large, experimentally tunable “superlattice” constant and the ability to fine-tune the carrier density in a single device at cryogenic temperatures provide unprecedented control over

the electronic environment and have made gated moiré systems one of the most promising material platforms for exploring and simulating the physics of strongly correlated 2D electron systems.

Second, 2D materials can be stretched, bent, and compressed more than bulk materials before they yield. Due to their remarkable strength, one particularly enticing tuning knob is strain since the ability to break rotational symmetries and change interatomic spacing both have significant implications for nearly all material properties that are rooted in the multi-orbital makeup of band structure and the crystal symmetries that underlie the tensors governing essentially all material properties. Despite the importance and potential for strain in tuning moiré systems, there have been limited experimental investigations utilizing *in-situ* strain control to date, not mentioning gated device geometry.

In this dissertation, I tackle the challenge of simultaneously implementing *cryogenic, tunable* uniaxial strain in a high-quality, gated moiré superlattice. After establishing optical techniques as a probe of crystal symmetries in Chapter 2 and exploring how localized, out-of-plane strain pulses generated by an ultrafast laser can be used to perturb and probe material properties in 2D van der Waals crystals in Chapter 3, the following three chapters build on each other sequentially.

In Chapter 4, I directly image the effects of applying uniaxial stress to an exposed WS_2/WSe_2 moiré superlattice with piezoresponse force microscopy (PFM). I use a combination of basic FFT analysis as well as an implementation of Geometric Phase Analysis (GPA) to qualitatively and quantitatively understand how this uniaxial stress strains the moiré superlattice. In Chapter 5, I report our work to address the strain transmission problem—graphene and hBN do not transmit strain from the substrate to a target layer in a functional device, requiring that we explore alternative dielectric substrates that provide an insulating, atomically flat, uniform

dielectric surface that also transmits significant strain. I show that bismuth oxy-selenite is a suitable material for this purpose that transmits ~1% uniaxial tensile strain to a gate-tunable monolayer WS_2 flake.

Finally, in Chapter 6 I unify the previous results by demonstrating the ability to fabricate high-quality, top-gated WS_2/WSe_2 moiré heterostructure devices that can be continuously, reversibly strained up to 1% at cryogenic temperatures. I report, for the first time, an interlayer exciton strain gauge factor, a splitting of the interlayer exciton into two distinct species with distinct dipole moments, optical selection rules, and gate-dependent oscillator strengths.

Contents

Contents 6
List of figures 7
Abbreviations 15
Acknowledgements 16
Publications 21
Dedication 22
Chapter 1 | Introduction 23
Chapter 1.1 | Outline of Dissertation 43
Chapter 2 | Anomalous Second Harmonic Generation from Atomically Thin $MnBi_2Te_4$ 46
Chapter 3 | Picosecond Ultrasonics in Topological Magnet $MnBi_2Te_4$ 59
Chapter 4 | Strain Tunable Moiré Geometry and Geometric Phase Analysis 78
Chapter 5 | Engineering robust strain transmission in van der Waals crystals and heterostructures 99
Chapter 6 | Cryogenic strain tuning of moiré excitons in gated WS_2/WSe_2 heterostructures 115
Appendix A | Rotational Anisotropy Fitting of $MnBi_2Te_4$ SHG 136
Appendix B | Theory of Geometric Phase Analysis 138
Appendix C | Strain-dependent PFM images and corresponding GPA matrix components 144
Appendix D | Tabulated Literature on Strained TMDs and Graphite 146
References 150

List of figures

Figure 1.1: Scotch tape exfoliation process. Bulk crystal **(a)** is peeled into thin flakes on scotch tape **(b)**, which is then pressed onto a Si/SiO_2 substrate **(c)** and peeled away **(d)**, which cleaves vdW crystals at the vdW interface **(e)**, leaving a chip covered with a variety of atomically thin flakes that can be searched with an optical microscope **(f)**. 27
Figure 1.2: Dry transfer technique for assembling vdW heterostructures. (a) A "stamp" consisting of a sticky polymer (PC or PPC) extended over a squishy polymer (PDMS) creates a gentle, controllable adhesive surface for picking up and transferring a wide variety of 2D materials. **(b)** A "transfer stage" that allows independent positioning of a substrate holder, stamp holder, and optical microscope facilitates the transfer process. **(c)** An example of a stacked heterostructure before the PC film has been removed from the final substrate. 28
Figure 1.3: Making electrical contact to 2D materials with electron beam lithography and metal evaporation. (a) Schematic side-view showing how electron beam exposure and solvent use define precise channels in a PMMA mask spin-coated over the whole device. When gold is evaporated over the whole surface and the PMMA is washed away with solvents, only the gold contacts to the 2D device remain. **(b)** Microscope image of channels left behind in PMMA after EBL. **(c)** Microscope image of finished device with metal contacts to the target flakes..... 29
Figure 1.4: Electrostatic gating of 2D materials with capacitor-like device structure. (a) Schematic of a 2D heterostructure sandwiched between stacks of insulating, dielectric hBN and conductive graphite with electrical connections to apply voltage to the top and bottom gate while keeping the sample grounded. (b) Schematic showing the change of basis from top- and bottom-gate voltages to electric field and carrier density, using Equations 1.1 and 1.2. 32
Figure 1.5: Moiré patterns around us and in 2D crystals. (a) Moiré pattern formed by a screen door showing the pattern resulting from interfering mesh screens (left) that is absent when only a single screen is present (right). **(b)** Moiré superlattice formed by a WS_2/WSe_2 heterostructure, which results from a combination of the ~4% lattice constant mismatch between the two crystals and the 4^o relative twist angle. 34
Figure 1.6: Flexibility of 2D crystalline materials. (a) Schematic of the ways that a monolayer 2D material can be deformed in myriad ways. **(b)** SEM images of 2D material rolled back on itself many times. **(c)** SEM image of 2D MoS2 wrinkling on a soft substrate. Panel (a) reproduced from ref.[68], panel (b) reproduced from ref.[69], and panel (c) reproduced from ref.[70] . All panels reproduced with permission..... 35
Figure 1.7: Fundamental aspects of strain in 2 dimensions. Depiction of **(a)** biaxial tensile, **(b)** shear, and **(c)** uniaxial tensile strains. The red dotted outline indicates the original shape, while the black outline indicates the shape after said strain is applied. **(d)** Typical stress-strain curve for a material. In the reversible, linear regime at low stress, the linear relationship between stress and strain is defined by the Young's modulus. Panel (d) reproduced from ref. [75]. 39
Figure 1.8: Commonly employed techniques to generate strain in 2D materials and 2D heterostructures. (a) A stressed film that either contracts or expands upon contact with the 2D material is applied to the exposed surface to generate compressive or tensile strain. **(b)** The sample is placed on a bendable substrate that can be deformed to create uniaxial tensile strain on the top surface. **(c)** 2D flakes are deposited over cavities and pressed with a narrow tip. **(d)**

Ultrafast laser pulses create a localized, dynamic strain pulse in a crystal that traverses the material. **(e, f)** Raised microscale structures are created that generate a specific, localized strain profile in 2D materials or heterostructures that are deposited onto these structures. Panel (a) reproduced from ref. [83]. Panel (b) reproduced from ref. [84]. Panel (c) reproduced from ref. [77]. Panel (d) reproduced from Chapter 3. Panel (e) reproduced from ref. [85]. Panel (f) reproduced from ref. [86]. All panels reproduced with permission. 41
Figure 2.1: $MnBi_2Te_4$ crystal structure and magnetic ordering. (a) $MnBi_2Te_4$ crystal structure. **(b)** Schematic showing how symmetry is preserved (broken) in odd (even) layer crystals. Red/blue arrows indicate the magnetic ground state below the Néel temperature. **(c)** Atomic force microscope image of $MnBi_2Te_4$ flakes down to a monolayer with linecut of 1 SL, 2 SL, and 3 SL steps taken along red line. Inset shows optical image of the same region. **(d)-(f)** RMCD sweeps of 1 SL, 2 SL, and 3 SL flakes measured at ~4.5 K. Magenta insets indicate $MnBi_2Te_4$ layer number measured in each plot. 48
Figure 2.2: 2 SL $MnBi_2Te_4$ magnetic field and temperature dependent SHG. (a) Polarization-resolved SHG from 2 SL $MnBi_2Te_4$ with no applied field below the Néel temperature. Black (blue) dots are co(cross)-linearly polarized experimental data with solid line fits to Eq. 1 (Eq. 2). XY data are excluded from subsequent subfigures for clarity. **(b)** Out-of-plane magnetic field dependence of the SHG. **(c)** Temperature dependence of the SHG above T_N. Magenta insets indicate $MnBi_2Te_4$ layer number measured in each plot. All data in (b) and (c) are taken at a cryostat base temperature of ~4.5 K, and only XX data are shown for clarity. 50
Figure 2.3: 1 SL & 3 SL magneto- and temperature dependent SHG. Dependence of the XX SHG on an out-of-plane magnetic field for 1 SL **(a)** and 3 SL flakes **(b)** at a base temperature of ~4.5 K. Temperature dependence of the XX SHG for 1 SL **(c)** and 3 SL **(d)** flakes above T_N. Magenta insets indicate $MnBi_2Te_4$ layer number. XY data, which exhibit the same behavior, are omitted for clarity. 51
Figure 2.4: Thickness and substrate dependence of polarization resolved SHG. Polarization-resolved SHG from **(a)** a few-layer flake on Au, **(b)** a bulk flake on Au, **(c)** a few-layer flake on SiO_2, **(d)** Bulk flake on SiO_2, **(e)** a bulk flake cleaved on Scotch tape before exfoliation, and **(f)** a pristine bulk flake oriented to have the beam incident on the (0001) surface. All data are taken at cryogenic temperature with no applied magnetic field. Black (blue) dots are co(cross)-linearly polarized experimental data with solid line fits to Eq. A.1 (Eq. A.2). 52
Figure 2.5: Comparison of SHG intensity from $MnBi_2Te_4$ and WSe_2. Polarization resolved SHG from **(a)** exfoliated bulk $MnBi_2Te_4$ and **(b)** 1L WSe_2 showing that the normalized intensity of SHG from $MnBi_2Te_4$ is approximately 3,000 times weaker than that from 1L WSe_2. All data are taken in the same experimental conditions other than excitation power, which was 850 μW in (a) and 600 μW in (b). 54
Figure 2.6: Effect of $MnBi_2Te_4$ surface degradation on SHG. Data shown in each panel taken from a different flake. Insets show a polarization resolved measurement before (blue) and after (orange) the time-dependent measurement. For the exposure time dependence, the SHG was collected at the polarization marked in the inset with a red arrow. SHG intensity decreases dramatically within the first 60 minutes following exfoliation. 56
Figure 2.7: Temperature and power dependent RMCD. (a) Temperature dependent RMCD around the central hysteresis loop for a 3 SL sample. (b) RMCD signal for the same 3 SL

measured as a function of ultrafast laser power when the SHG excitation beam is also on the sample. These data are overlapped with the RMCD data taken at 17.5 K when no ultrafast pulses were present. Below 500 μW, the local heating from the ultrafast beam does not raise the temperature of the 3 SL above its Néel temperature. 58
Figure 2.8: RMCD & SHG from a 4 SL sample. (a) RMCD from a 4 SL flake of $MnBi_2Te_4$ exfoliated on gold. **(b)** Magnetic field dependence of XX SHG from showing no change up to 3 T. **(c)** Temperature dependence of XX SHG flake showing a weak change in intensity of signal at higher temperatures, which we attribute to experimental artifacts. 59
Figure 3.1: Formation of the acoustic frequency comb. (a) Time trace of transient reflectivity as a function of delay time between pump and probe pulses showing periodic spikes in addition to the typical exponential decay. **(b)** FFT of the time trace shown in (a) highlighting the sharp comb teeth that emerge in the frequency domain. Red dashed line is a guide to the eye of the comb's gaussian envelope. **(c)** Cartoon of the strain pulse (shaded blue for tensile strain, green for compressive strain, and red for unstrained) forming at the top surface of the crystal, propagating through the material, and reflecting from the bottom interface. The thick black arrow to the right of the cartoon indicates time increasing downward. **(d)** Expanded view of a single strain pulse in time (left) and the associated FFT (right) with color shading corresponding to tensile, compressive, or zero strain as in (c), and highlighting that the individual comb teeth are lost when only a single temporal pulse is Fourier transformed. 63
Figure 3.2: Identification of vertical stacking faults from pulse timing and phase. (a) Time trace of transient reflectivity from a fault-free flake showing a single train of identically phased pulses. **(b)** Time trace of transient reflectivity from a different flake of similar thickness that hosts two sets of periodic pulse trains that are out of phase with each other and temporally offset by ~100 ps. The phase-flipped and temporally offset train of pulses arise from a partial reflection of the strain pulse off a stacking fault located 42 nm below the top surface of the crystal. **(c)** Cartoon illustration of how a stacking fault causes a partial reflection of the strain wavepacket within the crystal. Cartoon insets of (a) and (b) depict the distinct real-space pictures of how a defect causes partial reflection of the pulse within the crystal bulk. 64
Figure 3.3: Characterization of the frequency comb in $MnBi_2Te_4$ cavities. (a) Frequency comb for the data presented in **Figure *3.1***, fit with an 8-peak Lorentzian to identify the mode frequencies f and FWHM df. **(b)** Calculated quality factor ($Q = fdf$) versus frequency for each mode. **(c)** Calculated $f \times Q$ product for the same data in (b). 66
Figure 3.4: Absence of magnetostrictive coupling between cavity modes and magnetic order. (a) Time trace of transient reflectivity (black) and TR-MOKE (red) with exponential decay removed to highlight a picosecond pulse at 680 ps. **(b)** Expanded view of pulse in (a) demonstrating a negligible change in TR-MOKE concomitant with a significant change in reflectivity due to the strain pulse returning to the top surface of the crystal. **(c)** Dependence of the TR-MOKE on an external magnetic field applied along the crystal c-axis. The white dashed line emphasizes the metamagnetic transition at 3.5T that is easily identifiable from the change in sign of the MOKE signal. **(d)** FFT of the transient reflectivity as a function of magnetic field, collected simultaneously with the data in (c), showing that the comb spectrum remains unchanged across the metamagnetic transition. 68

Figure 3.5: Depiction of two explanations for additional pulse reflections. (a) Same time-trace data as in **Figure *3.2***b with origin (or absence) of strain pulses highlighted in different colors. Red arrows denote the main PU pulse that reflects off the SiO_2-$MnBi_2Te_4$ interface. Dark blue arrows denote the additional phase-flipped reflections that we attribute to a subsurface defect, and light blue arrows mark where additional pulses should appear if the subsurface defect back-reflected the top-down incident strain pulse. **(b)** Cartoon depicting two possible origins for the additional reflected signal. On the left, a subsurface defect that acts as a nearly unidirectional beamsplitter is depicted, with arrow color corresponding to panel (a). On the right, the possibility of transduction of the strain pulse through the SiO_2 substrate is shown, again with arrow color corresponding to panel (a). Reflections at interfaces that induce a 180° phase flip are shown with blue dots, while reflections at interfaces that induce no phase flip are shown with a yellow dot. 70
Figure 3.6: Determination of the speed of sound in $MnBi_2Te_4$ from Picosecond Ultrasonics. **(a, d)** Optical photographs of two $MnBi_2Te_4$ flakes used to determine the speed of sound. **(b, e)** AFM tapping mode topography of flakes measured. Inset: line cut taken at horizontal red lines in AFM image showing flake thickness. **(c, f)** Time-traces of optical reflectivity showing periodic pulses. Delay times corresponding to three phonon pulses are highlighted, with text insets showing average time delay between pulses and corresponding speed of sound $vs = 2dMBT\Delta t$. 77
Figure 4.1: In-situ imaging a strain-tunable moiré superlattice with piezoresponse force microscopy. (a) Schematic of piezoelectric strain apparatus and PI substrate. **(b)** Schematic of sample consisting of monolayer WSe_2 aligned to bulk WS_2, which is clamped to PI using gold. The sample leaves the moiré interface exposed for PFM measurements. **(c)** Optical photo of the heterostructure before Au clamping. **(d)** PFM image of the WSe_2/WS_2 superlattice with no applied strain. 84
Figure 4.2: Temperature-dependent wiring scheme for piezoelectric strainer. (a) Wiring scheme of cryogenic use of the strain cell. **(b)** Schematic of wiring scheme for room temperature use of the strain cell. **(c)** Typical butterfly-hysteresis diagram for displacement vs. applied voltage/electric field. Reproduced from ref [268]. Red arrows show the direction of displacement/expansion when a positive voltage is applied in (a) and (b). 85
Figure 4.3: Strain-dependent PFM with FFT and filtered peaks showing how moiré patter stretches under applied strain. Strain-dependent PFM data at 0V **(a)** and 75V **(d)** applied to the piezoelectric strainer. PFM data with simple data processing (line scan alignment and quadratic background subtraction) are shown in the top row. **(b)** and **(e)** are FFTs of the data shown in (a) and (d), respectively, and red pixels pick out the three most prominent peaks from the FFT. **(c)** and **(f)** show an inverse FFT of the three red peaks picked out in plots (b) and (e). 87
Figure 4.4: Expansion and rotation of the average moiré wavelength under uniaxial strain. (a) Example of how a moiré wavelength and peak angle can be extracted from the filtered FFT of each PFM image. Red and green dots are the lowest-wavelength moiré peaks corresponding to a real moiré wavelength, while the blue dot corresponds to a higher-order periodicity of the moiré wavelength resulting from the non-sinusoidal shape of the real moiré potential landscape. **(b)** Extracted moiré wavelength plotted for each strain value. **(c)** Extracted peak angle plotted for each strain value. 88

Figure 4.5: PFM image of a traditional, aligned WS_2/WSe_2 heterostructure from Heonjoon Park (UW)..... 89
Figure 4.6: GPA-generated strain matrix on a PFM of a WS_2/WSe_2 heterostructure. GPA computed ϵxx **(a)**, symmetrized ϵxy **(b)**, anti-symmetrized ωxy **(c)**, and ϵyy **(d)** revealing subtle inhomogeneities across the image in lattice strain and twist angle. All GPA images computed on the PFM image shown in **Figure 4.5**. 90
Figure 4.7: Doping-dependent photoluminescence from a dual-gated WS_2/WSe_2 device. The sharp jumps in PL intensity and energy as a function of gate voltage correspond to integer and fractional electron/hole fillings of the moiré superlattice. These data were collected from the moiré device whose moiré landscape was imaged with PFM and shown in **Figure 4.5**..... 92
Figure 4.8: Artifacts in GPA analysis of moiré images with lattice resolution. (a) HRTEM image of a WS_2/WSe_2 moiré superlattice. Adapted from: "*Atomic-Scale Insights of Exciton-Moiré Coupling in WSe_2/WS_2 Superlattices*,**"** Elizaveta Tiukalova, Yuzhou Zhao, Xiao-Wei Zhang, Rohan Mewada, Andrew R. Lupini, Jihui Yang, Di Xiao, Ting Cao, Xiaodong Xu, and Juan Carlos Idrobo, *unpublished* (2024). **(b)** Simulated WS_2/WSe_2 moiré superlattice with a 1° twist. **(c)** Different way to simulate a moiré lattice with a 1° twist. (d) GPA-calculated ϵxx for the data in (a) showing emergence of what appears to be a strain field with a rhombohedral tiling. **(e, f)** GPA-calculated $\epsilon xx + \epsilon yy$ (biaxial strain) for the simulated moiré lattices in (b) and (c), respectively reveal that the rhombohedral strain field that emerges is an artifact since the simulated lattices include no relaxation that could give rise to a real lattice strain. 94
Figure 4.9: PFM images at 3 different strains and corresponding ϵxx maps. PFM data at 0V **(a)**, 15V **(b)**, and 35V **(c)** of applied strain. **(d-f)** GPA computed ϵxx maps at each strain value. 95
Figure 4.10: Comparison of average GPA-calculated uniaxial and Poisson strain with FFT-calculated strain analysis. (a) Mean ϵxx (black dots) and ϵyy (red dots) versus applied strain voltage. Dotted purple lines serve as a guide to the eye. **(b)** Magnitude of the moiré lattice vectors from **Figure 4.4**b replotted. 96
Figure 5.1: Efficient interlayer strain transmission in van der Waals crystal CrSBr. (a) Side view of CrSBr crystal structure, consisting of monolayer planes stacked along the c axis. (**b)** Raman spectra taken on a thick (> 100 nm, optical image inset) exfoliated CrSBr flake with 0 V (blue) and 100 V (black) applied to the piezoelectric strain cell. The phonon mode shifts by ~ 6.8 cm^{-1}, corresponding to a strain of ~ 1.6 % (see **Methods**). (**c)** Measured strain as a function of piezo voltage applied to the strain cell. The thick flake shows a continuous shift with little change to the full-width at half maximum (FWHM) of the Raman peak (red). 101
Figure 5.2: High strain behavior in unclamped thin bulk CrSBr. (a) Colormap of Raman scattering from the P_3 peak as a function of piezo voltage. (**b)** Extracted peak energy obtained by fitting the spectra with Lorentzian functions. At a large strain approaching 4% (denoted by the grey line), the sample suddenly slips and the strain is released. The measurement was performed at a nominal temperature of 40 K to increase the piezo displacement and applied strain. 102
Figure 5.3: Measuring strain transmission in vdW crystals via a CrSBr strain sensor. (a) Crystal structure of hexagonal boron nitride (hBN). (**b)** Measured strain as a function of piezo voltage directly on the polyimide substrate (black) and through a thin bulk (~20-30 nm) hBN crystal. (**c-f)** Side view crystal structure and strain transmission characteristics of α-MoO_3 (**c, d**)

and Bi_2SeO_5 (**e, f**). The strain in all measurements is determined by using the calibrated Raman response of a CrSBr flake deposited on top as a sensor (**Methods**). 104
Figure 5.4: Optical images of CrSBr/hBN heterostructure before and after applying strain. Optical image of a thin bulk CrSBr flake and a CrSBr / hBN heterostructure deposited on the same polyimide substrate at 0 V before (left) and after (right) a piezo voltage of 120 V was applied to the strain cell. The hBN heterostructure demonstrates a variety of new wrinkles after strain cycling, while the CrSBr flake does not. 105
Figure 5.5: Bi_2SeO_5: a promising straintronic dielectric substrate. (a) Schematic of top-gated strain tuned vdW device. A standard graphite/hBN top gate is used to pick up and stack a monolayer WS_2 flake onto a pre-patterned platinum (grey) contact deposited on top of the bottom Bi_2SeO_5 layer. The entire device is assembled on a flexible polyimide strain substrate which is then attached to the strain cell. (**b)** Photoluminescence measurements of the monolayer WS_2 device at top gate voltages of -9.8 V (blue) and 7.3 V (black). An optical image of the device is inset, scale bar 5 μm. (**c)** Spatial map of PL intensity integrated over the entire spectral range with voltages of 0 and 7.3 V applied to the strain cell and top gate, respectively. (**d)** Spatial mapping of tensile strain taken at a piezo voltage of 40 V (**Methods**). 107
Figure 5.6: Gate-dependent photoluminescence of monolayer WS_2 strain device. PL measurements taken with 0 V applied to the strain cell as a function of voltage applied to the top gate. The sample is excited by σ^+ light, and the detected signal is co-circularly polarized with respect to the excitation. 108
Figure 5.7: Spatial map of photoluminescence energy at low and high strains. PL spatial maps at strain voltages of 0 V (**a**) and 40 V (**b**) with an applied gate voltage V_g = 7.3 V. The peak center energy is obtained by a Gaussian fit of X^- at each coordinate. 109
Figure 5.8: Strain tuning of exciton species in monolayer WS_2. (a, b) Strain-dependent co-circularly polarized photoluminescence measurements with the top gate voltage fixed at -9.8 V (**a**) and 7.3 V (**b**). (**c)** Extracted peak energy and degree of circular polarization, DOCP = $\sigma+ - \sigma- - \sigma+ + \sigma-$, of the various PL peaks as a function of piezo voltage obtained from the spectra in (**a)** and (**b)**. 110
Figure 5.9: Photoluminescence measurements taken during strain cycling. (a) PL spectra taken as the strain is swept from 0 V (solid black curve) to 40 V (red) and then back to 0 V (dashed black curve). The gate voltage is kept fixed at 7.3 V. **(b)** Extracted peak position plotted for versus applied strain voltage for sweep in (a). 111
Figure 6.1: Fabrication of high-quality strain- and gate-tunable WS_2/WSe_2 moiré superlattice devices. (A) Schematic of cryogenic strain apparatus, adapted to facilitate simultaneous electrostatic gating. **(B)** Cartoon of device architecture. **(C)** PFM of moiré pattern (left) measured before addition of top gate to show device quality on Bi_2SeO_5/PI and to extract moiré wavelength and corresponding twist angle from FFT of PFM image (right). **(D)** 100x optical image of finished top-gated device on PI with heterostructure region outlined by a red dashed line (left). 5x optical image with contact pads labeled (right). 117
Figure 6.2: Independent gate- and strain- tunability of IX PL. (A) Strain tuning of WS_2/WSe_2 IX PL feature, which demonstrates strain transfer without slipping. Shift in emission energy and oscillator strength transfer to high energy feature at $\epsilon \approx 0.75\%$ can both be observed. **(B)** Linecuts from (C) and (D) at zero gate voltage to show change in IX PL shape and

energy from $\epsilon = 0\%$ to $\epsilon = 0.89\%$. Top gate dependence of IX at $\epsilon = 0\%$ **(C)** and $\epsilon = 0.89\%$ **(D)**, shows both redshift and peak splitting under applied uniaxial strain.....118
Figure 6.3: Band structure engineering with strain probed by PLE. (A-C) Strain-dependent co-circularly polarized PLE showing evolution of IX feature under increasing tensile strain. **(D-F)** DOCP associated with PLE in panels A-C showing ~100% enhancement in DOCP of IX2 relative to IX1. 120
Figure 6.4: Power dependence of IX PL at $\epsilon = 1\%$. (A) Co-circularly polarized PL vs. excitation power for powers ranging from 30 nW to 30 μW. Excitation wavelength is fixed at 738 nm, and PL is normalized to excitation power and CCD integration time, so linear power dependence is represented by a constant color. The spectrum taken at 30 nW is subtracted from all data to remove a background artifact at 1.36 eV. **(B)** DOCP for the data shown in (A). **(C)** Integrated co-circularly polarized PL from 1.37 eV to 1.4 eV versus excitation power for IX 1. **(D)** Integrated co-circularly polarized PL from 1.4 eV to 1.47 eV versus excitation power for IX 2..... 121
Figure 6.5: Extracting strain from Raman measurements. (A) Strain-dependent Raman measurements on the WS_2/WSe_2 heterostructure. **(B)** Expanded view of (A) to show shift of the WSe_2 A_{1g} and E_{2g} modes. The in-plane E_{2g} modes lose their degeneracy under strain, with the E_{2g}^{-} mode experiences the greatest shift. **(C)** Peak positions of the $E_{2g}^{+/-}$ modes extracted via peak fitting with an algorithm developed by Tom O'Haver[345]. **(D)** Fitted E_{2g}^{-} mode vs. strain while sweeping up and down from (C), manually cleaned up to remove outliers and account for incorrectly fitted peaks. A calibrated strain axis is extracted based on a mode shift rate of -2.47 cm^{-1}/% tensile strain[107] (more conservative than a different report of 2 cm^{-1}/%[114]) and shown on the right. **(E)** Raw strain-dependent cross-circularly polarized PL from **Figure 6.2**A vs. applied piezo voltage. **(F)** Same data as in (E), identical to Figure 6.2A, with x-axis interpolated from strain calibration extracted from (D)..... 125
Figure 6.6: Additional measured devices. (A) Optical image, PFM, and FFT of moiré pattern for device D2, with identical stacking design as device D1 in the main text. **(B)** Optical image, TFM, and FFT of moiré pattern for device D3, with identical stacking design as device D1 and D2 in the main text. **(C)** Device D4, identical in design to D1-D3 except that 10 nm of PT are evaporated onto the PI prior to transferring the Bi_2SeO_5 to test strain transmission through a thin layer of metal that could eventually be used as a back-gate. **(D)** PFM images of moiré superlattice from D4 showing a clear moiré pattern. 127
Figure 6.7: Repeatable, reversible strain cycling on D1-D3. (A) Full data set from **Figure 6.2**A showing two full strain cycles. **(B)** Strain-dependent PL on device D2 showing same repeatable, continuous redshift and blueshift of the IX PL across five cycles on a second device. **(C)** Strain cycling on D1 at a gate voltage of 3V, so IX 2 does not emerge at high strain showing consistent behavior across 5 cycles. **(D)** Strain cycling on D3 across two cycles. 128
Figure 6.8: Strain-induced splitting of IX1 and IX2 at multiple spots on D1 and D2. Optical images showing two measured regions on D1 **(A, B)** and one on D2 **(C)**. Gate-dependent co-circularly polarized PL from two different spots on D1 (D, E) and one spot on D2 (F) at zero applied strain. **(G-I)** Gate-dependent PL at same spots at high strain showing emergence of secondary peak. 129

Figure 6.9: PLE at three different strains on D2. Co-circularly polarized PLE from D2 at 0V **(A)**, 50V **(B)**, and 100V **(C)** of applied strain. Though less distinct, the trends reproduce those observed from an identical measurement on D1 shown in Figure 6.3A-C. 130
Figure 6.10: Effects of FFT Filtering PL Spectra. (A) Raw data from **Figure 6.2**C. **(B)** FFT of linecut from (A) (blue) with bandpass filter indicating that the range of values from index 14 to index 188 will be removed from the FFT (orange). **(C)** Spectra in (A) after bandpass filtering spectra at each gate voltage. **(D)** Line cuts from (A) and (C) showing the effect of FFT filtering in greater detail. **(E)** Raw data from gate-dependent PL on D2. **(F)** FFT of linecut from (E) (blue) with bandpass filter indicating that the range of values from index 14 to index 188 will be removed from the FFT (orange). **(G)** Same spectra as in (E) after bandpass filtering at each gate voltage. **(H)** Line cuts from (A) and (C) showing the effect of FFT filtering in greater detail. (E) Raw data from gate-dependent PL on D2. 131
Figure B.1: Description of how peaks are selected from image for GPA. (a) Zoomed in HRTEM image of WS_2/WSe_2 moiré superlattice (same data as **Figure 4.8**a). **(b)** FFT of (a) with two peaks and masking radius identified. **(c)** Generated mask that will be applied (one circle at a time) to FFT image. **(d)** Zoomed-in image of (b) with points that will be used as reference reciprocal lattice vectors highlighted by red pixels. **(e, f)** Gaussian mask generated for each reciprocal moiré lattice vector (inset is FFT after applying mask). 141
Figure B.2: Demonstration of phase image formed from each masked peak during GPA. (a, d) $g \cdot r$ map for each moiré reciprocal lattice vector. This map represents a linear phase ramp due to the peaks being offset from the origin. **(b, e)** Phase image Pgr for each reciprocal lattice vector. (c, f) Processed phase image Pgr after linear phase ramps in (a, d) have been subtracted. 142
Figure B.3: Symmetrized strain and anti-symmetrized rotation matrix formed from GPA on example image shown in Figure B.1a. Symmetrized GPA-calculated strain matrix (a) and anti-symmetrized rotation matrix (b) for the data shown in **Figure B.1** and worked with in **Figure B.2**..... 143
Figure C.1: Raw PFM data (a-d), GPA-computed ϵxx (e-h), and GPA-computed ϵyy (i-l) for 0V, 10V, 15V, and 20V of applied strain. 144
Figure C.2: Raw PFM data (a-d), GPA-computed ϵxx (e-h), and GPA-computed ϵyy (i-l) for 25V, 30V, 35V, and 40V of applied strain. 145

Abbreviations

AFM	Atomic force microscopy, antiferromagnet
ARPES	Angle resolved photoemission spectroscopy
DOCP	Degree of circular polarization
EBL	Electron beam lithography
FFT	Fast Fourier transform
GPA	Geometric phase analysis
HRTEM	High resolution transmission electron microscope
KPFM	Kelvin probe force microscopy
PI	Polyimide
PFM	Piezoresponse force microscopy
PU	Picosecond ultrasonics
PL	Photoluminescence
QAH	Quantum Anomalous Hall
RT	Room temperature
SHG	Second harmonic generation
STM	Scanning tunneling Microscope
TMD(C)	Transition metal dichalcogenide
vdW	Van der Waals

Acknowledgements

First and foremost, I want to thank my advisor, Xiaodong Xu. Xiaodong's lab has been a place of tremendous growth and transformation for me. Xiaodong is a brilliant scientist with an unparalleled work ethic who is more present in lab, knowledgeable about my projects, and prompt about feedback than anyone as busy as he is has a right to be. Xiaodong has pushed me to grow in ways that are uncomfortable but ultimately rewarding, and I would not be the scientist I am today without the confidence and skills I've developed during my PhD under his mentorship. Xiaodong provides kind encouragement but also challenges my ideas. He has mentored me through project after project, trusted me to build and maintain critical lab equipment, sent me to conferences to present my work, involved me in the grant writing process, and given me undergraduate and REU students to mentor. I have learned so much about so many different aspects of being an academic, a mentor, and a scientist under Xiaodong, and I feel very fortunate to call him my advisor.

I also want to express my gratitude to my supervisory committee: Xiaodong Xu, Di Xiao, Dave Cobden, Armita Nourmohammad, Arthur Barnard, Jiun-Haw Chu, and Daniel Gamelin. Your mentorship, teaching, and feedback on my work have improved my science and supported my growth as a scientist.

One of the things that makes Xiaodong remarkable is not only his individual skill, but his ability to draw such a variety of brilliant, kindhearted, and hardworking people into his circle. During my PhD, I had the unbelievable good fortune to work with two postdocs in particular who took me under their wings: Geoff Diederich and Dmitry Ovchinnikov. Behind his deadpan dark humor, Dmitry hides an even-keeled, resilient optimism about science and a strong sense of integrity about how to be a great scientist, advisor, and human being. I hope his new graduate students appreciate how lucky they are to work with him. Geoff started their postdoc shortly after

I started my PhD, and they are the person I've worked with most closely throughout my schooling. They bring a refreshing, pure joy to optical measurements, experiment building, and beautiful data, and it is largely because of them that I developed the skill and confidence to tear down and rebuild an experiment over and over again until it worked the way I wanted it to. Geoff taught me to appreciate a fast Fourier Transform more than I thought possible and provided me with more emotional support than can be summarized here. Academic physics is a better place because of Geoff and Dmitry's presence and contributions, and I am a better scientist because of their kind mentorship. I thank them both.

I experience science to be a collective effort done by many people who contribute many different skills, perspectives, and values to the shared process. In particular, working in any single 2D materials lab at UW is really like being a member of a consortium of groups who share resources, knowledge, and equipment so freely that the boundaries of where one lab ends and another begins are hardly perceptible. For cultivating this environment, thank you to Dave Cobden, Jiun-Haw Chu, Arthur Barnard, Matthew Yankowitz, and Xiaodong Xu, and to Di Xiao and Ting Cao for bringing a similarly open group approach to our theoretical counterparts. I feel lucky to have been able to collaborate with so many different groups during my time at UW, both on campus and off. Thank you to Shuai Zhang and Dmitri Basov at Columbia for thoughtful discussions and impressive near-field measurements of graphene on sliding-ferroelectric moiré materials. It was a pleasure to collaborate with you. Thank you to Dacen Waters, Ellis Thompson, and Anna Okounkova from the Yankowitz lab for involving me in your efforts to understand anomalous behavior in hBN-aligned-to-graphene devices. Thank you to Shuai Zhang and Ying Xia at UW for bringing your expertise in atomic force microscopy to bear on understanding how strain affects a moiré superlattice. Thank you to Florie Mesple and Juan Carlos Idrobo for helping me understand

geometric phase analysis and how it can be used to study the geometry of moiré materials. Thank you to Laurel Anderson and Arthur Barnard for involving me in your efforts to transfer 2D materials onto tungsten tips for Coulomb screening experiments. Thank you to Adina Ripin and Mo Li for joining forces with me and John Cenker to explore whether surface acoustic waves could modulate magnon behavior in CrSBr. Thank you to Yuzhou Zhou for spearheading our own lab's attempts to recreate the "Quantum Twisting Microscope" and, more importantly, for bringing an "I can make this work better" and "I'd love to help you do that" mindset to the lab.

Within our lab, I want to thank Nathan Wilson and Bevin Huang for modeling how senior graduate students can be supportive, productive, and fun. I want to thank Tiancheng Song for sharing my passion for StarCraft II, and Minhao He for being an undying well of knowledge about everything from fabrication to theoretical physics. Kyle Hwangbo was the first graduate student I worked with, and I will always have fond memories of the month we spent losing our minds and exploring every possible way our lab could measure the lifetime of the $NiPS_3$ exciton to appease the infamous Reviewer 2. John Cenker is more passionate about straining 2D materials than anyone I've ever met, and I've greatly appreciated his mentorship, enthusiasm, and collaboration on my work to strain moiré heterostructures. It's been wonderful to learn and grow with my four cohort-members, Jiayi Zhu, Eric Anderson, Jiaqi Cai, and Yinong Zhang. I greatly appreciate having had the opportunity to do my PhD alongside such brilliant, curious, and hardworking peers. Congratulations to each of you for making it to the end of the long, winding road of a PhD. I know you'll all go far in your respective endeavors. I've also appreciated the chance to share what I know with and to learn from the subsequent generations of students: Heonjoon Park and Will Holtzmann, Jack Barlow and Courtney Baier, Mai Nguyen and Ren Pumulo, and now Dhan Bautista, Essance Ray, and Julian Stewart. You all work so hard to run the complex organism of a

research lab and to drive forward your individual projects, and I'm so impressed by each one of you. Thank you to the many postdoctoral scholars who have been great colleagues, taken the lead on developing new experimental capabilities, and provided so many different models of how to be a great scientist: Xi Wang, Yingqi Wang, Jiang Yao, Chaowei Hu, and Weijie Li. Last but certainly not least, I want to thank the undergraduate students I've worked with over the years: Sara Barrows, George Rickey, and Eric Zhao. Working with you has helped me understand my own science better, and I'm so grateful for the time you dedicated toward working on projects with me.

My whole life, I have had teachers who fostered my curiosity, tolerated my frustration, and helped me discover the joy and beauty of physics. Thank you to my first high school physics teachers, Mr. Kedge and Ms. Gilbert. Thank you to my wonderful college professors: David Latimer, Andy Rex, Rachel Pepper, Greg Elliott, and Amy Spivey. Thank you to my professors from graduate school, who showed me that a research-focused graduate program could still offer excellent courses: Steve Sharpe, Lukasz Fidkowski, Leslie Rosenberg, Mo Li, Arthur Barnard, Xiaodong Xu, Di Xiao, Armita Nourmohammad, Miguel Morales, and David Kaplan.

While I'm so grateful to have such a rich professional and academic community, I would not have thrived during (or perhaps even finished) my PhD without the support of my loving friends and family. My mom, Heather Burnett, dad, Jorge Fonseca, and younger sister Shannon Fonseca have each been an endless source of support. As far as I know, I am the first person in my family to receive a PhD. This is in large part a result of how much my parents—and their parents before them—understood the value of education and did everything they could to make sure I had opportunities that they did not.

At every turn in my journey, I find myself blessed (for lack of a better word) to have the loving, thoughtful, brilliant friends that I do. My community means everything to me, and I feel

so lucky to have remained in touch with so many wonderful people. From my childhood, thank you to Jeremy Hartse (a fellow UW PhD student and far more theoretically inclined physicist) and to Niall Ridgley. From high school, thank you to Christina Fox, Alex Prossnitz, Nicole Fox, Sam Berling, and many more. From college, I especially appreciate my cohort of physics peers who supported me and pushed me for 4 great years at the University of Puget Sound: Sam Berling, Alex Kaufman, Matt Fergoda, Jessy Hosken, Kri Michaud, Nic Rothbacher, and Kyle Miller. Finally, it's been wonderful to make new friends while at UW within and beyond the university. Thank you to Sam Tetef, Sarah George, Claire Huntington, Tharindu Fernando, Robert Pecoraro, Heather Harrington, and Maddie & Daniel Zdeblick.

Lastly, thank you to Elena and her family, who accompanied me through some of the most challenging years. I am forever grateful; you each bring so much light to the world.

Publications

1. John Cenker†, **Jordan Fonseca**†, Mai Nguyen†, Chaowei Hu, Jiun-Haw Chu, Xiaodong Xu, "Engineering robust strain transmission in van der Waals crystals and heterostructures" *In preparation* (2024)
2. Shuai Zhang†, **Jordan Fonseca**†, Daniel Bennett, Zhiyuan Sun, S.L. Moore, Suheng Xu, S.E. Rossi, Leo He, Dmitry Ovchinnikov, David Cobden, M.M. Fogler, Efthimios Kaxiras, Xiaodong Xu, D.N. Basov, "Plasmonic polarization sensing in graphene superlattices actuated by twisted-hBN antiferroelectricity" *In review, PRX* (2024)
3. Geoffrey M. Diederich, John Cenker, **Jordan Fonseca**, Sinabu Pumelo, Youn Jue Bae, Daniel G. Chica, Xavier Roy, Xiaoyang Zhu, Di Xiao, Yafei Ren, Xiaodong Xu, "Exciton Dressing by Extreme Nonlinear Magnons in a Layered Magnetic Semiconductor" *In review, Nature* (2024)
4. **Jordan Fonseca**†, Geoffrey M. Diederich†, Dmitry Ovchinnikov, Jiaqiang Yan, Di Xiao, Xiaodong Xu, "Picosecond Ultrasonics in Magnetic Topological Insulator $MnBi_2Te_4$" *In review, Nano Letters* (2024)
5. Shuai Zhang, Yang Liu, Zhiyuan Sun, Xinzhong Chen, Baichang Li, S. L. Moore, Song Liu, Zhiying Wang, S. E. Rossi, Ran Jing, **Jordan Fonseca**, Birui Yang, Yinming Shao, Chun-Ying Huang, Taketo Handa, Lin Xiong, Matthew Fu, Tsai-Chun Pan, Dorri Halbertal, Xinyi Xu, Wenjun Zheng, P. J. Schuck, A. N. Pasupathy, C. R. Dean, Xiaoyang Zhu, David H Cobden, Xiaodong Xu, Mengkun Liu, M. M. Fogler, James C. Hone, D. N. Basov, "Visualizing moiré ferroelectricity via plasmons and nano-photocurrent in graphene/twisted-WSe_2 structures," *Nat. Comm.* (2023)
6. Geoffrey M. Diederich, John Cenker, Yafei Ren, **Jordan Fonseca**, Daniel G. Chica, Youn Jue Bae, Xiaoyang Zhu, Xavier Roy, Ting Cao, Di Xiao, Xiaodong Xu, "Tunable interaction between excitons and hybridized magnons in a layered semiconductor" *Nat. Nano.* (2022)
7. **Jordan Fonseca**†, Geoffrey M Diederich†, Dmitry Ovchinnikov, Jiaqi Cai, Chong Wang, Jiaqiang Yan, Di Xiao, Xiaodong Xu "Anomalous Second Harmonic Generation from Atomically Thin $MnBi_2Te_4$" *Nano Letters* (2022)
8. John Cenker, Shivesh Sivakumar, Kaichen Xie, Aaron Miller, Pearl Thijssen, Zhaoyu Liu, Avalon Dismukes, **Jordan Fonseca**, Eric Anderson, Xiaoyang Zhu, Xavier Roy, Di Xiao, Jiun-Haw Chu, Ting Cao, Xiaodong Xu, "Reversible strain-induced magnetic phase transition in a van der Waals magnet," *Nat. Nano.* (2022).
9. Nathan P Wilson, Kihong Lee, John Cenker, Kaichen Xie, Avalon H Dismukes, Evan J Telford, **Jordan Fonseca**, Shivesh Sivakumar, Cory Dean, Ting Cao, Xavier Roy, Xiaodong Xu, Xiaoyang Zhu, "Interlayer Electronic Coupling on Demand in a 2D Magnetic Semiconductor," *Nat. Mater.* (2021).
10. Kyle Hwangbo, Qi Zhang, Qianni Jiang, Yong Wang, **Jordan Fonseca**, Chong Wang, Geoffrey M Diederich, Daniel R Gamelin, Di Xiao, Jiun-Haw Chu, Wang Yao, Xiaodong Xu, "Highly Anisotropic Excitons and Multiple Phonon Bound States in a Van der Waals Antiferromagnetic Insulator," *Nat. Nano.* (2021).

Dedication

To my loving friends, my endlessly supportive parents Heather and Jorge, my amazing sister Shannon, and my perfect cat Lydia 🐾

Chapter 1 | Introduction

Most introductory physics courses begin by introducing the kinematic equations of motion for Newtonian physics in one dimension. This approach evades the details of working with vector quantities and makes learning the physical concepts and equations simpler, at least in theory. Once students are comfortable with the fundamentals, they begin working with 2 and 3 spatial dimensions, incorporating the uniqueness of a gravitational pull in the "up and down" direction and the ability for objects to exist and move freely in the three-dimensional world we live in. From the perspective of the equations of motion, each dimension is independent, but not particularly unique. Objects can have positions and velocities, experience forces that cause accelerations, and so forth in any dimension. There is a general understanding that the physics of each dimension is not unique and that while it's easier to learn a new equation in one dimension, moving to higher dimensions is merely a matter of keeping your *i*-hats and *j*-hats straight; a small price of tedium to pay to describe how any object moves in the real world around us, not on the 1D cart track of a physics laboratory.

But already in the 3D macroscopic world of blocks on planes and cars turning on racetracks, there is an awareness that the 3 dimensions of our world are *not* all the same. In Cartesian coordinates, we usually call the direction parallel to gravity the *z-axis*; in polar coordinates, it is the *r-axis*, and the physics that governs how objects move along this axis is understood to be fundamentally different than the other two axes, typically because of gravity. The existence of a gravitational field makes one direction unique, not because the laws of physics are themselves unique along that axis but because in the world we live *on*, gravity is what gathered us here in the first place. We agnostically label axes x-, y-, and z-, but I dare you to walk, for example,

10 paces along the x-axis, 10 paces along the y-axis, and 10 paces along the z-axis. One of these is not like the others.

The observation that gravity makes “up and down” different from “forward and backward” or “left and right” doesn’t sound particularly profound, but there is a kernel of much of the richness of physics in this simple realization. The globe is spherical (or nearly so) *because* of gravity—which is itself a spherically symmetric force (or field). The symmetry of gravity that pulls masses *directly toward* each other, and the fact that all fundamental forces have this property, is why we think about physics the way we do.

In Phil Anderson’s famous 1972 *Science* article “More is Different”, he writes that "it is only slightly overstating the case to say that physics is the study of symmetry"[1]. The relationship between the symmetries that systems, objects, or equations have and how their effects manifest in the world is profound. As noted above, the world is round *because of the symmetry of gravity*, though it is also not *completely* symmetric because of (1) inhomogeneity, and (2) the fact that gravity is not the *only* force acting on the mass that makes up the earth.

In “hard” condensed matter physics, the world of interest is the world of crystal structures, and the first symmetries that govern what properties emerge in these systems are the symmetries that govern how atoms can pack together to form a crystal lattice. In a universe with 118 different known elements and a near-endless number of possible bonding configurations that join atoms together, it is perhaps surprising that in total, there are only 32 different point group symmetries that crystals can have. This constraint is enacted by the requirement that for a crystal to exist as a single entity, rather than a cluster of molecules, the structure must be periodic in as many dimensions as it exists in, be that 1, 2, or 3. Because symmetry is so important to physical laws and to the behavior of physical systems, symmetry-breaking effects have a uniquely powerful

effect on these material systems. While there are many ways to break various symmetries in condensed matter systems, one of the most obvious and direct ways to alter a crystal symmetry is by stretching, or *straining* the crystal. If a uniaxial strain is applied that only stretches the crystal in one direction, this in-plane symmetry is reduced to a 2-fold symmetry. This transformation can be imaged by picturing a square, which has four-fold symmetry (4 90^o rotations), being stretched into a rectangle (which only looks identical when rotated 180^o). As will be discussed later, atomically thin crystals turn out to be extremely well suited for strain studies.

The terms "2D material" and "van der Waals material" are often used somewhat interchangeably, but they are not strictly the same. Generically, a useful definition of a 2D material rooted in physics is that a 2D material is any material in which quantum confinement in the out-of-plane dimension becomes significant. (A 1D material, like a nanowire or carbon nanotube, experiences this quantum confinement in two dimensions but not along the axis of the wire.) There is a rich history of studying 2D electron gases (e.g. on the surface of helium) and confined electron systems (e.g. GaAs-based quantum wells) that predate the study of 2D vdW materials.

Van der Waals crystals have layered crystal structures that can be thought of like a ream of printer paper. Atoms within the plane are covalently bonded together, while only the relatively weak van der Waals force keeps adjacent layers stuck together. This property makes it easy to cleave vdW materials into layers because the vdW bond is far more likely to break when stressed than the in-plane covalent bonds. Van der Waals materials make good 2D materials because this cleaving process can be repeated until there is only a single layer of crystal—a monolayer—remaining.

This cleaving process can, remarkably, be accomplished with off-the-shelf Scotch tape (which, 20 years after the first exfoliations, remains the first choice of most 2D materials research

groups). The exfoliation process to obtain monolayer flakes from bulk crystals is shown in **Figure 1.1**. First, a bulk vdW crystal is prepared (Graphite from 2D Semiconductors in **Figure 1.1**a). Scotch tape is then used to peel the bulk crystal into a field of thinner bulk flakes (**Figure 1.1**b), which are subsequently pressed onto a substrate (typically a silicon wafer coated with a layer of silicon dioxide to enhance flake contrast via thin film interference, **Figure 1.1**c). When the tape is peeled away (**Figure 1.1**d), the crystal cleaves at the vdW interface (**Figure 1.1**e) and a random assortment of flakes of various thicknesses, shapes, and sizes is left behind. The chip is then searched using an optical microscope (**Figure 1.1**f) until flakes that suit a given research purpose are found. Typically, this process is performed manually, although there are examples of robotic searching based on computer vision that can be used as well[2,3]. As the story goes, the experimental discovery of monolayer graphene—the first monolayer material ever isolated from bulk crystal—by Novosolov and Geim in 2004 was made using exactly this technique[4].

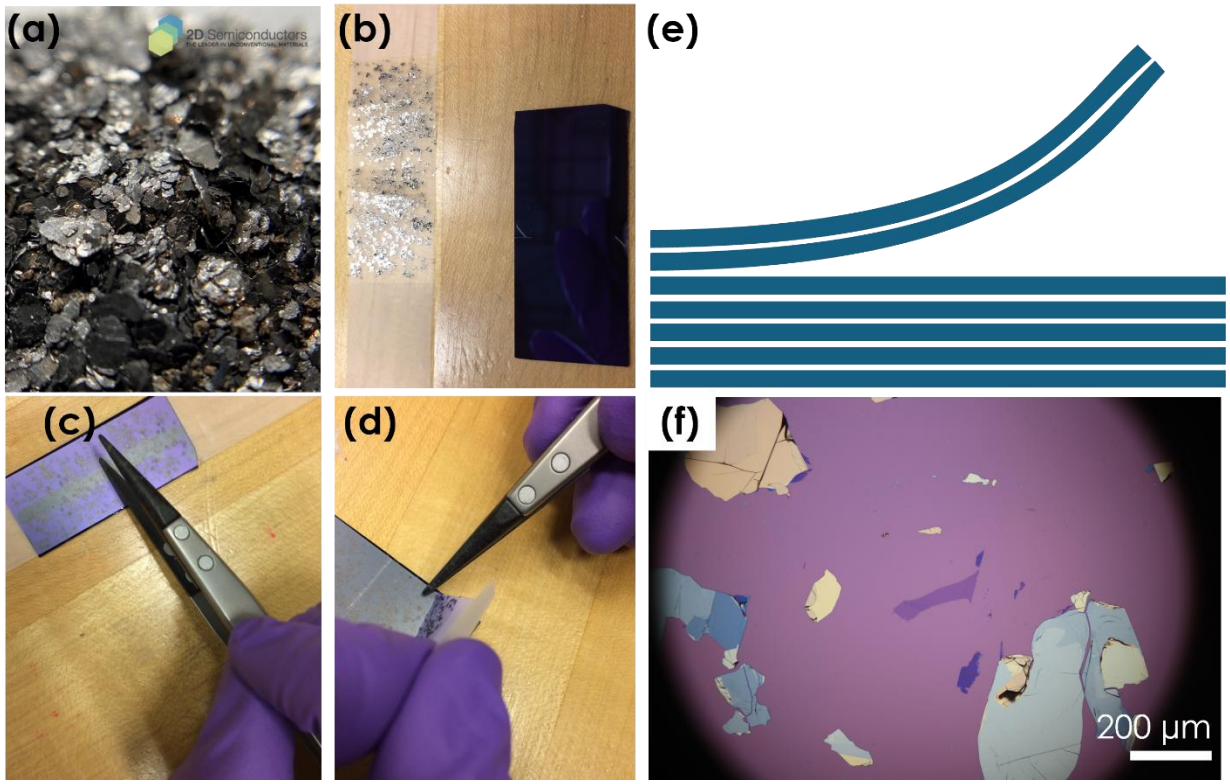

Figure 1.1: Scotch tape exfoliation process. Bulk crystal **(a)** is peeled into thin flakes on scotch tape **(b)**, which is then pressed onto a Si/SiO_2 substrate **(c)** and peeled away **(d)**, which cleaves vdW crystals at the vdW interface **(e)**, leaving a chip covered with a variety of atomically thin flakes that can be searched with an optical microscope **(f)**.

While there are many different measurements that can be performed on bare flakes, most of the appeal of 2D materials lies in the physics that can be uncovered when multiple flakes are stacked together to form heterostructures. Originally, flakes were combined using a wet transfer process[5–7] which leverage capillary forces to separate a 2D material from a growth substrate; however, today dry transfer techniques based on selective use of polymer films have become the first choice for most 2D labs because of their precision, repeatability, and versatility[7,8]. There are many slight variations in the dry transfer process, but the essential concepts are universal and depicted in Figure 1.2. Central to the transfer process is a simple technology called a “stamp” that

provides an accurate, gentle way to pick up and deposit nearly any van der Waals material. A stamp consists of a thin adhesive layer (typically polycarbonate or polypropylene carbonate) stretched over a rubbery layer that can be curved or flat (typically polydimethylsiloxane) affixed to a transparent glass slide (**Figure 1.2a**). By loading the stamp into a transfer stage that allows precise control over the chip temperature, chip position, stamp position, and microscope position (**Figure 1.2b**). The transfer process is repeatable, and stacks of flakes can be assembled "top-down" by picking up one flake after another until a device is fully assembled (**Figure 1.2c**).

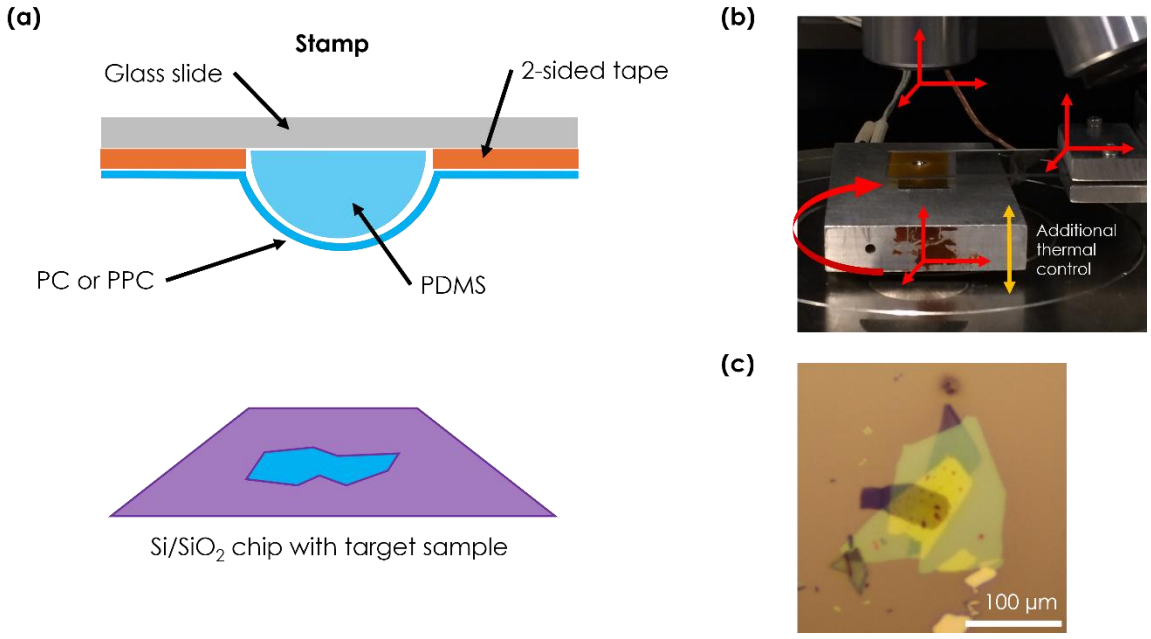

Figure 1.2: Dry transfer technique for assembling vdW heterostructures. (a) A "stamp" consisting of a sticky polymer (PC or PPC) extended over a squishy polymer (PDMS) creates a gentle, controllable adhesive surface for picking up and transferring a wide variety of 2D materials. **(b)** A "transfer stage" that allows independent positioning of a substrate holder, stamp holder, and optical microscope facilitates the transfer process. **(c)** An example of a stacked heterostructure before the PC film has been removed from the final substrate.

Precise, on-chip electrical contact can be made to different flakes in a 2D device using electron beam lithography (EBL). After transferring a heterostructure, the entire chip is coated with a polymer resist layer. Polymethyl-methacralate (PMMA) provides the necessary resolution for most of our purposes, although more expensive resists that provide sub-200 nm feature resolution can also be used when required. A scanning electron microscope (SEM) is then used to selectively expose portions of the resist layer, which breaks up polymer chains in the resist (**Figure 1.3**a). When the chip is exposed to a solvent (a combination of isopropanol and water), the channels with weakened resist dissolve quickly, leaving selected portions of the chip and heterostructure exposed (**Figure 1.3**b). The chip can then be loaded into a metal evaporation chamber (e-beam or thermal) in which thin films of different metals can be evaporated with precise thickness control (**Figure 1.3**c). Finally, solvents are used to completely remove the mask, leaving the heterostructure with on-chip electrical connections (**Figure 1.3**d, e).

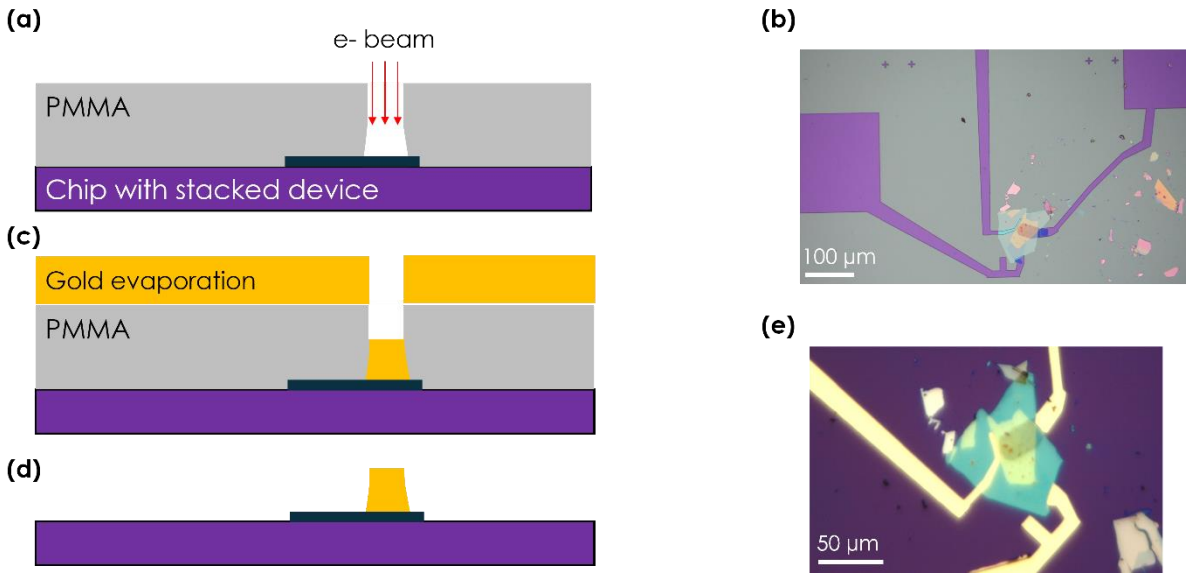

Figure 1.3: Making electrical contact to 2D materials with electron beam lithography and metal evaporation. (a) Schematic side-view showing how electron beam exposure and solvent use define precise channels in a PMMA mask spin-coated over the whole device. When gold is

evaporated over the whole surface and the PMMA is washed away with solvents, only the gold contacts to the 2D device remain. **(b)** Microscope image of channels left behind in PMMA after EBL. **(c)** Microscope image of finished device with metal contacts to the target flakes.

Since the discovery of graphene and the first exploration of its remarkable electronic properties, which include semi-metallic Dirac-like linear dispersion around its K-points and a Fermi energy pinned at charge neutrality[4,9–11], a vast swathe of 2D materials with different unique properties have been discovered. In addition to the existence of a variety of metals, semiconductors, and insulators, the field has seen the discovery of monolayer magnetism[12,13], superconductivity in atomically thin flakes[14], and the eruption of topological insulators and topologically nontrivial materials and heterostructures. Beyond individual material properties, 2D vdW materials offer the opportunity to probe layer-dependent changes in electronic and topological properties, to engineer proximity effects, and to fabricate complex heterostructures that enable unparalleled control over materials by tuning carrier type, carrier density, and symmetry-breaking electric fields.

One of the most important experimental tools for a materials scientist or engineer is the ability to tune carrier density—to *dope* a crystal. Carrier density, be that the density of electrons or holes in a crystal, has a dramatic effect on material properties. The periodic table itself is organized primarily by counting how many total electrons each atom has, and this is because the number of valence electrons nearly single-handedly determines an element's chemistry. In crystalline materials, the number of excess electrons can be altered by selectively substituting a certain percentage of one element with a different element that occurs neutrally with more or fewer electrons. For bulk crystals, this *stoichiometric doping* is the only way to meaningfully and change carrier density across the whole sample, and it has been used to great effect to explore the phase

space of high-Tc cuprate superconductors, for example. The downside of this approach is that achieving a given doping level requires growing a new crystal. This is a time-consuming process that is susceptible to fluctuations in repeatability, and it makes fine-tuning carrier density over a large range an intractable problem.

One of the most appealing aspects for studying the electronic properties of 2D materials is the ability to tune carrier density with an electrostatic gate rather than stochiometric doping. When a 2D material or heterostructure is sandwiched between a capacitor-like structure consisting of dielectric insulating layers between metallic flakes (**Figure 1.4a**), applying voltages to the top or bottom gates alters the electrostatic potential seen by electrons in the 2D material or heterostructure. In bulk crystals, electronic screening at the material's surface prevents the application of homogenous potentials across the entire sample; however, in 2D the screening is reduced sufficiently for this gating to have a significant effect. For a dual-gated device architecture, the application of arbitrary voltages to each plate results in a combination of electrostatic doping and out-of-plane electric field. With knowledge of the dielectric environment and layer thickness, it is possible to perform a change of basis from axes of top-gate and bottom-gate voltages to axes of pure carrier density and pure electric field (Equations 1.1 and 1.2, **Figure 1.4b**)

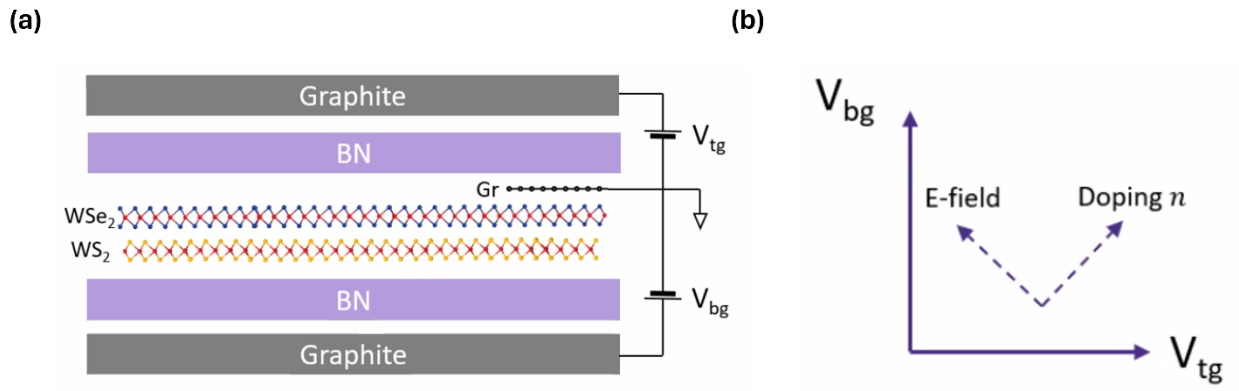

Figure 1.4: Electrostatic gating of 2D materials with capacitor-like device structure. (a) Schematic of a 2D heterostructure sandwiched between stacks of insulating, dielectric hBN and conductive graphite with electrical connections to apply voltage to the top and bottom gate while keeping the sample grounded. (b) Schematic showing the change of basis from top- and bottom-gate voltages to electric field and carrier density, using Equations 1.1 and 1.2.

$$n = \frac{-1}{e}\left[\frac{\varepsilon_{BN}\varepsilon_0}{d_t}(V_t - V_{t0}) + \frac{\varepsilon_{BN}\varepsilon_0}{d_b}(V_b - V_{b0})\right][\mathrm{cm}^{-2}] \quad 1.1$$

$$E = \left(\frac{V_t}{d_t} - \frac{V_b}{d_b}\right) \quad 1.2$$

While graphene was both the first vdW material to be exfoliated as well as a profoundly rich physical system for study over the past 20 years, the transition metal dichalcogenide (TMD) semiconductor family is a close rival. Graphene's semi-metallic nature makes its electronic properties most readily probed by electrical transport measurements, while the monolayer TMDs are direct-bandgap semiconductors with gaps in the visible to near-IR spectrum, making them easy to probe with light and technologically promising for a variety of lighting applications. TMDs have the stochiometric formula MX_2 where M is a transition metal—typically W or Mo, although Ti, Cr, and V-based compounds also go by this name—and X is a chalcogen S, Se, or Te. From a theoretical perspective, the TMDs share several unifying properties. They all have direct bandgaps

at the K-point in the monolayer with all but $MoTe_2$ becoming indirect in even bilayer. They all share the D_{3h} point group, which lacks inversion symmetry, giving rise to strong nonlinear optical response[15–25]. Monolayer TMDs have strong spin-orbit coupling and exhibit spin-valley locking at the K-points, which establishes optical selection rules that govern the lowest level optical excitations that dominate their tunable optical properties [26–37]. Beyond small quantitative differences, the main qualitative theoretical differences between different species of TMDs is a reversed spin-splitting in the conduction band K-points for Mo- and W-based TMDs[36], giving them different selection rules and optical ground states.

For the past 8 years, the aspect of 2D materials that has garnered the most attention is the moiré superlattice, which results when two similar periodic structures that differ by a small spatial mismatch or relative twist angle are placed in proximity. This effect can be seen clearly by eye at macroscopic length scales, shown in **Figure 1.5a** by the interference seen from a screen door. This phenomenon, which is an interference effect analogous to beating between sound waves and was well-known in the photography community—particularly in the era of pixelated digital photography, is important in materials science because it introduces a new periodic length-scale to the electronic environment. Moiré superlattices can have periodicities ten to hundreds of times those of the constituent crystalline materials. An example of the moiré superlattice formed by a 4^o twisted WS_2/WSe_2 heterostructure is shown in **Figure 1.5b**. Commensurate with this larger periodicity is a potential landscape that can localize electrons, holes, and other quasiparticles. Furthermore, since 2D materials are amenable to electrostatic doping, moiré superlattice sites can be precisely filled with enough electrons or holes for one to inhabit each site, or each other site, or each third site, etc. A vast amount of theoretical and experimental work has been done to study how moiré superlattices offer platforms in which intersite hopping is sufficiently quenched to

produce flat, low-energy moiré bands that exhibit correlated many-body physics[38–56]. Since correlated electronic phenomena are not the focus of this dissertation, the curious reader should consult the many excellent reviews that have been published about moiré systems in graphene and TMD homo/heterostructures[57–64].

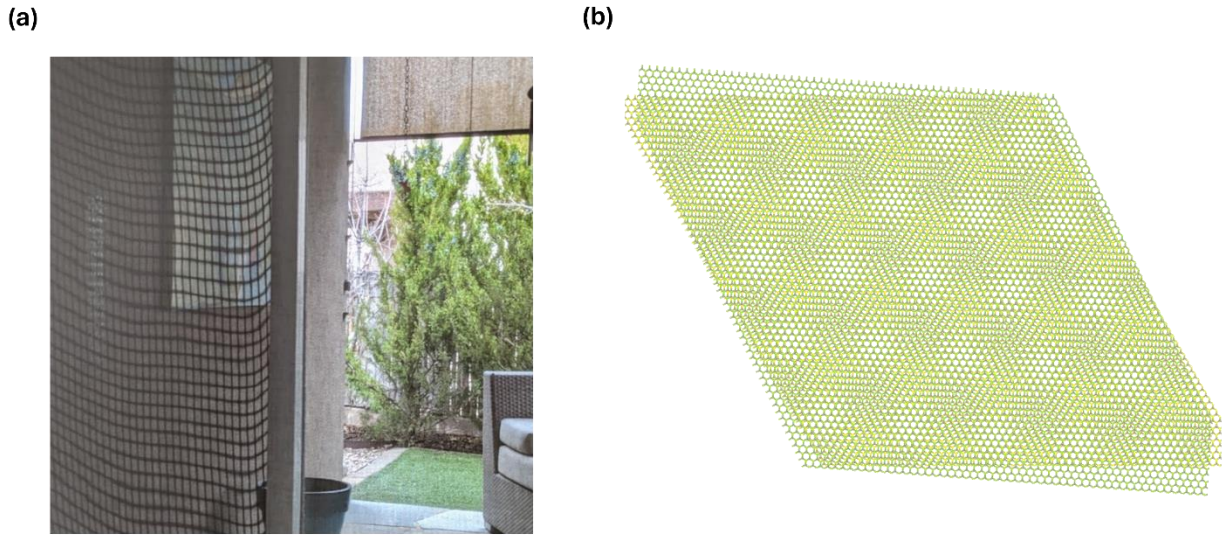

Figure 1.5: Moiré patterns around us and in 2D crystals. (a) Moiré pattern formed by a screen door showing the pattern resulting from interfering mesh screens (left) that is absent when only a single screen is present (right). **(b)** Moiré superlattice formed by a WS_2/WSe_2 heterostructure, which results from a combination of the ~4% lattice constant mismatch between the two crystals and the 4^o relative twist angle.

Yet another aspect of 2D materials that makes them stand apart from bulk crystals is their unparalleled flexibility. The combination of low dimensionality and low defect density makes it possible for 2D materials to bend, fold, and stretch far more than most crystal structures before they break, or "yield." **Figure 1.6**a schematically demonstrates a variety of ways that the unique flexibility of 2D materials can be leveraged to do things that would not be possible with bulk crystals. **Figure 1.6**b and **Figure 1.6**c show scanning electron microscopy (SEM) images of 2D

crystals that have experimentally been significantly deformed in some of the ways depicted in **Figure 1.6**a. This property is scientifically interesting and potentially technologically useful in two somewhat orthogonal ways. First, a crystal structure that can be easily molded around an irregular, soft, or moving surface is a promising platform for flexible electronics, and the 2D nature of these materials also makes them lightweight and low-profile which furthermore enhances their potential utility. Already, studies about the potential for wearable electronics from 2D materials abound[65–67]. Alternatively, the ability to stretch a crystal lattice without breaking it opens the path toward strain tuning electronic properties.

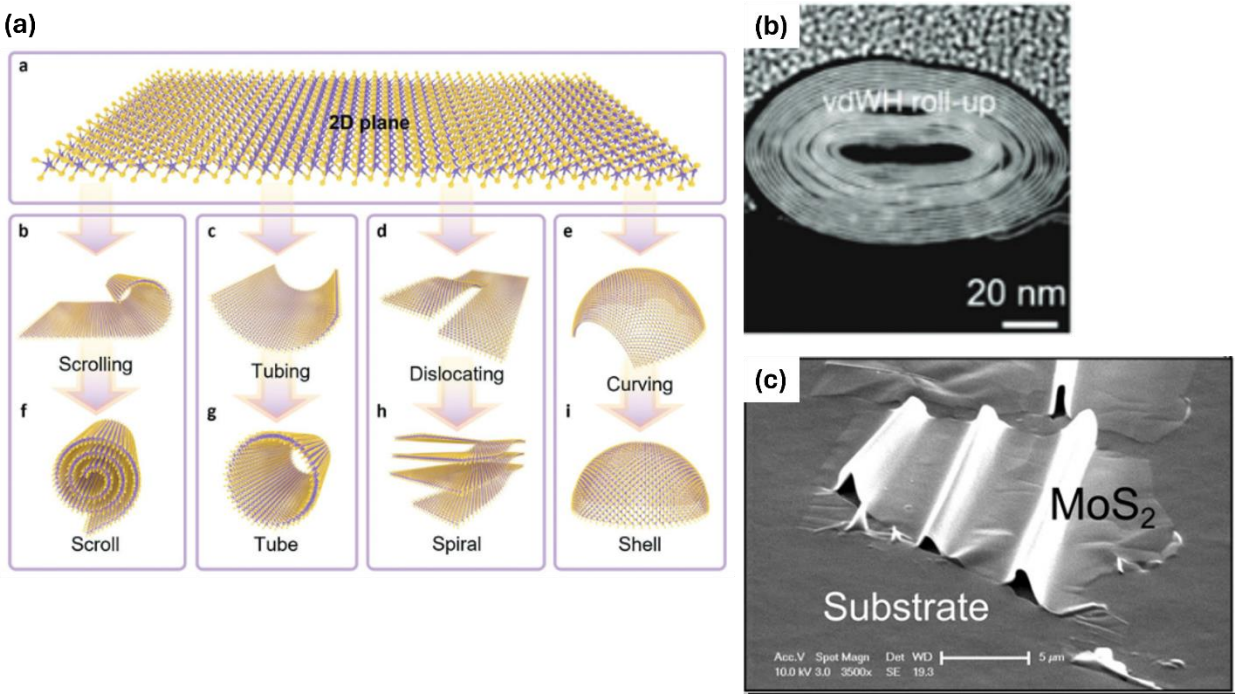

Figure 1.6: Flexibility of 2D crystalline materials. (a) Schematic of the ways that a monolayer 2D material can be deformed in myriad ways. **(b)** SEM images of 2D material rolled back on itself many times. **(c)** SEM image of 2D MoS2 wrinkling on a soft substrate. Panel (a) reproduced from ref.[68], panel (b) reproduced from ref.[69], and panel (c) reproduced from ref.[70] . All panels reproduced with permission.

Strain impacts material properties for two reasons. To begin with, the electronic properties of crystals are inherited from the wavefunction overlap of adjacent atoms. While a single atom has an electronic structure described by orbitals and interacting atoms exhibit "hybridized" orbitals, a crystal can be considered as a heavily hybridized electron orbital that is smeared out across space and more commonly described by a *band structure*. If atoms are pushed closer together or pulled apart, the overlap of their electron wavefunctions with those of adjacent atoms changes, altering the electronic properties of the whole crystal. Furthermore, strain can lift crystal symmetries and break degeneracies. While the van der Waals gap already makes the out-of-plane axis unique, 2D materials often exhibit 3, 4, or even 6-fold symmetry within the plane. These symmetries underpin the physical properties that the material has. If a uniaxial strain is applied that only stretches the crystal in one direction, this in-plane symmetry is reduced to a 2-fold symmetry. This transformation can be imaged by picturing a square, which has four-fold symmetry (4 90^o rotations), being stretched into a rectangle (which only looks identical when rotated 180^o).

The differences between straining a bulk 3D crystal and a 2D material are profound, but to understand these differences, it is important to understand the fundamentals of strain, which is really the purview of mechanical engineering or materials science. To stretch a material, a "stress" must be applied. This stress, which has units of Pascals, describes a force (or really, a pressure) applied to a material in a given direction. "Strain," on the other hand, is a unitless quantity that describes the deformation of the material that occurs because of this applied stress. In one dimension, a rod of length L lying on the x-axis that experiences a stress σ_x in the x-direction and elongates a length ΔL has been strained an amount $\Delta L/L$. As the stress on the rod increases, the strain also increases. At a certain point, depending on the material composition of the rod, the applied stress exceeds the threshold of the material to stretch, and the rod will "yield," which often

takes the form of permanent plastic deformation or fracturing. Materials can be characterized by stress-strain curves (Figure 1.7d), and all materials have a "linear" regime over which the applied stress results in a proportional strain that is reversible without causing permanent damage to the material. The slope of the stress/strain curve in this linear regime is referred to as the materials Young's modulus or elastic modulus and quantifies the "stretchiness" of a material. Soft polymers typically have a Young's modulus on the order of GPa or lower[71] (e.g. Polyimide, which has a Young's modulus of ~2.5 GPa[72]), while metals have moduli in the tens to hundreds of GPa[73].

In two dimensions, the strain tensor is a 2×2 matrix resulting from the two independent directions along which stress can be applied and strain can be experienced. This tensor can be considered with its cartesian component matrix elements or broken down into a biaxial strain ϵ_c and a pure shear strain ϵ_s (Eq. 1.3).

$$\epsilon = \begin{pmatrix} \epsilon_{xx} & \epsilon_{xy} \\ \epsilon_{xy} & \epsilon_{yy} \end{pmatrix} = \epsilon_c \mathbb{I} + \epsilon_s S_{\phi_s} \tag{1.3}$$

Biaxial strain, which describes equal stretching or compression in both directions and only changes the size of the unit cell, takes the form of Eq. 1.4 and is depicted schematically in Figure 1.7a.

$$\epsilon_c = \frac{\epsilon_{xx} + \epsilon_{yy}}{2} \tag{1.4}$$

Pure shear strain, which changes the shape of the unit cell without changing the size, takes the form of Eq. 1.5 and is depicted schematically in Figure 1.7b.

$$\epsilon_s = \sqrt{\left(\frac{\epsilon_{xx} - \epsilon_{yy}}{2}\right)^2 + \epsilon_{xy}^2} \tag{1.5}$$

Shear strain has a matrix representation, the *shear matrix,* which takes the form S_{ϕ_s} (Eq. 1.6), and a shear angle ϕ_s (Eq. 1.7).

$$S_{\phi_s} = \cos(\phi_s)\,\sigma_x + \sin(\phi_s)\,\sigma_z \tag{1.6}$$

$$\phi_s = \cos^{-1}\left(\frac{\epsilon_{xy}}{\epsilon_s}\right) \quad 1.7$$

From an experimental perspective, the most accessible ways to uniformly stress a 2D material are by applying biaxial or uniaxial strain. Uniaxial strain, depicted in Figure 1.7c, involves a material stretching along an axis due to stress applied to the same axis. For uniaxial strain along the x-axis, the strain tensor takes the form of Eq. 1.8, where ν is the Poisson ratio, a material-specific parameter ranging from -1 to 1 that describes how much a given material shrinks in the direction transverse to the direction of applied stress.

$$\epsilon_{uniaxial} = \begin{pmatrix} \epsilon_{xx} & 0 \\ 0 & -\nu\epsilon_{xx} \end{pmatrix} \quad 1.8$$

Uniaxial strain can is mathematically a combination of biaxial and shear strain with a shear angle $\phi_s = 90^o$, and it is this strain that will be the focus of Chapter 4 - Chapter 6. While the information in this paragraph is general knowledge, the conceptual outline and specific formulations were adapted from ref. [74].

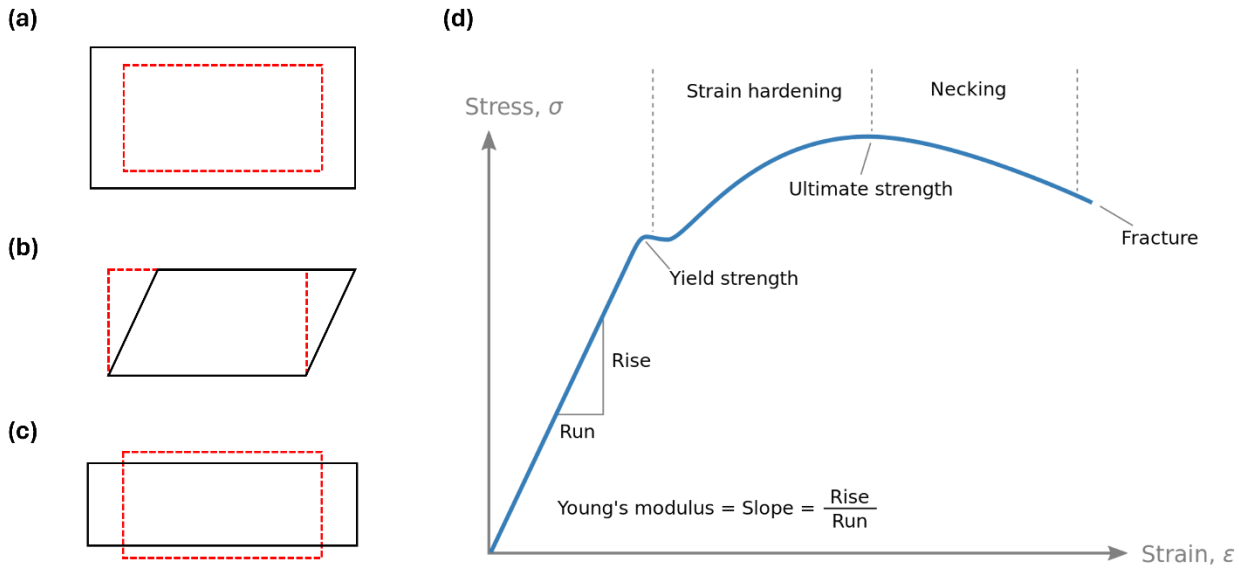

Figure 1.7: Fundamental aspects of strain in 2 dimensions. Depiction of **(a)** biaxial tensile, **(b)** shear, and **(c)** uniaxial tensile strains. The red dotted outline indicates the original shape, while the black outline indicates the shape after said strain is applied. **(d)** Typical stress-strain curve for a material. In the reversible, linear regime at low stress, the linear relationship between stress and strain is defined by the Young's modulus. Panel (d) reproduced from ref. [75].

When a crystalline material is stretched, the elastic energy must be absorbed. At an atomic level, a material strains under stress because the interatomic spacing between atoms increases, changing bond angles and orbital overlap. Typically, crystal defects are the limiting factor that determine the maximum strain that a crystal can experience. Defects, including atomic vacancies, atomic substitutions, line defects, etc., are nucleation sites for tearing because they represent a disruption in the periodic web of ionic or covalent bonds that bind the crystal together. Defect density, consequently, has a significant impact on how much strain a crystal can repeatedly sustain before it yields. 3D bulk materials typically yield at strains below 1%, particularly at cryogenic temperatures, though there are examples of bulk crystals that can sustain much higher strains.

Reduced dimensionality offers two advantages for achieving high strain. First, the increased flexibility of a single atomic layer opens many different avenues for achieving large, local strains that would not be possible for bulk crystals (e.g. conforming over features in a substrate). Second, regardless of defect *density*, which can vary widely in both 2D and 3D crystals, the *overall number* of defects is significantly reduced in an atomically thin crystals. Since defects are naturally weak points in the crystal lattice that nucleate further separation, materials with fewer defects can sustain significantly higher strains[76]. These aspects together have resulted in experimental reports of monolayer MoS_2 withstanding strains of 11% before rupturing at stresses equal to ~11% of the Young's modulus[77], comparable to the theoretical limit of 10% for a defect-free crystal[78]. This corresponds to the point at which the covalent bonds between atoms, not local defects, break to release the elastic energy.

From the perspective of experimental techniques, the approaches to straining 3D crystals and 2D flakes are also naturally different. While 3D crystals are characterized by an indisputable degree of "hardness" or "brittleness", 2D materials evoke images of shear fabrics, flexible membranes, and sheets of paper. Their atomic thickness gives them the flexibility to fold back on themselves many times, roll into spirals, and conform to the shape of a substrate. The conventional technique to apply strain to a bulk crystal involves glueing a flake of crystal on the order of millimeters in length across a gap. To apply strain, this gap is widened, typically either by a manual micrometer or piezoelectric device[79]. This technique can easily apply strains up to fractions of a percent to bulk crystals using conventional and home-built strain apparatuses[79–82]. 2D materials, on the other hand, are not only much thinner than bulk crystals, but typically much smaller. With thicknesses ranging from a single atomic layer (~0.3 nm) to tens of nanometers and lateral

dimensions ranging from 2-5 μm up to hundreds of microns or more, the approaches required to stretch them are distinct.

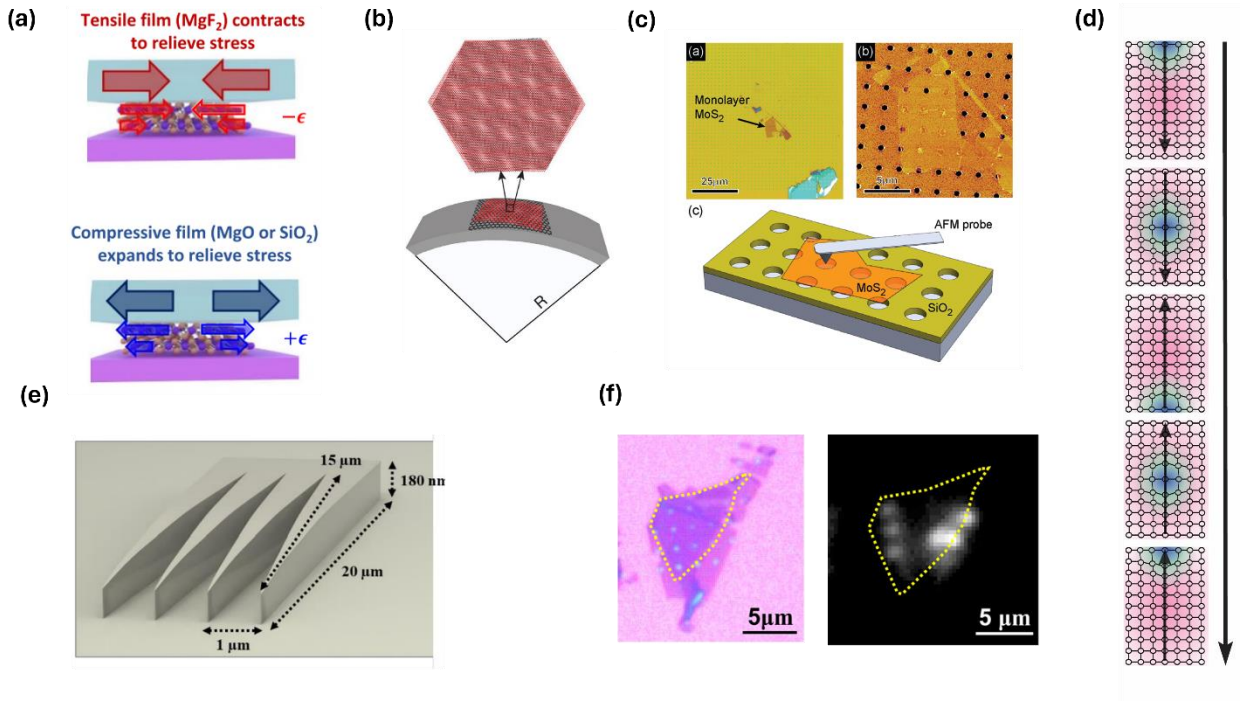

Figure 1.8: Commonly employed techniques to generate strain in 2D materials and 2D heterostructures. (a) A stressed film that either contracts or expands upon contact with the 2D material is applied to the exposed surface to generate compressive or tensile strain. **(b)** The sample is placed on a bendable substrate that can be deformed to create uniaxial tensile strain on the top surface. **(c)** 2D flakes are deposited over cavities and pressed with a narrow tip. **(d)** Ultrafast laser pulses create a localized, dynamic strain pulse in a crystal that traverses the material. **(e, f)** Raised microscale structures are created that generate a specific, localized strain profile in 2D materials or heterostructures that are deposited onto these structures. Panel (a) reproduced from ref. [83]. Panel (b) reproduced from ref. [84]. Panel (c) reproduced from ref. [77]. Panel (d) reproduced from Chapter 3. Panel (e) reproduced from ref. [85]. Panel (f) reproduced from ref. [86]. All panels reproduced with permission.

Experimental approaches for inducing strain vary widely and fall into several different categories with unique advantages and disadvantages. A number of different approaches are depicted in Figure 1.8 and discussed at greater length below. There is instantaneous, or dynamic strain, imparted via a traveling wave of light or sound, and there is persistent strain. There is localized strain induced where a 2D material stretches over an irregularity in the substrate, and there is global strain where a large region of a flake is uniformly stretched. There is fabrication-induced strain, which occurs naturally, either accidentally or intentionally, and there is tunable strain, which can be reversibly and repeatably applied to a sample. There are techniques that work well at room temperature but are incompatible with cryogenic measurements, and there are techniques that work with scanning-probe techniques but not with far-field optics or electrical transport measurements. Appendix D includes **Table 1**, which is a library of 105 recent papers studying strain in graphene, TMDs, or heterostructures of these materials. Of these, 85 are experimental studies, with a particular focus on MoS_2 (29 papers). The choice experimental technique for tunable strain is *bendable substrates* (**Figure 1.8**b), which is employed in 32 of the 85 experimental works. There is also a growing body of work that employs *process-induced* strain, which was a technique borrowed from the silicon industry and developed for 2D materials primarily by Tara Peña in Steven Wu's group at the University of Rochester[83,87–91].

While there is a significant body of literature studying strain in vdW crystals from both theoretical and experimental perspectives, the vast majority of strain experiments are either (1) room-temperature studies of tunable strain on bare flakes[25,66,67,92–127] or (2) cryogenic studies of fabrication-induced strain intentionally or unintentionally added to bare flakes or functional devices[86,89,128–130]. Though somewhat reductive, this categorization captures the fact that the techniques used to apply strain are difficult to implement on electrostatically gated

heterostructures. The first challenge is that state-of-the-art 2D device fabrication, particularly for moiré heterostructures, is predicated on the clean, rigid, smooth, silicon-silicon dioxide substrates that facilitate both device fabrication and measurement. Strain substrates that allow for the application of high strain, on the other hand, are soft, pliable plastics that are bent, stretched, or otherwise deformed to apply a strain. The second challenge is that vdW crystals, by their very nature, are weakly bonded to adjacent layers and do not typically transfer strain efficiently from one flake to the next. Graphene and hBN are particularly "slippery," and in a typical device both flakes would separate the target material from the substrate. In fact, before the discovery of graphene, bulk graphite and TMDs were already heavily used in some industries as dry lubricants[131–133], and since then low-friction and superlubricity have been reported[134–138]. You try building a heterostructure of low-friction lubricants and then stretching it!

One core challenge that this dissertation addresses is whether it is possible to apply large, tunable strains to a high-quality 2D materials device. Typically, the approaches that apply strains to 2D crystals are somewhat incompatible with the device architectures required for high quality devices, particularly when these devices involve moiré superlattices that need atomically smooth substrates and a high degree of homogeneity over the order of hundreds of moiré unit cells (microns).

Chapter 1.1| Outline of Dissertation

In Chapter 2, we begin with a study of surface SHG from topological magnet $MnBi_2Te_4$. In this chapter, we will explore how optical measurements such as SHG are sensitive to the crystal symmetries of 2D materials as well as how magnetism can alter the electronic symmetries relevant for SHG. Though the role of strain was not directly explored in this project, SHG's sensitivity to symmetry makes it an ideal way to quantitatively measure strain in 2D TMDs[24,25]. Furthermore, it

introduces $MnBi_2Te_4$ as an interesting material system in which magnetism, topology, and layer-number intertwine to produce a rich phase diagram worthy of future optical study.

Chapter 3 delves deeper into the ways that ultrafast optical techniques can probe the physics of $MnBi_2Te_4$ and introduces dynamic, localized strain as a potential avenue to control and probe physical properties. It explores how a combination of two different techniques—pump-probe and time-resolved magneto-optical Kerr effect (TR-MOKE) can be used in conjunction to first generate localized, dynamic strain wavepackets that traverse the top and bottom surfaces of a 2D crystal and subsequently to probe the effect of these strain wavepackets on the magnetism of $MnBi_2Te_4$.

In Chapter 4, we shift gears to focus explicitly on applying large, uniform, global strain to 2D materials. In particular, we focus on how a moiré superlattice can be uniaxially strained, and how the effects of this strain can be directly imaged by an atomic force microscope. We also explore how the direct nature of PFM images of the moiré superlattice lend themselves to quantitative analysis of "global" strain using basic FFT techniques and a home-built geometric phase analysis (GPA) algorithm. This chapter sets the stage for subsequent chapters that build toward applying large, tunable strains to fully functional gated moiré heterostructure devices at cryogenic temperatures.

In Chapter 5, the problem of limited strain transfer through vdW crystals (specifically graphene and hBN) and the implications this has for straining 2D devices is addressed directly. Capitalizing on prior experience with high strain-transfer through CrSBr, we show that bismuth oxy-selenite (Bi_2SeO_5), a recently proposed high-κ candidate to replace hBN, provides an atomically smooth, strain-transmitting dielectric layer that makes it possible to achieve flake-wide, reversible, cryogenically tunable strain transfer up to 1% to a gated monolayer flake of WS_2.

Chapter 6 concludes with an as-yet unpublished report of how these developments in strain-transfer and moiré strain tuning can be combined to fabricate high-quality, top gate-tunable moiré superlattice devices that can be uniaxially strained up to 1% at cryogenic temperatures. In doing so, we observe not only the expected redshift in PL from the intralayer and interlayer (IX) excitons, but also a peak splitting in the IX emission. The emergent peak exhibits a distinct dipole moment and degree of circular polarization—features that can only be fully characterized because of the ability to tune the amount of uniaxial strain independently and continuously and/or the electric field/carrier density with an electrostatic gate.

Chapter 2 | Anomalous Second Harmonic Generation from Atomically Thin $MnBi_2Te_4$

This chapter consists of my published work: **Jordan Fonseca**[†], Geoffrey M Diederich[†], Dmitry Ovchinnikov, Jiaqi Cai, Chong Wang, Jiaqiang Yan, Di Xiao, Xiaodong Xu "Anomalous Second Harmonic Generation from Atomically Thin $MnBi_2Te_4$" *Nano Letters* (2022). Aside from minor formatting changes, the work appears as it was published[139]. Author contributions are as follows: X.X conceived the experiment. J.F. prepared samples, assisted by D.O. and J.C. G.M.D. and J.F. performed the RMCD and SHG measurements. C.W. and D.X. verified the SHG theoretical calculations. J.Y. synthesized and characterized the bulk crystals. J.F., G.M.D., D.O., and X.X. analyzed the data and wrote the paper, with input from all authors. All authors discussed the results. J.F. and G.M.D. contributed equally to this work.

$MnBi_2Te_4$ has attracted broad interest in recent years due to its potential to host intertwined intrinsic magnetic and topological properties that persist to the atomically thin limit.[140–146] It is a van der Waals crystal in which each stoichiometric septuple layer (SL) can be thought of as a quintuple layer of Bi_2Te_3 intercalated with an MnTe bilayer (Figure 2.1a).[147,148] The Mn spins in each SL couple ferromagnetically to each other with magnetic moments along the easy *c*-axis; however, exchange coupling causes spins in adjacent layers to anti-align, giving rise to A-type AFM ordering below the Néel temperature of $T_N \approx 25\,K$.[140,146] The interplay of thickness, magnetic state, and band topology conspire to produce a rich topological phase diagram. $MnBi_2Te_4$ is predicted to host a trivial magnetic insulator in 1 SL flakes, the zero-plateau quantum anomalous hall effect or "axion insulator states" in thin even-layer flakes, and quantum anomalous hall (QAH) states in thin odd-layer flakes.[149]

Despite the excitement precipitated by this theoretical work, robust and consistent experimental evidence for $MnBi_2Te_4$'s thickness dependent physics has remained elusive. Shortly after the initial theoretical prediction,[149] the material was synthesized in bulk crystal form and confirmed to be the first AFM topological insulator.[147,148] Subsequent experimental works on atomically thin flakes partially confirmed initial predictions, with the observation of the QAH effect in a 5 SL device[145] and transport signatures of the axion insulator state in 6 SL samples.[150] Nevertheless, reproducing the QAH effect has been difficult. Instead, quantized transport in the field induced ferromagnetic state has been repeatedly observed and become a robust phenomenon in both even- and odd-layer samples. Thus, the nature of $MnBi_2Te_4$'s layer-dependent topological and magnetic states remains an open question.

Besides numerous transport studies indicating similar magnetic-state-dependent topological properties of even- and odd-layer number samples,[142,150–156] ARPES measurements provide inconclusive results regarding whether the surface state is gapped at zero magnetic field.[157–159] These experimental incongruities might be related to the impact of atomic defects on magnetism,[160] defect-induced surface reconstruction in few-layer samples,[161] or a possible exfoliation-induced structural or magnetic phase transition,[162–164] all of which could alter the expected layer-dependent magnetism and topology of the studied samples. This situation calls for a non-invasive probe that is sensitive to $MnBi_2Te_4$'s layer-dependent structural, magnetic, and surface symmetries.

Optical second harmonic generation (SHG) is an ideal tool to investigate $MnBi_2Te_4$'s structural and magnetic properties. Within the 2D materials field, SHG arising from structural inversion symmetry breaking has found utility as a non-invasive means to optically identify crystal axes,[19,22] measure strain,[25] and identify relative twist-angle in layered materials.[165–168]

Furthermore, inversion symmetry can be broken by an A-type AFM order (Figure 2.1b), leading to so-called *c-type* SHG. It has been employed to explore structural and magnetic properties of a variety of materials including bulk Cr_2O_3,[169] atomically thin $MnPS_3$,[170] bilayer CrI_3,[171] and monolayer $MnPSe_3$.[172] Studies have shown that $MnBi_2Te_4$ crystalizes in the centrosymmetric $R\bar{3}m$ (D_{3d}^5) space group.[173–175] With A-type AFM magnetic ordering included, this becomes the magnetic space group R_I-*3c* [176] with the crystal and magnetic structure depicted in Figure 2.1a, b. In even (odd) layers, strong (zero) *c-type* SHG is predicted,[177] making optical second harmonic generation a feasible probe of both AFM order and the symmetries of the underlying crystal structure with particular sensitivity to the surface.

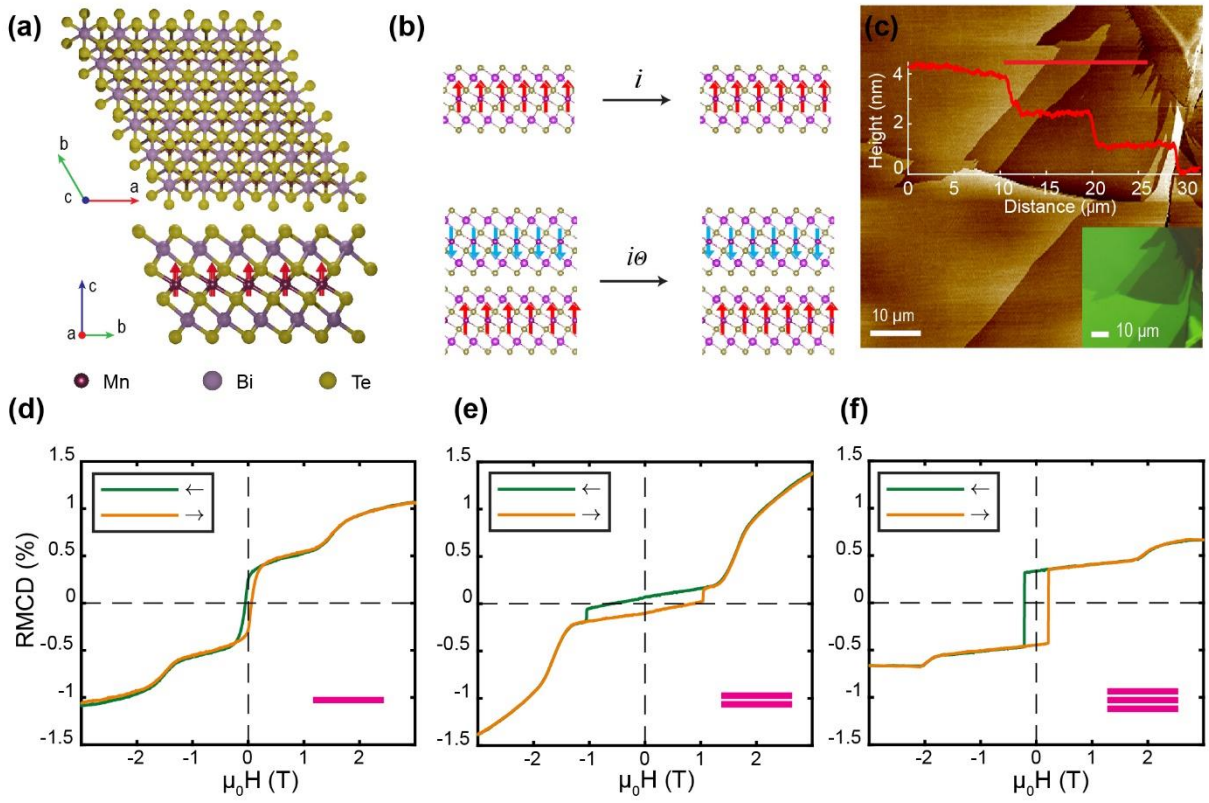

Figure 2.1: $MnBi_2Te_4$ crystal structure and magnetic ordering. (a) $MnBi_2Te_4$ crystal structure. **(b)** Schematic showing how symmetry is preserved (broken) in odd (even) layer crystals. Red/blue arrows indicate the magnetic ground state below the Néel temperature. **(c)** Atomic force

microscope image of $MnBi_2Te_4$ flakes down to a monolayer with linecut of 1 SL, 2 SL, and 3 SL steps taken along red line. Inset shows optical image of the same region. **(d)-(f)** RMCD sweeps of 1 SL, 2 SL, and 3 SL flakes measured at ~4.5 K. Magenta insets indicate $MnBi_2Te_4$ layer number measured in each plot.

In this work, we perform polarization resolved SHG and polar reflectance magnetic circular dichroism (RMCD) measurements on $MnBi_2Te_4$ flakes ranging in thickness from bulk to monolayer. Contrary to our expectations, we find that the observed SHG is independent of magnetic state, temperature, exfoliation substrate, or crystal thickness. We conclude that any *c-type* SHG arising from the AFM ordering is obscured by a much stronger signal that likely arises from the interface between $MnBi_2Te_4$ and vacuum. Our findings are consistent with the expected structural symmetry of $MnBi_2Te_4$ and call for additional studies to address the underlying reasons for the absence of observation of *c-type* SHG.

After preparing 1 - 4 SL flakes of $MnBi_2Te_4$ (Figure 2.1c, Methods), we characterize the layer-dependent magnetic state using RMCD, which is a sensitive optical probe of out-of-plane magnetization for 2D materials.[12] We demonstrate that our layer assignment, magnetization curves, spin-flip coercive fields, and spin-flop/spin-canting fields are consistent with existing literature (Figure 2.1d-f, Figure 2.8a).[143,146] We then employ polarization resolved SHG measurements on the same 1 - 4 SL flakes characterized with RMCD to compare their magnetic state with their SHG response. We measure the co-linear (XX) and cross-linear (XY) SHG response in Faraday geometry, which enables us to maximally probe the elements of the nonlinear susceptibility tensor given the normal incidence restrictions of our measurement apparatus.

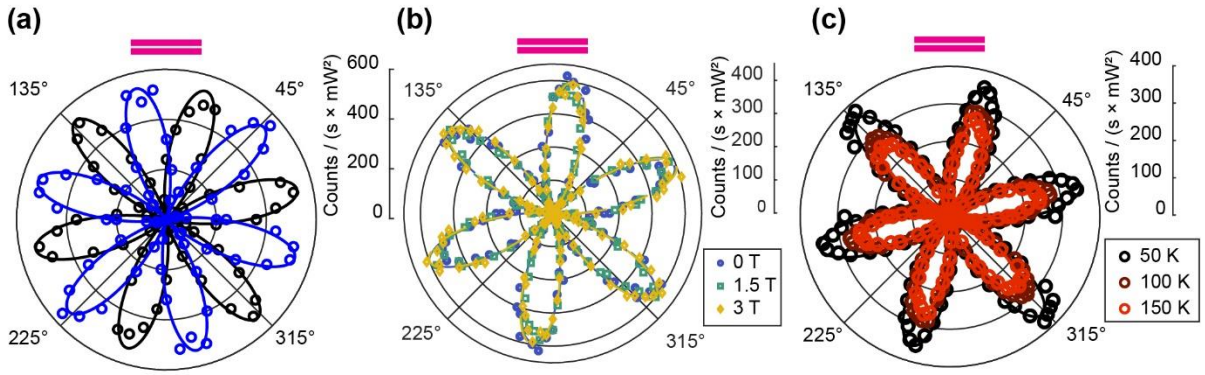

Figure 2.2: 2 SL $MnBi_2Te_4$ magnetic field and temperature dependent SHG. (a) Polarization-resolved SHG from 2 SL $MnBi_2Te_4$ with no applied field below the Néel temperature. Black (blue) dots are co(cross)-linearly polarized experimental data with solid line fits to Eq. 1 (Eq. 2). XY data are excluded from subsequent subfigures for clarity. **(b)** Out-of-plane magnetic field dependence of the SHG. **(c)** Temperature dependence of the SHG above T_N. Magenta insets indicate $MnBi_2Te_4$ layer number measured in each plot. All data in (b) and (c) are taken at a cryostat base temperature of ~4.5 K, and only XX data are shown for clarity.

At first glance, the SHG response from 2 SL $MnBi_2Te_4$ is consistent with the theoretical prediction (Figure 2.2a). A six-fold pattern emerges in both XX and XY channels, which have identical amplitudes and can be fit well by the predicted theoretical model based on AFM time reversal symmetry breaking (Appendix A).[177] Unexpectedly, the observed pattern remains unchanged under applied magnetic field up to 3 T (Figure 2.2b), which is above the 2 SL spin flop field of ~2 T.[143,146] For an SHG signal arising from AFM ordering that breaks inversion symmetry, we expect a change in the underlying magnetic state to manifest as a change to the shape or amplitude of the SHG rotational anisotropy. Experimentally, we do not see this change, which suggests that time reversal symmetry breaking is not the mechanism that explains the observed signal. We more conclusively demonstrate the independence of the measured SHG signal on magnetic ordering with temperature-dependent measurements. As shown in Figure 2.2c, the SHG

anisotropy and amplitude from the 2 SL remain nearly unchanged up to 150 K (Figure 2.2c) which far exceeds the Néel temperature of ~25K.

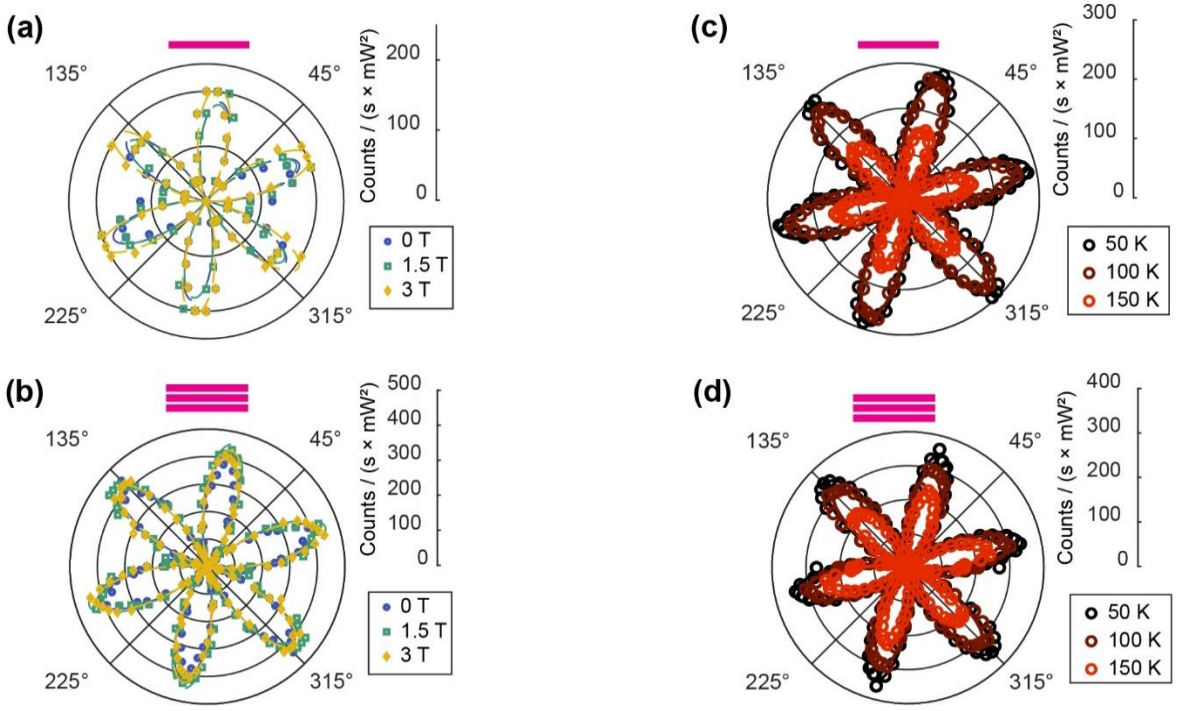

Figure 2.3: 1 SL & 3 SL magneto- and temperature dependent SHG. Dependence of the XX SHG on an out-of-plane magnetic field for 1 SL **(a)** and 3 SL flakes **(b)** at a base temperature of ~4.5 K. Temperature dependence of the XX SHG for 1 SL **(c)** and 3 SL **(d)** flakes above T_N. Magenta insets indicate $MnBi_2Te_4$ layer number. XY data, which exhibit the same behavior, are omitted for clarity.

We observe nearly identical behavior in 1 SL and 3 SL samples. Regardless of magnetic state, all odd-layer flakes of $MnBi_2Te_4$ possess an inversion center located at the middle Mn layer, which should make these layers second-harmonic dark. Surprisingly, we find that the SHG from 1 SL and 3 SL flakes is as strong as that from the 2 SL with identical polarization dependence. As with the 2 SL flake, SHG from 1 SL and 3 SL samples exhibits no magnetic field dependence up to 3 T (Figure 2.3a, b) and remains unchanged at temperatures far above the Néel temperature

(Figure 2.3c, d). Therefore, the observed SHG has no magnetic origin. A 4 SL sample also exhibits nearly identical behavior (Figure 2.8). The fluctuations in intensity observed in the temperature dependence data do not reflect a real change in the sample, but rather imperfect experimental conditions across the wide temperature range.

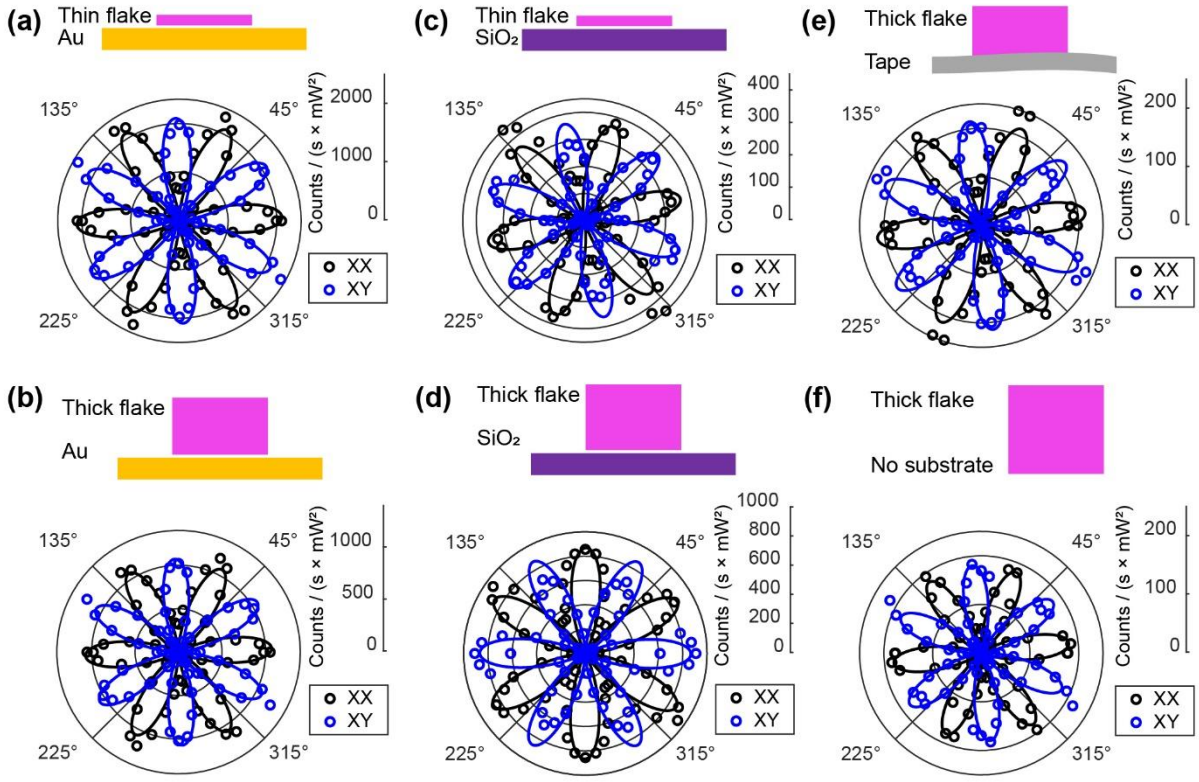

Figure 2.4: Thickness and substrate dependence of polarization resolved SHG. Polarization-resolved SHG from **(a)** a few-layer flake on Au, **(b)** a bulk flake on Au, **(c)** a few-layer flake on SiO_2, **(d)** Bulk flake on SiO_2, **(e)** a bulk flake cleaved on Scotch tape before exfoliation, and **(f)** a pristine bulk flake oriented to have the beam incident on the (0001) surface. All data are taken at cryogenic temperature with no applied magnetic field. Black (blue) dots are co(cross)-linearly polarized experimental data with solid line fits to Eq. A.1 (Eq. A.2).

To ensure that our fabrication methods have not introduced any unwanted signal contributions, we explore how the SHG from $MnBi_2Te_4$ depends on flake substrate and crystal

thickness. For example, charge transfer between the Au substrate and the atomically thin $MnBi_2Te_4$ flakes we measured could result in a symmetry breaking electric field arising within the crystal.[178] To understand the impact this effect has on our data, we compare the SHG from thin and thick flakes exfoliated onto either Au or SiO_2 (Figure 2.4a – d). Although there is variation in intensity across the plots shown, no pattern emerged in our measurements that would allow us to identify a consistent trend between flakes exfoliated on gold versus SiO_2. Crucially, choice of substrate does not explain the presence of the SHG signal that we observe. Finally, we rule out an exfoliation-induced structural transition by performing SHG measurements at various stages of our flake preparation. We measure SHG from the (0001) surface of bulk $MnBi_2Te_4$ (Figure 2.4f) as well as from flakes that have been cleaved onto scotch tape but not deposited onto any substrate (Figure *2.4*e). We find that the SHG from unexfoliated bulk flakes is typically ~5 times weaker than that measured from exfoliated bulk flakes, but that otherwise the shape and presence of $MnBi_2Te_4$'s rotational anisotropy SHG response is independent of crystal thickness, exfoliation substrate, and exfoliation process. At 800 nm, the nonlinear susceptibility of exfoliated bulk $MnBi_2Te_4$ is ~50 times weaker than the susceptibility of monolayer WSe_2 (Figure 2.5). While the five-fold change in the SHG intensity across a wide variety of sample thicknesses and preparation methods may be indicative of some symmetry-breaking process that occurs during the exfoliation, it does not explain the presence of SHG in the remainder of our measurements.

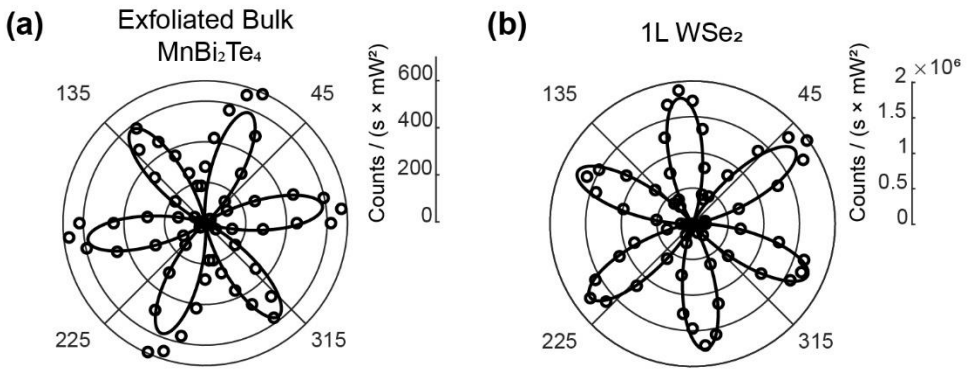

Figure 2.5: Comparison of SHG intensity from $MnBi_2Te_4$ and WSe_2. Polarization resolved SHG from **(a)** exfoliated bulk $MnBi_2Te_4$ and **(b)** 1L WSe_2 showing that the normalized intensity of SHG from $MnBi_2Te_4$ is approximately 3,000 times weaker than that from 1L WSe_2. All data are taken in the same experimental conditions other than excitation power, which was 850 μW in (a) and 600 μW in (b).

Our experimental results conclusively reveal that the dominant second harmonic response of $MnBi_2Te_4$ crystals of all thicknesses under 800 nm excitation is unrelated to the material's magnetic properties. Rather, the system exhibits a layer-, magnetic-state-, and temperature-independent response which cannot arise from the centrosymmetric crystal structure of both bulk and monolayer flakes. We note that our experiment does not preclude the existence of the predicted *c-type* SHG, which might be much stronger for mid-IR excitation wavelengths.[177] If there is any c-type SHG, any additional contribution this makes to the dominant *i-type* signal cannot be resolved in our measurements. More specifically, this may be because our excitation energy of ~1.55 eV (800 nm) is much smaller than the spin splitting between the Mn *d*-bands[179] that would give rise to a strong *c-type* SHG signal.

The unexpectedly strong and magnetic-state-independent SHG response of $MnBi_2Te_4$ calls for further investigation into the origin of this signal. SHG in centrosymmetric crystals can arise

from magnetic dipole or toroidal moments,[180] though we rule out any magnetic contributions to our signal on the grounds that these contributions would depend on applied magnetic field and temperature, contrary to our observations. For a more plausible explanation of the origin of the anomalous SHG signal, we look to $MnBi_2Te_4$'s parent materials Bi_2X_3 (X = Te, Se), both of which exhibit SHG arising from the inversion symmetry broken surface of the crystal where the crystallographic point group symmetry is reduced from D_{3d} to C_{3v},[178,181] as is the case for $MnBi_2Te_4$. In Bi_2Se_3, rotational anisotropy and surface oxidation dependent SHG measurements confirm that the six-fold SHG pattern originates from the anharmonic hyperpolarizability of the Bi-Se and Se-Se bonds at the surface.[178] SHG from $MnBi_2Te_4$ also exhibits strong dependence on the surface oxidation (Figure 2.6) as well as a rotational anisotropy consistent with the C_{3v} point group. Both facts point toward anharmonic polarizability of the in-plane Te-Te bonds at the crystal surface as the main source of the SHG reported here. Because the point group symmetry at an interface is related to the bulk material's point group, our surface SHG measurements corroborate $MnBi_2Te_4$'s expected crystal structure and stacking order.

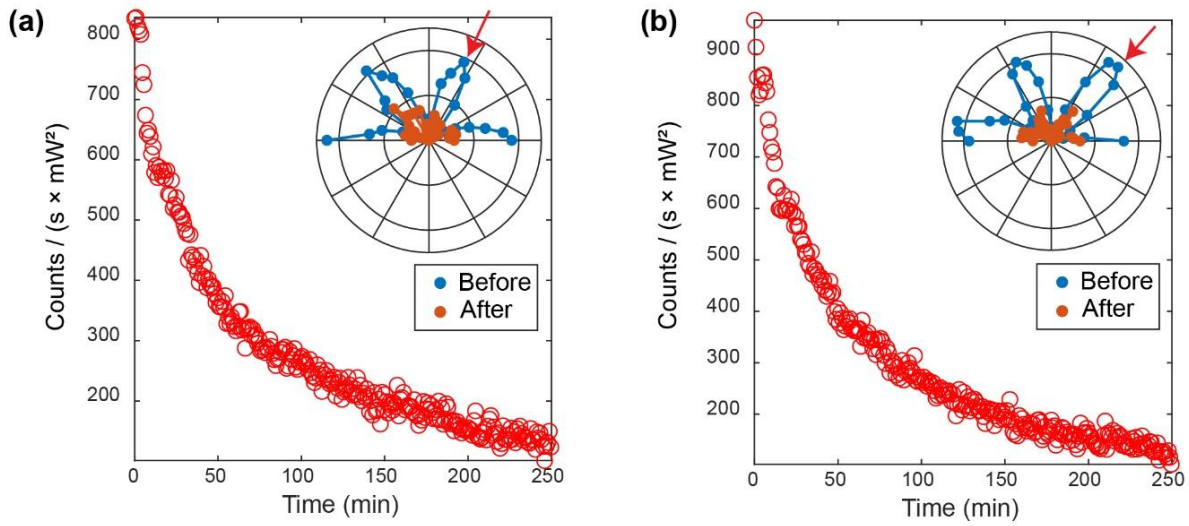

Figure 2.6: Effect of $MnBi_2Te_4$ surface degradation on SHG. Data shown in each panel taken from a different flake. Insets show a polarization resolved measurement before (blue) and after (orange) the time-dependent measurement. For the exposure time dependence, the SHG was collected at the polarization marked in the inset with a red arrow. SHG intensity decreases dramatically within the first 60 minutes following exfoliation.

In conclusion, we use RMCD to characterize the layer dependent magnetic ordering of few-layer $MnBi_2Te_4$ down to a monolayer. We subsequently employ polarization resolved magneto- and temperature dependent SHG to show that, contrary to expectations, the measured SHG pattern at 800 nm excitation is independent of the material's magnetic ordering and layer thickness. We emphasize that our most important finding is that the SHG generated from widely available Ti:sapphire sources does not probe AFM magnetic order in $MnBi_2Te_4$, but rather likely arises from an inevitable structural symmetry breaking at the crystal surface. Our results lay the experimental groundwork for nonlinear optical probe of the magnetic and structure properties in topological antiferromagnet $MnBi_2Te_4$.

Methods

Crystal growth and sample preparation

$MnBi_2Te_4$ bulk crystals were grown out of a Bi-Te flux as previously reported.[182] All samples were prepared inside an Argon-filled glovebox. We isolate thin flakes using standard scotch-tape exfoliation technique. To reliably procure flakes down to monolayer thickness, we evaporate a ~2 nm layer of Cr or Ti followed by a ~ 3 nm layer of Au onto 285 nm thick SiO_2/Si wafers and use the gold assisted exfoliation technique.[183,184] Optical and atomic force microscope images of few-layered flakes (Figure 2.1c) were taken inside the glovebox before sealing flakes in a copper spacer and transferring them to a cold-finger 4 K cryostat for measurement. The schematic crystal structures in Figure 2.1a and Figure 2.1b were drawn using VESTA.[185]

Optical measurements

All optical measurements were performed with light normally incident on the (0001) surface of the crystal. Measurements were conducted in a variable temperature cryostat including a superconducting magnet in Faraday geometry (Montana Instruments). The polar RMCD measurements were performed with a 632.8 nm HeNe laser, which was intensity-modulated by a mechanical chopper and polarization-modulated by a photoelastic modulator (Hinds PEM100). HeNe laser power was kept below 1 μW for all measurements. The SHG measurements were performed using femtosecond pulses from a 76 MHz Ti:sapphire oscillator (Coherent Mira 900F). The central output wavelength was chosen to be 800 nm for most measurements. The beam was focused onto the sample by a microscope objective (Olympus LUCPLFLN40X), which also collected the second harmonic signal. SHG is typically detected using a photomultiplier tube (Hamamatsu H8259) connected to a Time Interval and Frequency Counter (Stanford Research SR620). Polarization-resolved measurements were achieved by rotating the incident and collected beams together using a half-wave plate, while an additional half-wave plate and polarizer in the

collection path allow for independent measurement of colinear (XX) and cross-linear (XY) SHG. The measurement is corrected for Faraday rotation in the objective and cryostat window by adjusting the rotation angles of the two waveplates based on calibrated measurements of the wavelength dependent Faraday rotation. To ensure that laser-induced heating does not melt magnetic ordering, we perform RMCD measurements at various ultrafast excitation powers and establish that at a cryostat base temperature of ~ 4.5K, laser powers below 500 μW do not locally heat the sample above T_N (Figure 2.7). To expedite measurements, all SHG data (except those shown in Figure 2.5b) were collected for 180° of polarization. Data taken at angle θ were then duplicated to angle $\theta + 180^o$. The validity of this approach was experimentally verified intermittently throughout our measurements.

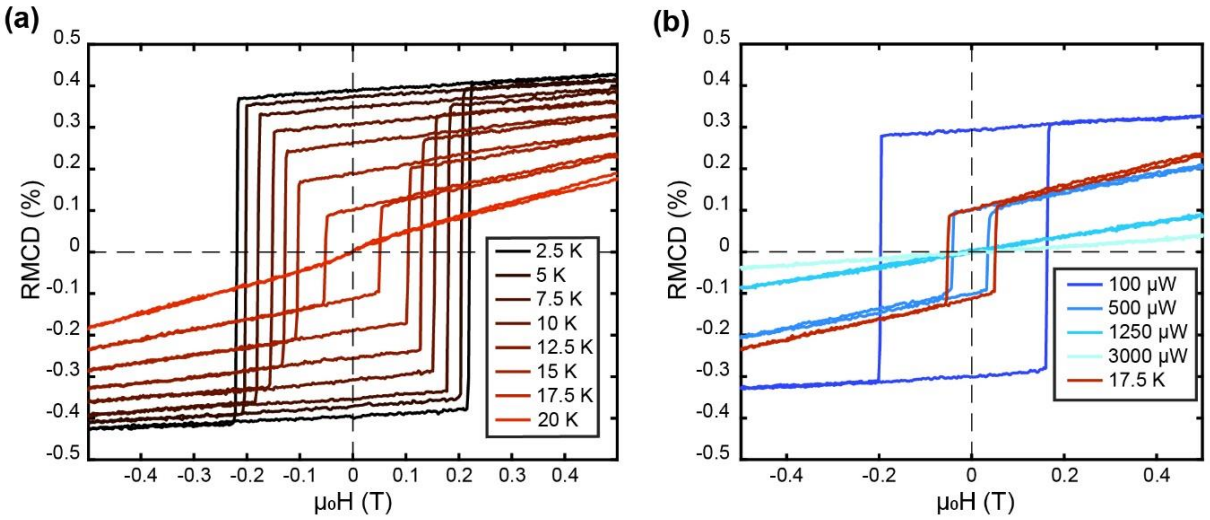

Figure 2.7: Temperature and power dependent RMCD. (a) Temperature dependent RMCD around the central hysteresis loop for a 3 SL sample. (b) RMCD signal for the same 3 SL measured as a function of ultrafast laser power when the SHG excitation beam is also on the sample. These data are overlapped with the RMCD data taken at 17.5 K when no ultrafast pulses were present.

Below 500 μW, the local heating from the ultrafast beam does not raise the temperature of the 3 SL above its Néel temperature.

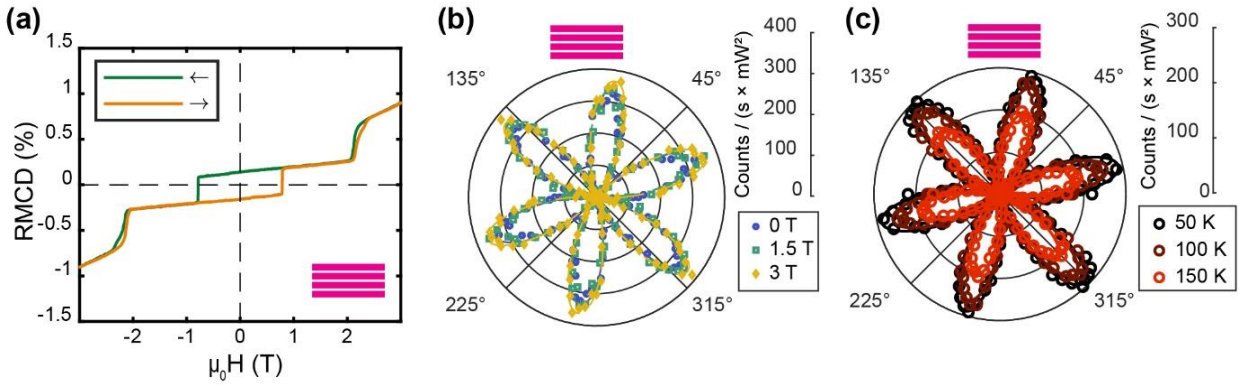

Figure 2.8: RMCD & SHG from a 4 SL sample. (a) RMCD from a 4 SL flake of $MnBi_2Te_4$ exfoliated on gold. **(b)** Magnetic field dependence of XX SHG from showing no change up to 3 T. **(c)** Temperature dependence of XX SHG flake showing a weak change in intensity of signal at higher temperatures, which we attribute to experimental artifacts.

Chapter 3 | Picosecond Ultrasonics in Topological Magnet $MnBi_2Te_4$

This chapter consists of my submitted work: **Jordan Fonseca**†, Geoffrey M Diederich†, Dmitry Ovchinnikov, Jiaqiang Yan, Di Xiao, Xiaodong Xu "Picosecond Ultrasonics in Topological Magnet $MnBi_2Te_4$" *in review, Nano Letters* (2024). Aside from minor formatting changes, the work appears as it was submitted. Author contributions are as follows: X.X. and G.M.D. conceived the experiment. J.Y. synthesized bulk crystals. J.F. prepared exfoliated samples and performed atomic force microscopy measurements, assisted by D.O. J.F. and G.M.D. performed the optical measurements. G.M.D., J.F., D.O., and X.X. analyzed the data and wrote the paper, with input from all authors. All authors discussed the results. J.F. and G.M.D. contributed equally to this work.

Introduction

In crystalline structures, the density, type, and location of defects have a significant impact on the material's physical properties. Consequently, developing metrology techniques to probe structural properties and diagnose these defects is a core goal of materials science and engineering. $MnBi_2Te_4$ is an archetypal example of a quantum material in which the intertwined magnetic, topological, and electronic properties sensitively depend on crystal quality. This material platform has generated intense interest as the first intrinsically magnetic topological insulator[147–149] with potential to exhibit exotic quantum phenomena such as the quantum anomalous hall effect[186] and axion insulator state[150]. Additionally, it hosts interesting electron-phonon and spin-lattice coupling[187,188]. In the years following $MnBi_2Te_4$'s synthesis, it was shown that Te-vacancies could induce a surface structural collapse[161]. Mn-Bi anti-site defects also have a significant impact on the material's magnetic and topological properties[189–191]. Subsequent STM work on $MnBi_2Te_4$[192,193] and on the analogous alloy $MnBi_{2-x}Sb_xTe_4$[194,195] have further established the connection between defect type and distribution and the resultant impact on critical properties such as the Dirac cone on the topologically gapped surface. More recently, stacking faults were predicted to have significant impact on the topologically nontrivial surface states and may reconcile the findings of both gapped and gapless surface states in few-layer $MnBi_2Te_4$[196]. The intimate relationship between crystal defects and topological order in these materials encourages development of new metrology techniques that can identify subsurface defects.

While scanning probe experiments have evolved to provide atomic resolution of crystal surfaces and made the precise identification of atomic defects on the surface of $MnBi_2Te_4$ possible, detecting stacking faults buried deep within the van der Waals structure is challenging. Nevertheless, because of $MnBi_2Te_4$'s A-type AFM interlayer coupling between adjacent layers, identifying the presence of these faults may be important for device performance and magnetic

properties. Although techniques such as cross-sectional high-angle annular dark-field scanning transmission electron microscopy (HAADF-STEM) can provide a side-on image of a van der Waals crystal with atomic resolution[8], utilizing such a technique requires vertically milling the crystal and subsequently provides an image of only a narrow slice of the freshly cut surface. This approach damages the sample and may still miss localized stacking faults if they are not present at the milled surface. Ultrasonic force microscopy is sensitive to subsurface features[197,198]; however, this technique requires an atomic force microscope, which is challenging to implement in a cryogenic environment. It also applies force to the crystal structure and can introduce layer shearing in vdW materials. It would thus be desirable to employ a non-destructive optical metrology technique for identifying stacking faults among other structural properties *in-situ* under a wide variety of experimental conditions. Such a technique could advance the understanding of how structural changes alter $MnBi_2Te_4$'s quantum properties while providing a more versatile tool for defect metrology of a wider variety of van der Waals materials.

Picosecond ultrasonics (PU) emerged in the 1980s as a method to probe mechanical and acoustic properties of materials with high spatial and temporal resolution[199–201]. Typically implemented via an optical pump-probe experiment, the technique consists of first generating a strain wavepacket comprised of coherent acoustic phonons with an ultrafast pump pulse. The wavepacket propagates through the sample, modulating the local optical and structural properties of the medium through which it passes. Subsequent changes in reflectivity can be monitored by a time-delayed probe pulse (Figure 3.1a). This technique has been employed to measure fundamental mechanical properties such as the speed of sound[202,203], anisotropic stiffness coefficients[204], strain generation mechanisms[205], and phonon lifetimes[202] in a wide variety of materials, as well as how these properties depend on experimental parameters such as

temperature[199,200,206]. Furthermore, PU has been used to identify defects such as subsurface monolayers[207,208] or grain boundaries[209] in thin films and thus emerges as a natural choice for defect characterization in van der Waals materials.

PU inherits its micron lateral spatial resolution and nanometer vertical spatial resolution from the small beam spot size and sub-picosecond temporal resolution of optical pump-probe measurements. It is thus suited for nano- and meso-scale samples that may be too small or too thin to accommodate other techniques. In the past, PU has been used to characterize nanomechanical resonator cavities fabricated from silicon[210] and 2H-$MoSe_2$[211], to measure the interlayer elastic properties of exfoliated bulk $MoSe_2$ and WSe_2[202], for THz phononic engineering in suspended van der Waals heterostructures[212], and as an acoustic tomography tool for heterostructures fabricated from monolayer WSe_2 encapsulated in hBN[33]. While these studies have lain important groundwork by introducing PU to the field of 2D materials[202,203,211,213–215], the possibilities for this technique have not been fully explored. So far, PU studies of van der Waals (vdW) materials have focused on transition metal dichalcogenides, which have been the subject of intensive research for over a decade. One appealing aspect of the field of 2D materials, however, is the ability to realize and control a broad range of materials and phases of matter (e.g. insulators, metals, semiconductors, superconductors, and magnets) in the 2D limit. Understanding how picosecond strain pulses interact with these phases of matter could provide a new probe of a wide variety of order parameters that are sensitive to how strain modifies crystal structure and material properties.

In this work, we employ picosecond ultrasonics on exfoliated $MnBi_2Te_4$. Unlike similar studies, we do not suspend our samples over cavities[210–212] or evaporate a metal transduction layer onto the sample[213], which simplifies our fabrication procedures (Methods). We show that thin-slab (100-200 nm) $MnBi_2Te_4$ is an excellent acoustic phonon cavity. By measuring the acoustic phonon

wavepackets, we can determine the crystal thickness, identify stacking faults in the $MnBi_2Te_4$ crystal, and measure their depths with nanometer precision *in situ*. Additionally, we show that the magnetic ordering in $MnBi_2Te_4$ does not couple to these out-of-plane vibrations through magnetostriction by simultaneously performing magneto-optical measurements. Despite the unique capabilities of this technique and its recent application to vdW materials, the results described in this work are the first report of these acoustic strain pulses in a topological quantum material.

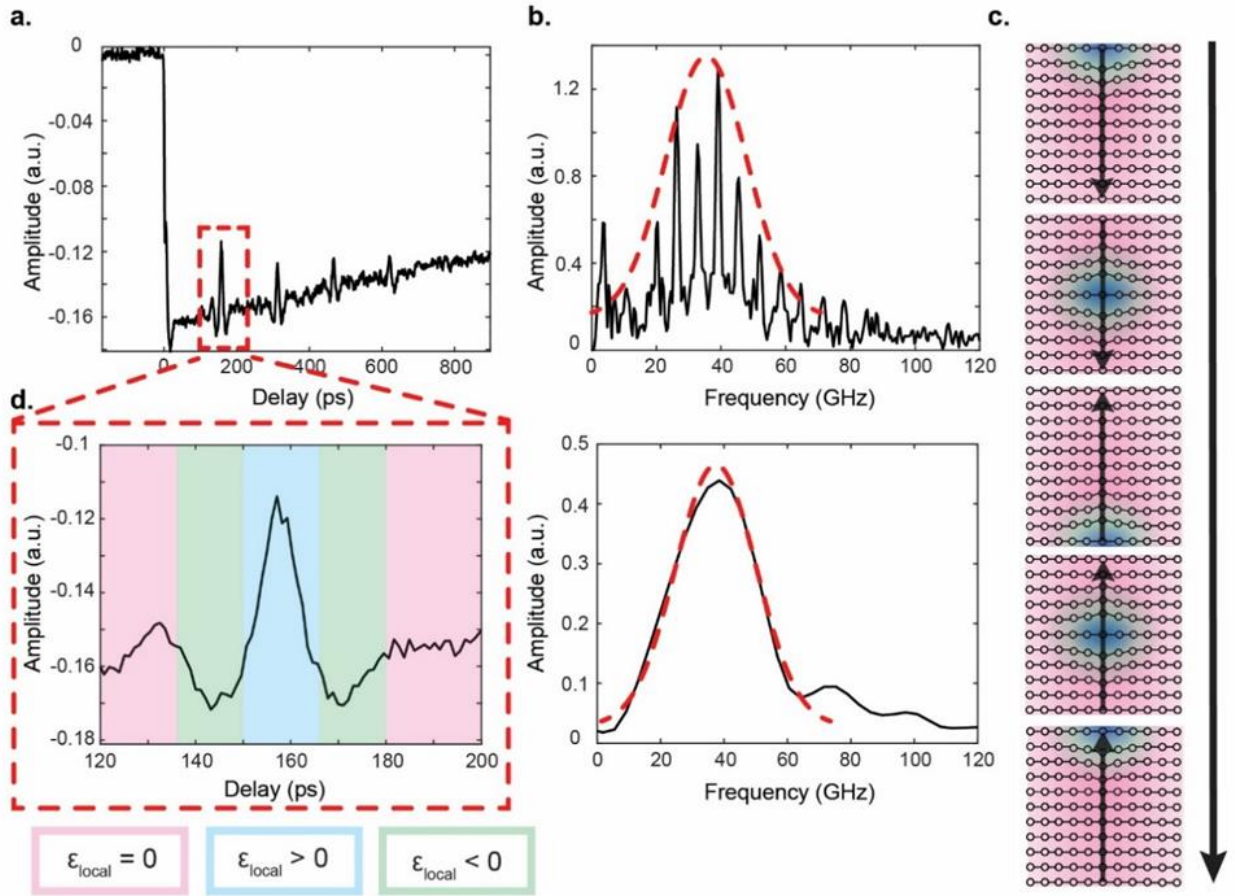

Figure 3.1: Formation of the acoustic frequency comb. (a) Time trace of transient reflectivity as a function of delay time between pump and probe pulses showing periodic spikes in addition to the typical exponential decay. **(b)** FFT of the time trace shown in (a) highlighting the sharp comb

teeth that emerge in the frequency domain. Red dashed line is a guide to the eye of the comb's gaussian envelope. **(c)** Cartoon of the strain pulse (shaded blue for tensile strain, green for compressive strain, and red for unstrained) forming at the top surface of the crystal, propagating through the material, and reflecting from the bottom interface. The thick black arrow to the right of the cartoon indicates time increasing downward. **(d)** Expanded view of a single strain pulse in time (left) and the associated FFT (right) with color shading corresponding to tensile, compressive, or zero strain as in (c), and highlighting that the individual comb teeth are lost when only a single temporal pulse is Fourier transformed.

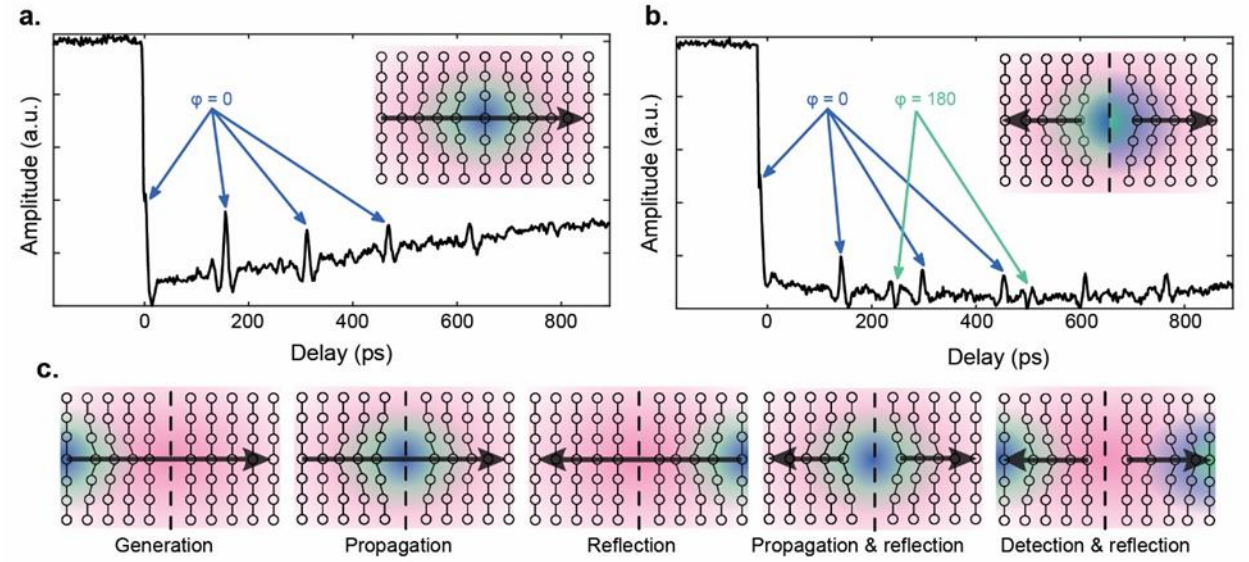

Figure 3.2: Identification of vertical stacking faults from pulse timing and phase. (a) Time trace of transient reflectivity from a fault-free flake showing a single train of identically phased pulses. **(b)** Time trace of transient reflectivity from a different flake of similar thickness that hosts two sets of periodic pulse trains that are out of phase with each other and temporally offset by ~100 ps. The phase-flipped and temporally offset train of pulses arise from a partial reflection of the strain pulse off a stacking fault located 42 nm below the top surface of the crystal. **(c)** Cartoon

illustration of how a stacking fault causes a partial reflection of the strain wavepacket within the crystal. Cartoon insets of (a) and (b) depict the distinct real-space pictures of how a defect causes partial reflection of the pulse within the crystal bulk.

We begin by presenting the formation of a phonon frequency comb through the addition of cavity modes in a thin bulk flake of $MnBi_2Te_4$. For these measurements, we employ 100 kHz amplified pulses (< 200 fs FWHM) from a 76 MHz oscillator split into a broadband pump ranging from 490 nm to 530 nm and a probe at 800 nm. Pump and probe powers were 6 μW and 4 μW, respectively, and the sample was held at 10 K in an optical cryostat. Figure 3.1a and Figure 3.1b show the transient reflectivity data and its Fourier transform. The time domain data clearly show a series of peaks superimposed on the typical exponential decay seen in time resolved optical reflectivity experiments. These peaks correspond to the arrival of the phonon wavepacket at the sample surface after a round trip through the crystal (shown in Figure 3.1c), where the strain-induced change to the local optical properties is measured by a change in reflectivity of the probe pulse. The frequency domain data show a microwave frequency comb whose sharp peaks correspond to the acoustic phonon cavity modes that contribute to the strain wavepacket. Figure 3.3a-c shows an 8-peak Lorentzian fitting of the comb teeth and the extracted quality factor Q and product $f \times Q$ for the series of cavities modes spanning the 80 GHz comb bandwidth. At 60 GHz, Q>30, while $f \times Q \approx 2$ THz, which far exceeds the characteristic thermal frequency of $k_B T/h = 300\ GHz$ at 10 K.

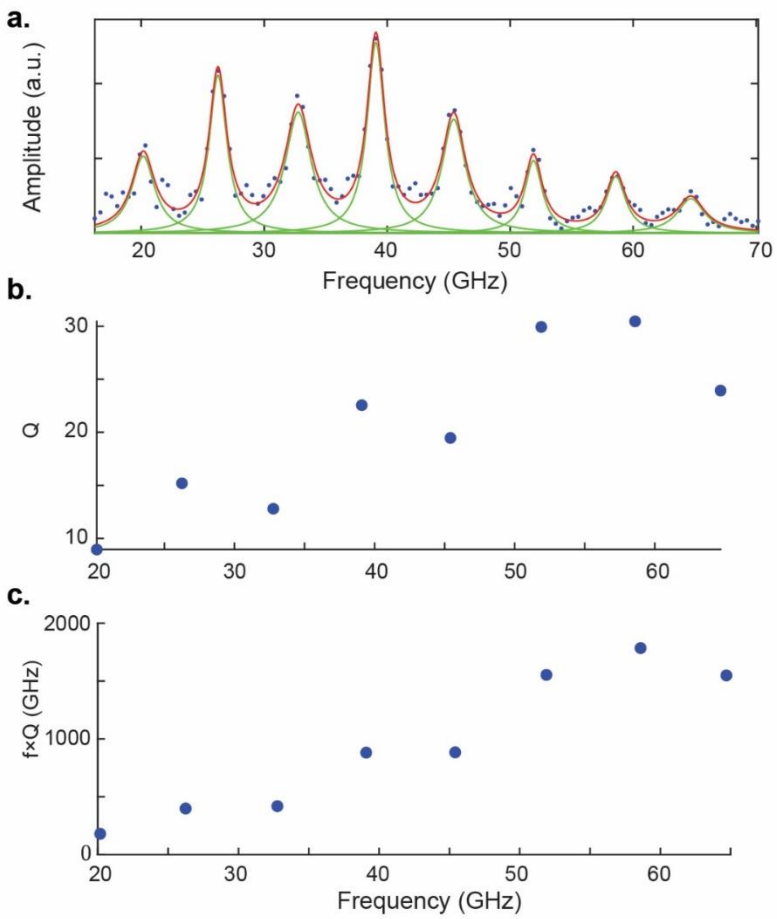

Figure 3.3: Characterization of the frequency comb in $MnBi_2Te_4$ cavities. (a) Frequency comb for the data presented in **Figure *3.1***, fit with an 8-peak Lorentzian to identify the mode frequencies f and FWHM df. **(b)** Calculated quality factor ($Q = f/df$) versus frequency for each mode. **(c)** Calculated $f \times Q$ product for the same data in (b).

Figure 3.1d zooms in on the first time-domain peak, where the local strain at a given delay time has been color coded. Its Fourier transform consists of a Gaussian phonon distribution. Here, the frequency comb has been lost due to the limited resolution present in the FFT of such a short time signal. This loss of frequency-domain resolution when only a single pulse can be Fourier transformed emphasizes that it is the cavity-nature of repeated, periodic acoustic reflections that

make it possible to resolve the thickness-dependent cavity modes in $MnBi_2Te_4$ that comprise the frequency comb and study their interaction with the material's magnetic order.

Since the inception of PU, the technique has been most directly employed to measure the acoustic properties of materials and to identify subsurface structures in layered materials. Using a combination of atomic force microscopy (AFM) to measure flake thickness d_{MBT} and PU to measure roundtrip phonon travel time Δt, we experimentally determine the speed of sound in $MnBi_2Te_4$ to be $v_s = 2d_{MBT}/\Delta t = 2.447$ km/s (Methods, Figure 3.6). Throughout the rest of this work, we calculate thickness of $MnBi_2Te_4$ flakes measured based on this speed of sound, which is somewhat slower than the value extracted from a linear chain model by Bartram et al.[214] Furthermore, we extend the technique to identify additional pulses in the time trace that we attribute to a stacking fault in the vdW crystal, a type of defect that is otherwise difficult to detect. Specifically, phase shifts in the phonon wavepackets can indicate discontinuities in the acoustic medium through which the wavepacket travels. In layered vdW materials, these discontinuities can arise from stacking faults that result in partial reflections of the strain pulse at the fault[216]. These reflections carry a 180^o phase shift from those that are only reflected off the substrate once.

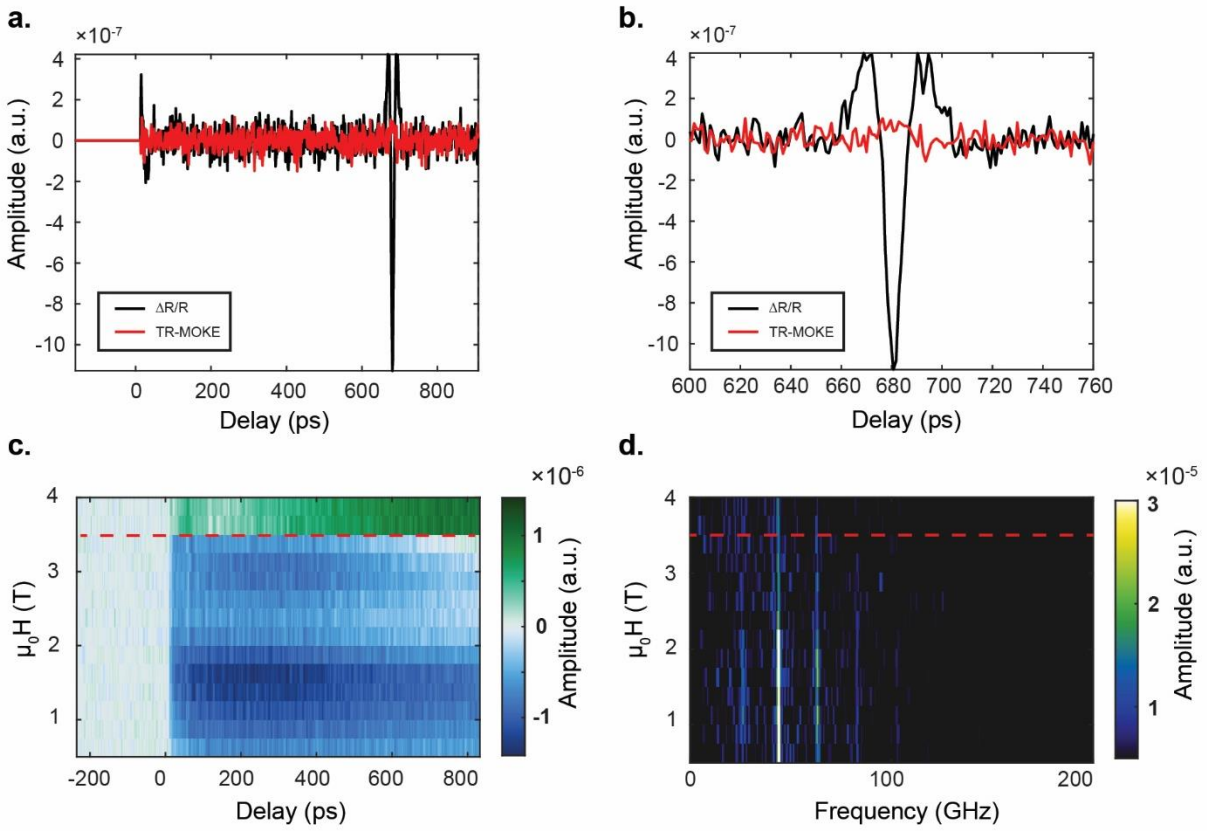

Figure 3.4: Absence of magnetostrictive coupling between cavity modes and magnetic order. (a) Time trace of transient reflectivity (black) and TR-MOKE (red) with exponential decay removed to highlight a picosecond pulse at 680 ps. **(b)** Expanded view of pulse in (a) demonstrating a negligible change in TR-MOKE concomitant with a significant change in reflectivity due to the strain pulse returning to the top surface of the crystal. **(c)** Dependence of the TR-MOKE on an external magnetic field applied along the crystal c-axis. The white dashed line emphasizes the metamagnetic transition at 3.5T that is easily identifiable from the change in sign of the MOKE signal. **(d)** FFT of the transient reflectivity as a function of magnetic field, collected simultaneously with the data in (c), showing that the comb spectrum remains unchanged across the metamagnetic transition.

This effect can be seen by contrasting data from two flakes of $MnBi_2Te_4$, shown in Figure

3.2a and Figure 3.2b. The data in Figure 3.2a show a single series of phonon reflections with a travel time of 144 ps (176 nm crystal thickness). In contrast, the data in Figure 3.2b shows a similar series of phonon reflections with a travel time of 150 ps (184 nm thickness) and a second series of reflections with opposite sign and a travel time of 240 ps. Based on the return times of the echoes, we infer that there is a stacking fault in this crystal 42 nm below the top surface. This stacking fault acts as a phonon beamsplitter, reflecting a portion of the incident acoustic wave each time it passes the fault. Figure 3.2c schematically presents this process, showing how the pump pulse generates the wavepacket that propagates, reflects from the back surface, and is then split at the discontinuity. In reality, the stacking fault reflects strain wavepackets incident on the fault from both directions. However, in our data, we do not observe reflections in the "upward" direction, either because the defect is close to the surface and reflections cannot be distinguished from the primary echo signal or because the defect reflects strain pulses asymmetrically. Consequently, we have chosen to omit a reflection from the discontinuity in the forward direction of our schematic to match our data.

The additional pulses that we observe have a period roughly 100 ps longer than the main pulse train, which could also arise from a secondary mechanism in which $MnBi_2Te_4$ transduces the strain pulse to the SiO_2 substrate and then is re-excited by the returning pulse, as was observed by Bartram et al.[214] We rule out this explanation on the following grounds: First, we would expect to see this kind of transduction in all of our samples exfoliated onto SiO_2, while we observe it in only a single sample. Second, the PU technique is expected to be sensitive to subsurface discontinuities in the acoustic impedance[207–209]. Third, our data are consistent with reflections from a "phononic beamsplitter" that most strongly reflects pulses toward the bottom surface of the crystal. Lastly, it is worth noting that because the acoustic impedance of SiO_2 (Z_{SiO2} = 12.55 MRayls[217]) is smaller

than that of $MnBi_2Te_4$ (Z_{MBT} = 23.9 MRayls[214]) and silicon (Z_{Si} = 19.7[217]), the phase difference between the two pulse sequences, which are longitudinal waves, is expected in both cases and thus does not favor one explanation or the other (see Figure 3.5). Unidirectional acoustic beamsplitters are expected to involve crystal defects, however, and would have interesting practical applications[214,218] that encourage further study of this behavior in $MnBi_2Te_4$.

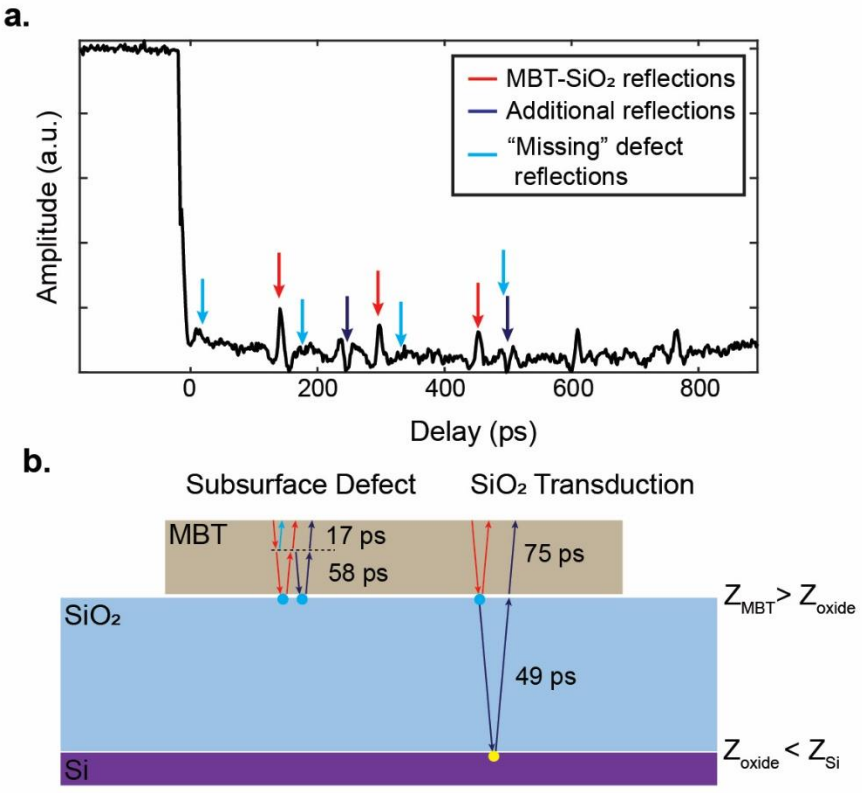

Figure 3.5: Depiction of two explanations for additional pulse reflections. (a) Same time-trace data as in **Figure *3.2***b with origin (or absence) of strain pulses highlighted in different colors. Red arrows denote the main PU pulse that reflects off the SiO_2-$MnBi_2Te_4$ interface. Dark blue arrows denote the additional phase-flipped reflections that we attribute to a subsurface defect, and light blue arrows mark where additional pulses should appear if the subsurface defect back-reflected the top-down incident strain pulse. **(b)** Cartoon depicting two possible origins for the additional

reflected signal. On the left, a subsurface defect that acts as a nearly unidirectional beamsplitter is depicted, with arrow color corresponding to panel (a). On the right, the possibility of transduction of the strain pulse through the SiO_2 substrate is shown, again with arrow color corresponding to panel (a). Reflections at interfaces that induce a 180^o phase flip are shown with blue dots, while reflections at interfaces that induce no phase flip are shown with a yellow dot.

In addition to measuring structural properties, a fascinating potential application of PU is to investigate materials physics that will exploit its acoustic nature to study the coupling of physical phenomena to those structural properties. As one example, magnetostriction describes changes in the parameters of a given crystal lattice under different magnetic states, which provides an avenue to employ PU to study magnetic effects. Figure 3.4a and Figure 3.4b compare the transient reflectivity signal with a simultaneously collected time-resolved magneto-optical Kerr effect (TR-MOKE) signal. TR-MOKE measures the transient rotation of linearly polarized light reflected from a sample due to pump-induced magnetization. As the phonon echo reaches the surface in Figure 3.4b, where we have zoomed in on the phonon echo presented in Figure 3.4a, we see a drastic change in the transient reflectivity signal. However, no appreciable change in the TR-MOKE signal over the course of the echo is present. Given that the primary strain generated by this method is in the out-of-plane direction, these data indicate that the moderate changes to the interlayer lattice parameters generated by the strain pulse do not induce changes to the magnetic ordering in $MnBi_2Te_4$. Quantifying the change in lattice spacing from the exact strain magnitude via PU is a nontrivial task that requires understanding of electronic and thermal diffusion that is beyond the scope of this work. Sufficiently large strains are expected to alter the interlayer magnetic coupling in $MnBi_2Te_4$.

Further, we find that the change of the magnetic state does not cause appreciable changes to the lattice parameters either. Figure 3.4c presents TR-MOKE data as a function of magnetic field applied along the out-of-plane *c*-axis of the crystal. There is a clear magnetic transition at $\mu_0 H \approx 3.5\,T$, highlighted with a white dashed line, which has previously been identified as a metamagnetic transition[146]. Figure 3.4d presents the spectrum of the acoustic phonons present in transient optical reflectivity measurements performed simultaneously with the TR-MOKE presented in Figure 3.4c. The spectra show no drastic change at the critical field that correlates to the transition seen in the TR-MOKE data, indicating no significant change to the structural properties of the crystal under different magnetic configurations. The decrease in amplitude with increasing field, particularly of the higher frequency modes, is a consequence of the continual decrease in overall transient reflectivity signal but does not exhibit a sharp change in behavior at the metamagnetic transition. Simply put, $MnBi_2Te_4$ presents no evidence of coupling between these cavity phonons and the magnetic order.

The above finding is consistent with a previous report that used similar measurements to investigate the interlayer breathing mode phonons intrinsic to the $MnBi_2Te_4$ crystal[214]. However, it is important to note that in the data we have presented here, the phonon modes are *cavity* modes of the system defined by the thickness of the crystal. In our case, many of these standing cavity modes coherently add to produce a propagating wavepacket. In the case of thinner crystals[214], these modes are not supported and a reduction in crystal symmetry allows the measurement of the out-of-plane breathing mode. In contrast to these findings, a recent study[219] found that $MnBi_2Te_4$'s A_{1g} modes, which are present in thicknesses down to monolayer, do couple strongly to the magnetic order. This implies that magnetostriction in $MnBi_2Te_4$ is sensitive to the specific vibrational mode and its associated symmetry. However, the sensitivity of PU to crystal strain and the advantages

derived from its all-optical nature (compatibility with cryogenic measurements, ease of integration with applied magnetic fields, etc.) establishes the PU technique as a probe that can measure out-of-plane magnetostrictive effects, an important capability for the growing field of 2D magnets which often present out-of-plane magnetic ordering.

The application of PU to thin vdW materials is still in its nascent stage, yet it holds the power to measure structural properties of the sample as well as phenomena that couple to the lattice. Exchanging information or energy between lattice, optical, magnetic, and charge degrees of freedom is both scientifically interesting and technologically relevant for applications in energy efficient information processing and quantum technologies. 2D materials represent an ever-growing platform in which to explore such coupling. The results presented here highlight that PU can be deployed on cleavable topological quantum materials and point to the power of PU for measuring the magnetic properties of thin vdW materials. The presence of multiple pulse trains in the data allows for the identification of stacking faults in the crystal. The lack of correlation between PU and magneto-optical measurements shows that there is no magnetostriction effect when considering cavity phonon modes. Finally, given the sharp peaks present in the frequency combs and their strong dependence on the acoustic properties of the host crystal, this technique should enable high resolution measurements of material properties that couple to the lattice. We hope that our work will motivate further application of this technique to vdW materials, both as a metrology tool for crystal quality and as a powerful technique for measuring the physical properties intimately connected to lattice parameters.

Methods

Crystal growth and sample preparation: $MnBi_2Te_4$ bulk crystals were grown out of a Bi-Te flux as previously reported[147]. All samples were prepared inside an Argon-filled glovebox. We isolate

thin flakes using standard scotch-tape exfoliation technique. For these measurements, we use two different substrates. Data shown in Figure 3.4a and Figure 3.4b were obtained from a bulk flake cleaved onto Scotch tape but never exfoliated onto a substrate. All other data were obtained from flakes exfoliated onto 285 nm thick SiO_2/Si wafers coated with ~ 2 nm of Cr or Ti followed by ~ 3nm of Au. We observe no qualitative difference in the PU behavior across different substrates. Optical and atomic force microscope images of few-layered flakes were taken inside the glovebox before sealing flakes in a copper spacer and transferring them to a cold-finger 4 K cryostat for measurement.

Optical Measurements: Transient optical reflectivity measurements were performed by using the output of a titanium sapphire amplifier tuned to 800 nm with a repetition rate of 100 kHz. The output was separated into pump and probe arms by a beamsplitter, and the pump light was passed through a sapphire crystal to generate broadband white light, which was subsequently filtered to a bandwidth from 490-530 nm. The probe beam was sent to a retroreflector mounted on a motorized translation stage to produce the pump-probe delay. Each beam was sent through a waveplate and polarizer to simultaneously attenuate the beams and set their polarization to a known orientation. The beams were then recombined and sent through a 0.6 NA microscope objective onto the sample. The pump and probe pulses carry ~1.5 mJ/cm^2 at the sample. The back-reflected probe beam was sent through a Wollaston prism to separate components of the beam that were parallel or perpendicular to the input polarization. The two components were directed onto the sensors of a balanced photodiode with a lock-in amplifier demodulating the signal at the frequency of a mechanical chopper placed in the pump arm of the experiment. The sum of the components produces the transient optical reflectivity measurements, while their difference produces the TR-MOKE measurements. To produce the time domain data, the delay stage was continuously swept

at low speed while streaming data from the lock-in amplifier to the host computer at a high sampling rate (> 100 kHz), which produced time traces with ~2 picosecond resolution in the data presented here. Multiple traces (25 < N < 100) were recorded and averaged, depending on the desired signal-to-noise ratio. The samples were kept at ~10 K, far below the Neel temperature of ~25 K in thin bulk samples[146], in an optical cryostat with an integrated out-of-plane magnet capable of applying fields up to 4 T.

Comb Characterization: Of the tens of samples of various thicknesses measured, we have presented data for the thinnest sample in which we observed clear pulses comprised of a discernible frequency comb. In thinner flakes (~10-20 layers, or ~15-30 nm), individual coherent interlayer phonon modes can be observed as oscillations in the reflectivity with a frequency of ~ 50 GHz; however, no pulsing is observed by previous work[220]. This coherent interlayer mode is a cavity mode, but several distinct modes must be supported before a frequency comb emerges. A true PU frequency comb can be used to study atomically thin samples, but it requires sandwiching these target layers between bulk crystals and using transducer layers to create an acoustic cavity that supports enough modes for pulse formation[213] . Below we include a basic cavity calculation that indicates that a minimum flake thickness of ~ 62 nm is required to see the 8-tooth frequency combs such as the ones that we have observed:

$$N\lambda = 2L$$

$$f\lambda = v$$

$$v = 2.45 \text{ nm/ps}$$

$$\lambda = \frac{v}{f} = 123 \text{ nm (20 GHz)}$$

$$\lambda = \frac{v}{f} = 37.7 \text{ nm (65 GHz)}$$

So, to see down to the 20 GHz mode, a cavity of length L = $\lambda/2$ = 61.5 nm is required.

Calculation of the Speed of Sound: We include a report of the speed of sound in our supplementary information based on the AFM data available to us because (1) it falls out naturally from doing these measurements, and (2) it provides a self-consistent way for us to determine flake thicknesses and defect depth. We have averaged two measurements together based on available AFM data (Figure 3.6); however, there is a ~15% discrepancy between these values. It is well known that $MnBi_2Te_4$ is laden with defects and that replicating device physics can take tens of samples. This suggests that there is significant variation in crystal quality (either from growth or material preparation) even within batches, and we believe that this variation could explain a 15% difference in measured speed of sound. Specifically plausible mechanisms for this variation include antisite

defects or vacancies that modulate interlayer coupling, which can have a dramatic effect on the out-of-plane speed of sound in vdW materials[203].

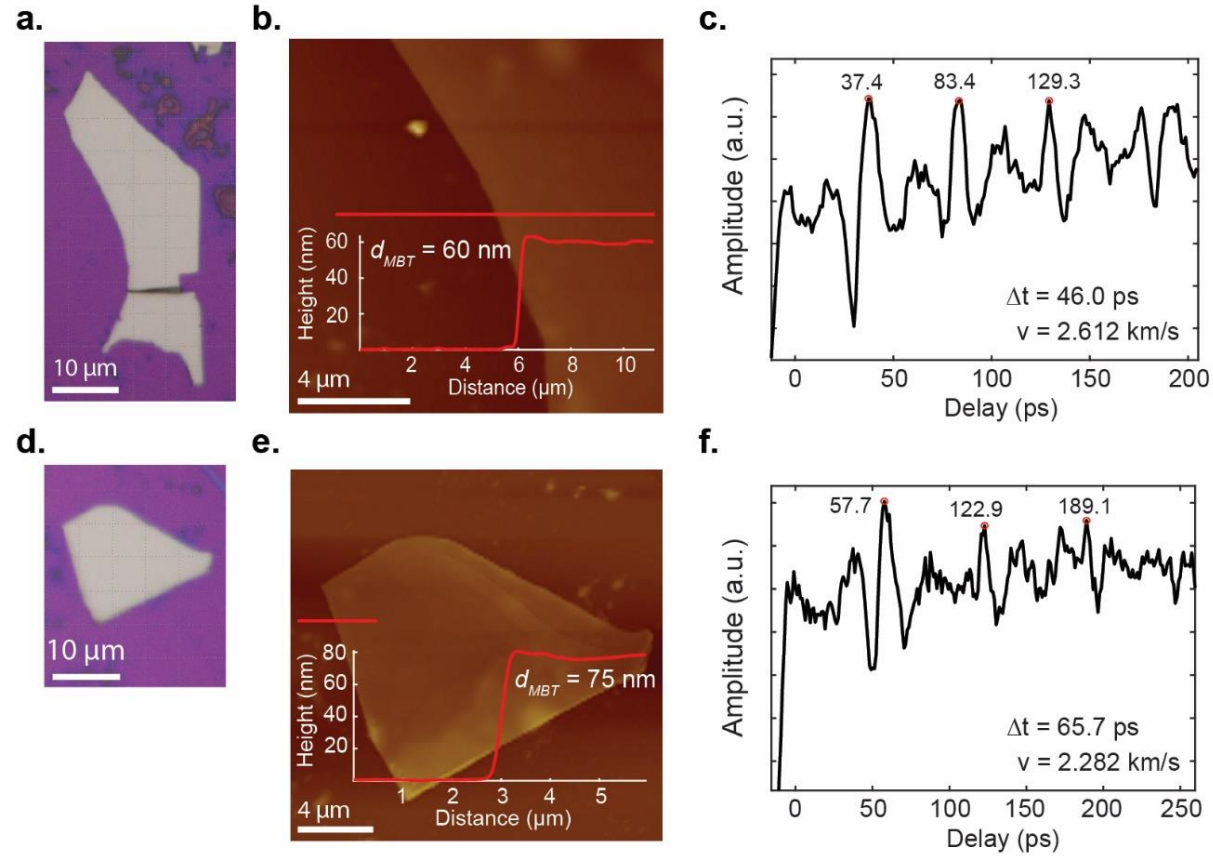

Figure 3.6: Determination of the speed of sound in $MnBi_2Te_4$ from Picosecond Ultrasonics. **(a, d)** Optical photographs of two $MnBi_2Te_4$ flakes used to determine the speed of sound. **(b, e)** AFM tapping mode topography of flakes measured. Inset: line cut taken at horizontal red lines in AFM image showing flake thickness. **(c, f)** Time-traces of optical reflectivity showing periodic pulses. Delay times corresponding to three phonon pulses are highlighted, with text insets showing average time delay between pulses and corresponding speed of sound $v_s = 2d_{MBT}/\Delta t$.

Chapter 4 | Strain Tunable Moiré Geometry and Geometric Phase Analysis

This chapter consists of my as-yet unpublished work: **Jordan Fonseca**, John Cenker, Yuzhou Zhao, Ying Xia, Shuai Zhang, Juan Carlos Idrobo, Xiaodong Xu, "Strain-tunable moiré geometry revealed by piezoresponse force microscopy and geometric phase analysis," *in preparation* (2024). X.X. conceived of the experiment. J.F. prepared samples, assisted by J.C. J.F. performed PFM measurements, assisted by J.C., Y.Z., Y.X., and S.Z. J.F. performed the data analysis and wrote the GPA analysis script, with input from J.C., Y.Z., and J.-C.I. J.F. wrote the paper, with input from all authors. All authors discussed the results.

Introduction:

There are many compelling reasons that 2D materials have attracted the interest of theoretical and experimental physicists, materials science researchers, and engineers. Perhaps chief among these reasons is the unique platform of a 2D moiré superlattice. Because there is a 2D material that offers nearly every imaginable material property (metals, insulators, semiconductors, semimetals, magnetic materials, superconductors), it is possible to create heterostructure devices consisting of layered structures of different materials. When two different crystal lattices that differ slightly, either from a mismatch in atomic spacing or a relative rotation between crystal axes, are overlapped, a moiré superlattice forms with a moiré wavelength governed by Equation 4.1[221]. When the two crystal lattices are different materials, an average lattice constant and lattice mismatch can be computed using Equation 4.2 and Equation 4.3, respectively. Hence, the moiré wavelength introduces a new length scale and corresponding potential landscape to the system, and this length scale and energy landscape can have profound impact on the behavior of electrons, phonons, and excitons in the system[21,57,222–232].

There are a number of models of electronic interactions in two dimensions that explain a surprising variety of electronic behavior. Simplest among these models is the Hubbard model, which accounts for intersite hopping t and an onsite potential U. This simple model can be extended to include repulsion V between particles on neighboring sites[57]. Since the hopping parameter depends strongly on the distance between adjacent lattice (or moiré superlattice) sites, hopping can be controlled by adjusting twist angle between flakes, making moiré superlattices a platform in which the ratio t/U can be widely tuned. Because the hopping energy, or kinetic energy can be quenched relative to the onsite interaction, it is possible to engineer moiré superlattices in which Coulomb interactions between electrons are the dominant energy scales, giving rise to correlated electronic phenomena[38,40,41,43–49,51,52,56,233,234].

$$\lambda_m = \frac{(1+\delta)a}{\sqrt{2(1+\delta)(1-\cos\phi)+\delta^2}} \tag{4.1}$$

$$a = \frac{a_1+a_2}{2} \tag{4.2}$$

$$\delta = \frac{|a_1-a_2|}{a} \tag{4.3}$$

For as long as researchers have been fabricating moiré heterostructures to study the behavior of electrons, excitons, and other quasiparticles that respond to the moiré potential, the important role of inhomogeneity, strain, and disorder have been apparent[111,235–238]. During fabrication, 2D flakes are subject to forces that induce strain and rotation. Bubbles and contaminants can be trapped between or underneath layers[239–242], and thermal and strain gradients occur naturally in the course of typical flake transfer and fabrication processing steps. This issue can be turned on its head, however, to ask how homogenous and inhomogeneous strains can be used to alter the moiré geometry and thereby control the electronic and optical properties.

Long before the discovery of vdW materials, strain was recognized as an important control parameter for tuning important material properties such as superconductivity[243–246]. Shortly after

the isolation of monolayer graphene, it was discovered that 2D materials not only offer an unparalleled flexibility compared to bulk crystals, but also an unparalleled strength. Graphene is often heralded as being "stronger than steel," a phrase that refers to a number of properties, including a Young's modulus over 1 TPa[247]. Mechanical measurements of MoS_2 reported monolayer flakes sustaining strains up to 11% before yielding at stresses of 11% of the Young's modulus[77], a value approaching the theoretical 2D yield strength of 1/8 the Young's modulus[78]. In the past 20 years, there have been a vast number of experimental and theoretical works exploring how uniaxial, biaxial, and shear strains alter the electronic, vibrational, and optical properties of a wide variety of 2D materials, particularly graphene and TMDs (see **Table 1** in Appendix D for a compiled list of over 100 papers based on what material system, strain approach, and maximum strain each approach achieved). Because a moiré superlattice consists of two loosely adhered layers of crystal, studies of strain in moiré systems must consider a wider variety of factors, such as how well strain transfers from one layer to the next, how relative twist angle or edges change interlayer friction, how strain transfer differs when the two flakes are the same crystal (e.g. graphene on graphene) versus when the two flakes are different (e.g. WSe_2 on WS_2)[84,135,248–254].

There are many different approaches to visualizing and measuring strain in 2D crystals and their moiré heterostructures. Common optical techniques include Raman spectroscopy[107,113,125,255] and optical SHG[24,25], although PL and reflectance can be used as well since strain strongly tunes the bandgap of atomically thin TMDs. These techniques, which are typically implemented via microscopy, have the intrinsic spatial resolution of a diffraction-limited beam spot (~1-5 μm^2) and must be rastered across the sample to provide a spatial map. Near-field optical techniques such as nano-SHG and techniques that probe atomic structure such as HRTEM and STM provide atomic resolution and thereby are an excellent way to resolve strain in each layer as well the resulting

moiré; however, both techniques require expensive, specialized equipment and careful sample preparation to be compatible with either approach. Lastly, atomic force microscopy (AFM) and related scanning probe techniques (Kelvin probe force microscopy—KPFM, conductive AFM, PFM, torsional force microscopy, etc.) offer a cost-effective way to directly image moiré superlattices with the potential for atomic resolution[256–261]. During 2D device fabrication, PFM has become the dominant technique for imaging the moiré superlattice before completing the device with a top layer.

In parallel with the AFM techniques that provide an image of the moiré superlattice, there remains a question of how to interpret these data quantitatively and qualitatively. While a sense of "homogeneity" can be seen by eye and an average moiré wavelength can be measured from an FFT (e.g. **Figure 4.3**a,d, **Figure 4.4**a), to truly create a spatially resolved measure of local moiré wavelength (and thereby underlying relative twist angle and strain), additional analysis is required. There have been a handful of research works that tackle this task of quantitatively extracting spatially resolved strain and rotation[238,262,263].

In this chapter, we will explore how Geometric Phase Analysis (GPA), a technique developed for HRTEM and STM data, may still have a lot to offer for the analysis of AFM images of moiré superlattices that lack the resolution to resolve constituent lattices. While this technique is over 20 years old, it has only been implemented a handful of times on low-energy electron microscopy images of moiré superlattices[262,264]. While GPA is a technique rooted in the physics of a periodic image and its Fourier transform, it is agnostic to the source of these data, and is therefore well suited to be ported over as a tool for adding spatially resolved quantitative understanding to analysis of moiré images. Running GPA on typical data sets requires relatively low computational

power and can be done in reasonable time on an average personal computer, making it a natural addition to a data analysis pipeline.

Results

We begin our study of strain-tunable moiré geometry with one of the most straightforward samples possible: a monolayer flake of WSe_2 aligned to a thin bulk flake of WS_2, which are picked up and transferred onto a polyimide substrate, as shown in **Figure 4.1**b, c. This sample is secured to the PI substrate with Au clamps, which at the time of fabrication were believed to enhance strain transfer from the PI through the bulk of the WS_2. Since the preparation of this sample, subsequent measurements have indicated that using metal to clamp TMDs to the substrate is not a viable approach to improving overall strain transfer, although there is some reason to believe that clamps can introduce a strain-transfer-pinning effect that helps generate vertical strain gradients[265]. By clamping only the WS_2 and not the WSe_2, the chances of generating heterostrain between the TMD layers increase. While the moiré heterostructure would typically be encased in hBN to provide a uniform dielectric environment and the possibility of electrostatic gating for optics or transport measurements[266,267], we leave the moiré interface intentionally exposed to facilitate direct imaging of the moiré interface with an atomic force microscope. We employ the well-established technique of PFM to image the moiré[257] (**Figure 4.1**d), though we note that since then there has been a report that the AFM that we use (Bruker Dimension Icon) images the moiré because of crosstalk from torsional modes, not the inverse piezoelectric effect[256].

After device fabrication, we attach the sample to a strainer adapted for room-temperature measurement (**Figure 4.1**a). Because the maximum field limit for tensile and compressive strains of the piezo is symmetric at cryogenic temperatures, our cryogenic strainers are wired with the central piezo stack shorted backwards to the outer stacks (Figure 4.2a). This scheme has two main

advantages: first, the piezos are all *oriented* the same direction, so the natural thermal expansion during cryostat warmup and cooldown causes a sample displacement, minimizing the strain induced during sample cooling. Second, the piezos (which are much less efficient at cryogenic temperatures) can achieve maximum strain without displacing the sample by applying tensile strain to the outer stack and compressive strain to the inner stack. For room temperature measurement, only ~20V of compressive strain can be applied compared to the ~120V of tensile strain that is possible. With the cryogenic shorting scheme, our strain measurements would be limited to 20V. By disconnecting the central piezo and shorting it to itself (**Figure 4.2**b), we can apply 120V of tensile strain at room temperature at the cost of losing the symmetric gap opening that prevented sample displacement and provided a nominal factor of 2 increase in the maximum gap width. One consequence of this wiring scheme is that the sample will be displaced as the gap opens since the outer piezos are moving while the inner one remains fixed. To accommodate this, the AFM scan area must be manually adjusted at each strain value to track the same region of the sample. Lastly, it is worth noting that because all piezos have a "butterfly" hysteretic voltage-displacement curve (**Figure 4.2**c), it is important to perform comparable measurements *over the same strain/voltage range* and to always compare measurements that were *swept in the same direction.*

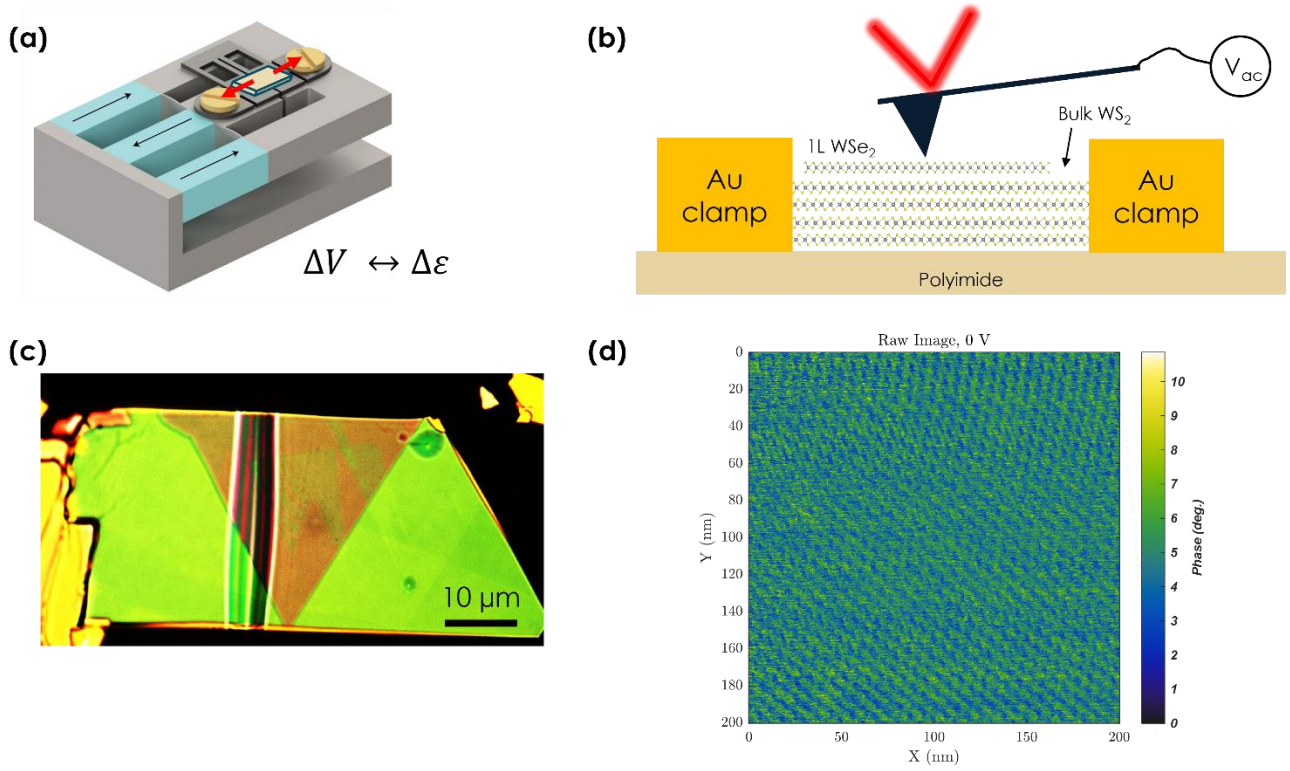

Figure 4.1: In-situ imaging a strain-tunable moiré superlattice with piezoresponse force microscopy. (a) Schematic of piezoelectric strain apparatus and PI substrate. **(b)** Schematic of sample consisting of monolayer WSe_2 aligned to bulk WS_2, which is clamped to PI using gold. The sample leaves the moiré interface exposed for PFM measurements. **(c)** Optical photo of the heterostructure before Au clamping. **(d)** PFM image of the WSe_2/WS_2 superlattice with no applied strain.

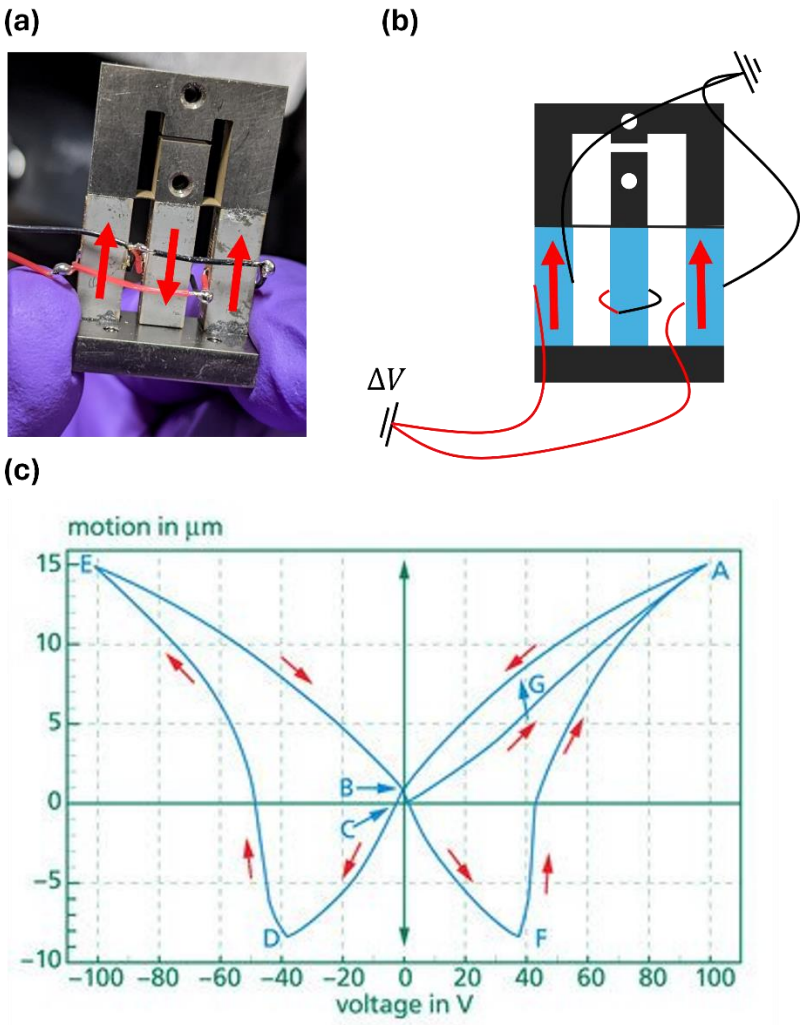

Figure 4.2: Temperature-dependent wiring scheme for piezoelectric strainer. (a) Wiring scheme of cryogenic use of the strain cell. **(b)** Schematic of wiring scheme for room temperature use of the strain cell. **(c)** Typical butterfly-hysteresis diagram for displacement vs. applied voltage/electric field. Reproduced from ref [268]. Red arrows show the direction of displacement/expansion when a positive voltage is applied in (a) and (b).

As the sample is stretched, the effects of strain are readily apparent in the PFM images. **Figure 4.3**a and **Figure 4.3**d show a representative example of data at two different strain values — 0V and 75V. While it is clear from the PFM image that the moiré pattern changes under strain,

it is difficult to quantify these changes in real space. To quantify these changes, we take the 2D FFT of each image and select the three most prominent distinct spatial frequencies (**Figure 4.3**b, e). For simplicity, we pick out only a single set of peaks and omit the set of peaks that are 180° out of phase since the information is redundant. Finally, we can take inverse FFT of these three main peaks, which represent the dominant/average moiré reciprocal lattice vectors. This process leaves a significantly filtered real space image of the moiré superlattice that captures the average moiré pattern present in the PFM data at each strain value (**Figure 4.3**c, f). While this technique elides the granular features within each image, it makes it possible to see by eye that the moiré lattice stretches (and possibly rotates) under uniaxial strain.

Having established a way to extract three dominant moiré reciprocal lattice vectors from each image, we can now explore the trends as we apply uniaxial tensile strain. **Figure 4.4**a clarifies how the three peaks in each PFM FFT can be converted to an amplitude and direction of a moiré lattice vector. For peak i with $i = 1, 2, 3$, the reciprocal space magnitude is $k^i_{mag} = \sqrt{k_x^2 + k_y^2}$. The real space periodicity λ^i_m is then the reciprocal of this value, $\lambda^i_m = 1/k^i_{mag}$, and the direction of the moiré lattice vector is $\theta^i = \tan^{-1}(k^i_y/k^i_x)$. **Figure 4.4**b shows the magnitude of each of the moiré lattice vectors versus strain, while **Figure 4.4**c shows the directions versus strain. It is worth noting that while the red and green dots represent the real moiré periodicities, the blue dots are a secondary, higher-order correction to the shape of the moiré geometry, which is why they appear to have a periodicity roughly half of the real moiré periodicity and why they are offset by only ~30° from the real moiré lattice vectors.

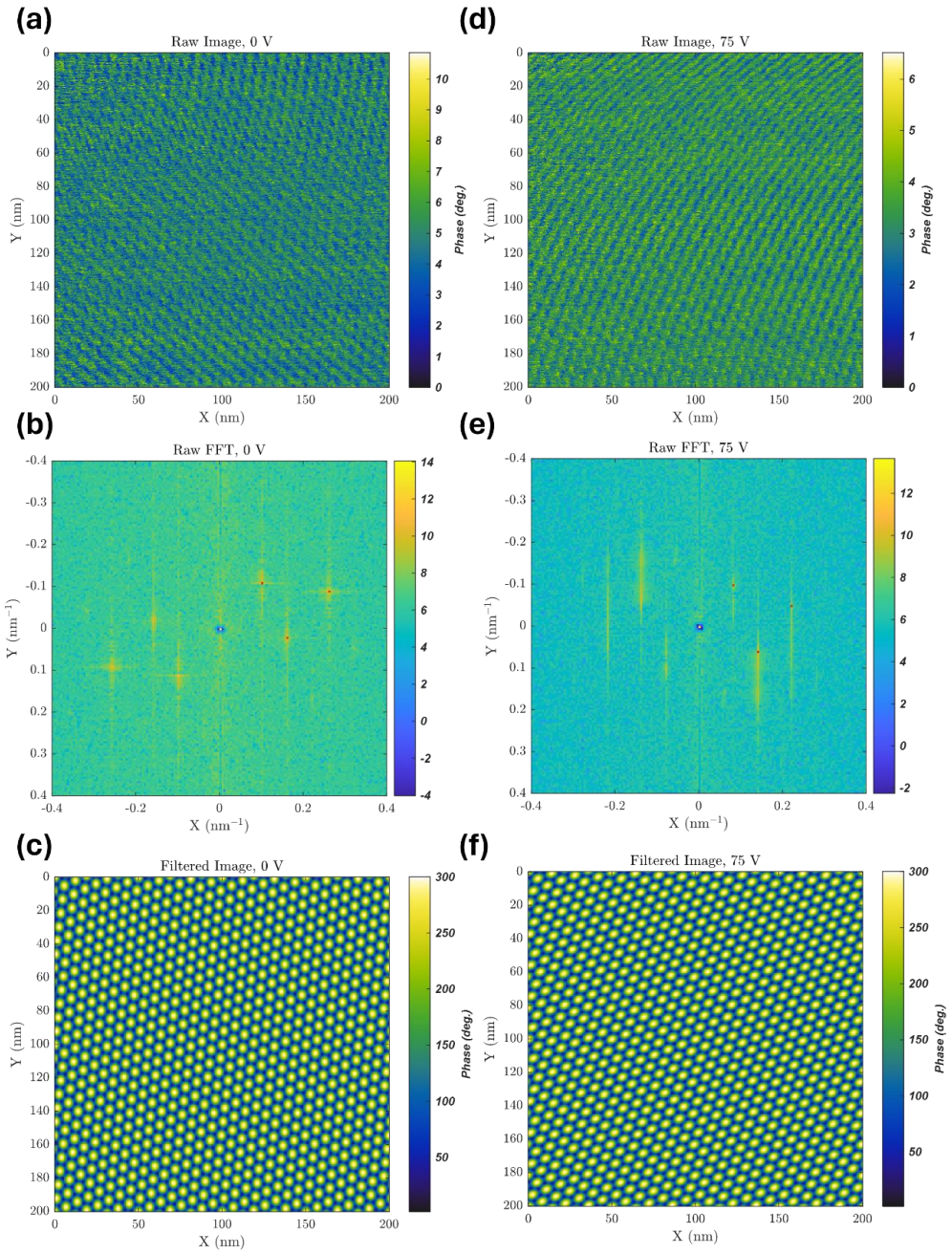

Figure 4.3: Strain-dependent PFM with FFT and filtered peaks showing how moiré patter stretches under applied strain. Strain-dependent PFM data at 0V **(a)** and 75V **(d)** applied to the piezoelectric strainer. PFM data with simple data processing (line scan alignment and quadratic background subtraction) are shown in the top row. **(b)** and **(e)** are FFTs of the data shown in (a)

and (d), respectively, and red pixels pick out the three most prominent peaks from the FFT. **(c)** and **(f)** show an inverse FFT of the three red peaks picked out in plots (b) and (e).

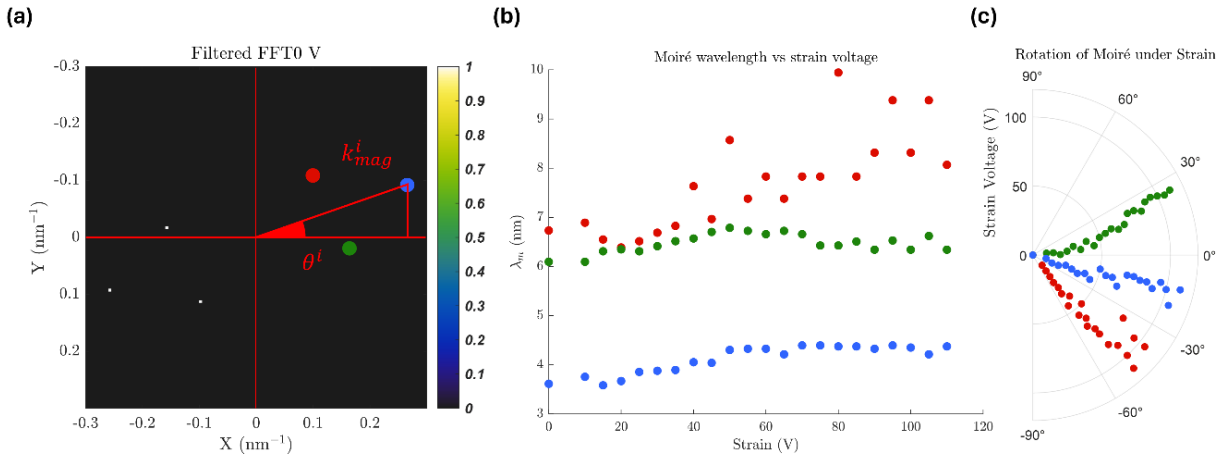

Figure 4.4: Expansion and rotation of the average moiré wavelength under uniaxial strain. **(a)** Example of how a moiré wavelength and peak angle can be extracted from the filtered FFT of each PFM image. Red and green dots are the lowest-wavelength moiré peaks corresponding to a real moiré wavelength, while the blue dot corresponds to a higher-order periodicity of the moiré wavelength resulting from the non-sinusoidal shape of the real moiré potential landscape. **(b)** Extracted moiré wavelength plotted for each strain value. **(c)** Extracted peak angle plotted for each strain value.

There are two main aspects of these data in particular that are worth highlighting. First, even though taking a handful of dominant peaks from the FFT is a crude approach, a clear trend emerges in the change in magnitude of the moiré lattice vectors. Up to ~60V, there is a clear upward trend in the magnitude of the vectors shown by blue and green dots in **Figure 4.4**b and little change in direction as shown by **Figure 4.4**c. Above 60V, the magnitude data become much noisier, not indicative of real fluctuations in the moiré periodicity but rather in the noisiness of the raw PFM data. Interestingly, though noisy there is also a sudden counterclockwise rotation of ~10^o

in all moiré lattice vectors. These data, taken together, suggest that after a certain point, the moiré may release strain energy by undergoing a rotational relaxation rather than a slipping or continued stretching, though further measurements or theoretical modeling would help corroborate this claim. The second clear take-away is that the moiré patterns measured here are not completely uniform, even across the 200×200 nm^2 measured area. Quantifying this inhomogeneity and understanding how strain is locally or globally transferred to the moiré superlattice is the focus of the remainder of this chapter.

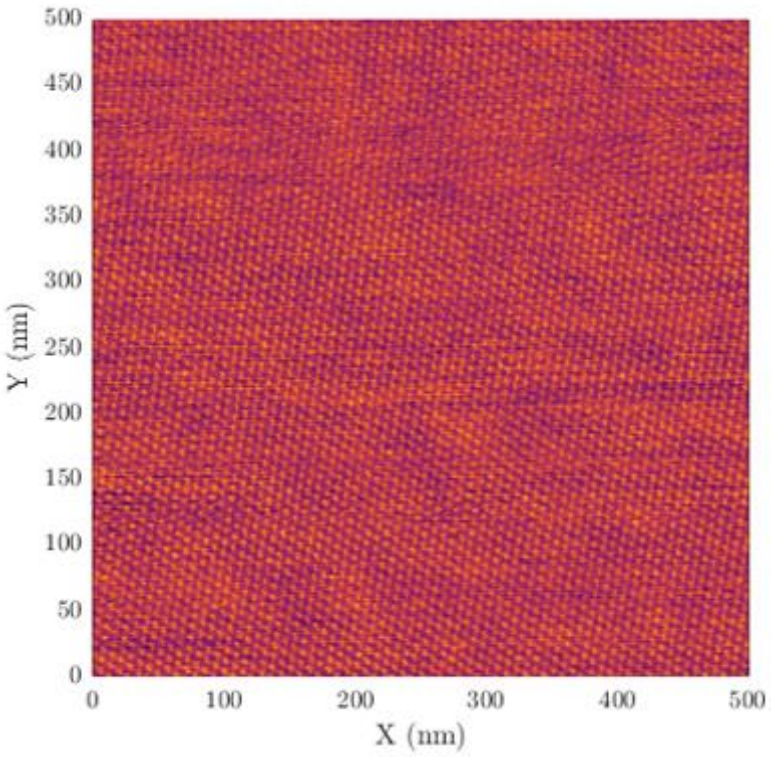

Figure 4.5: PFM image of a traditional, aligned WS_2/WSe_2 heterostructure from Heonjoon Park (UW)

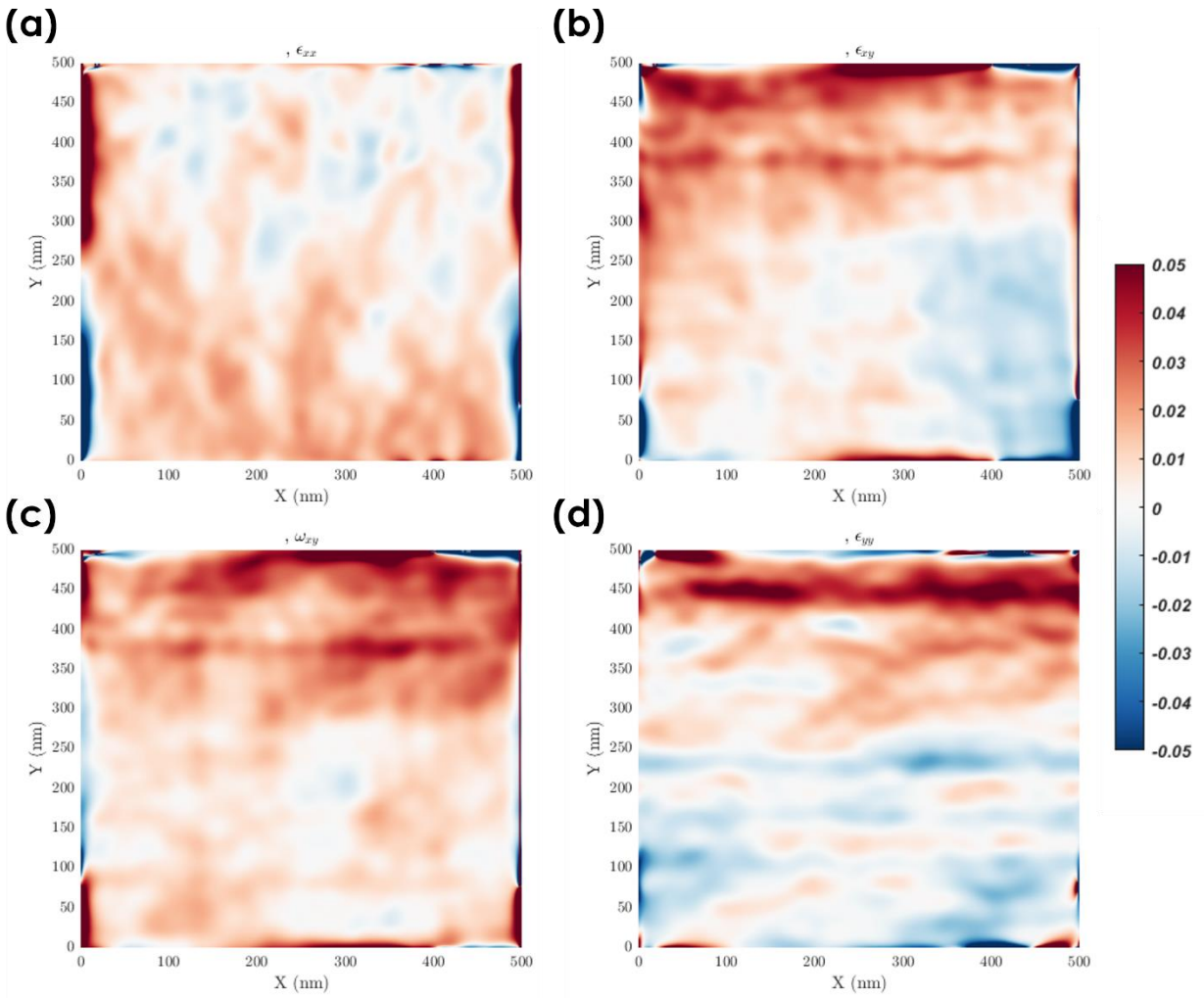

Figure 4.6: GPA-generated strain matrix on a PFM of a WS_2/WSe_2 heterostructure. GPA computed ϵ_{xx} **(a)**, symmetrized ϵ_{xy} **(b)**, anti-symmetrized ω_{xy} **(c)**, and ϵ_{yy} **(d)** revealing subtle inhomogeneities across the image in lattice strain and twist angle. All GPA images computed on the PFM image shown in **Figure 4.5**.

Geometric phase analysis is a technique that can be used to quantify strain in a periodic structure such as a crystal lattice. It has been used extensively in analyzing HRTEM and STM images of grain boundaries, local defects, and lattice strains[269,270]. The theory of GPA, including examples of how our home-built GPA algorithm can be used on a moiré superlattice, are included in Appendix B. We begin by showing the results of applying GPA to a PFM of a high-quality

WS_2/WSe_2 moiré superlattice fabricated on a typical hBN/graphite back gate on a Si/SiO_2 substrate (**Figure 4.5 and Figure 4.6**). The raw PFM data are shown in **Figure 4.5**, while the matrix elements ϵ_{xx}, ϵ_{xy}, ω_{xy}, and ϵ_{yy} are shown in **Figure 4.6**a-d, respectively. Note that in this case, the strain terms have been symmetrized while the rotation matrix ω_{xy} is antisymmetric. From these data, a few salient aspects stand out. First, by eye the PFM data look exceptionally uniform across the 500×500 nm^2 scanned area. This device, which was completed and studied optically (**Figure 4.7**) exhibited correlated electronic phenomena as indicated by clear, sharp changes in PL intensity and energy, suggesting that this is a high-quality and uniform moiré superlattice by the traditional standards of the field. Nevertheless, GPA reveals localized strains and rotations that can be quantified in a way that would not be possible from simple FFT analysis alone and may offer a way to rigorously quantify moiré homogeneity either as part of the general fabrication pipeline or as a quick, convenient, and inexpensive way to quantitatively analyze arbitrary moiré patterns.

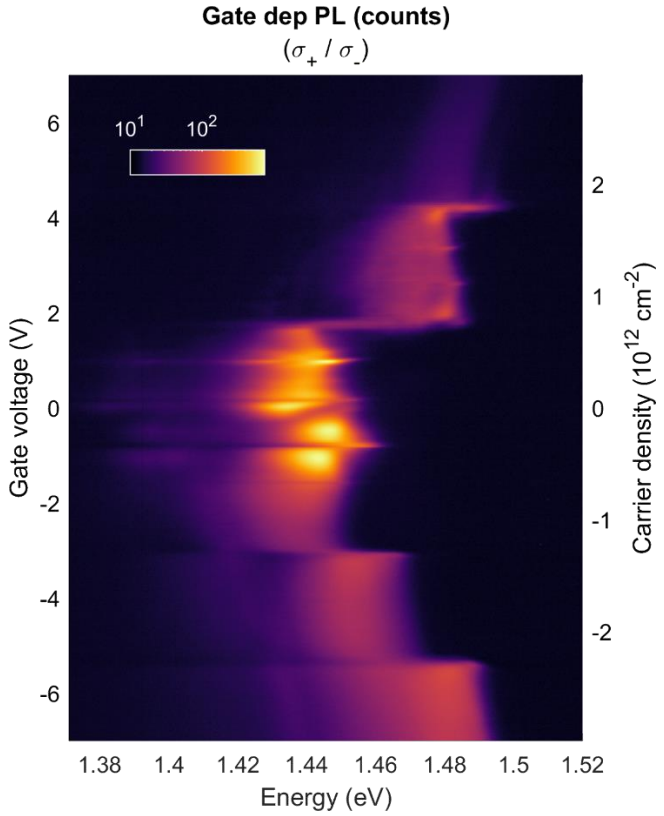

Figure 4.7: Doping-dependent photoluminescence from a dual-gated WS_2/WSe_2 device. The sharp jumps in PL intensity and energy as a function of gate voltage correspond to integer and fractional electron/hole fillings of the moiré superlattice. These data were collected from the moiré device whose moiré landscape was imaged with PFM and shown in **Figure 4.5**.

While the ability to resolve atomic positions and the moiré pattern simultaneously is typically an advantage, there are problematic artifacts that emerge when using GPA on lattices that form a moiré pattern. **Figure 4.8** demonstrates how what initially appears to be relaxation-induced strain in a system that is known to exhibit this phenomenon is actually a result of moiré-induced artifacts. **Figure 4.8**a shows a large, high-resolution HRTEM image of a WS_2/WSe_2 moiré superlattice shared by Juan Carlos Idrobo (UW). **Figure 4.8**d shows the corresponding GPA-calculated ϵ_{xx} for this image, in which a periodic, rhombohedral strain field that matches well with the high-symmetry points of the moiré emerges. Since lattice relaxation is a known phenomenon

in this material system, it at first appears that GPA has successfully revealed and quantified the strain profile within the moiré unit cell. However, GPA-calculations (**Figure 4.8**e, f) on *simulated,* perfect WS_2/WSe_2 moiré superlattices with a 1° twist angle that are not relaxed (**Figure 4.8**b, c) show a nearly identical pattern. The challenge arises because GPA is rooted in singling out a reciprocal lattice vector, building a mask around it in Fourier space, and then measuring how peaks within the vicinity of the masked area vary across the image. Moiré patterns introduce new, long-wavelength (small reciprocal lattice vector) periodicities that create not only new peaks in the FFT close to the origin, but also satellite peaks around the crystallographic reciprocal lattice vectors. If these moiré satellite peaks are within the applied mask, they result in the artifacts seen in **Figure 4.8**, which have also been studied elsewhere[271]. For this reason, there is precedent for using GPA on images in which *only* the moiré superlattice can be resolved and then performing the analysis on the *moiré reciprocal lattice vectors*.

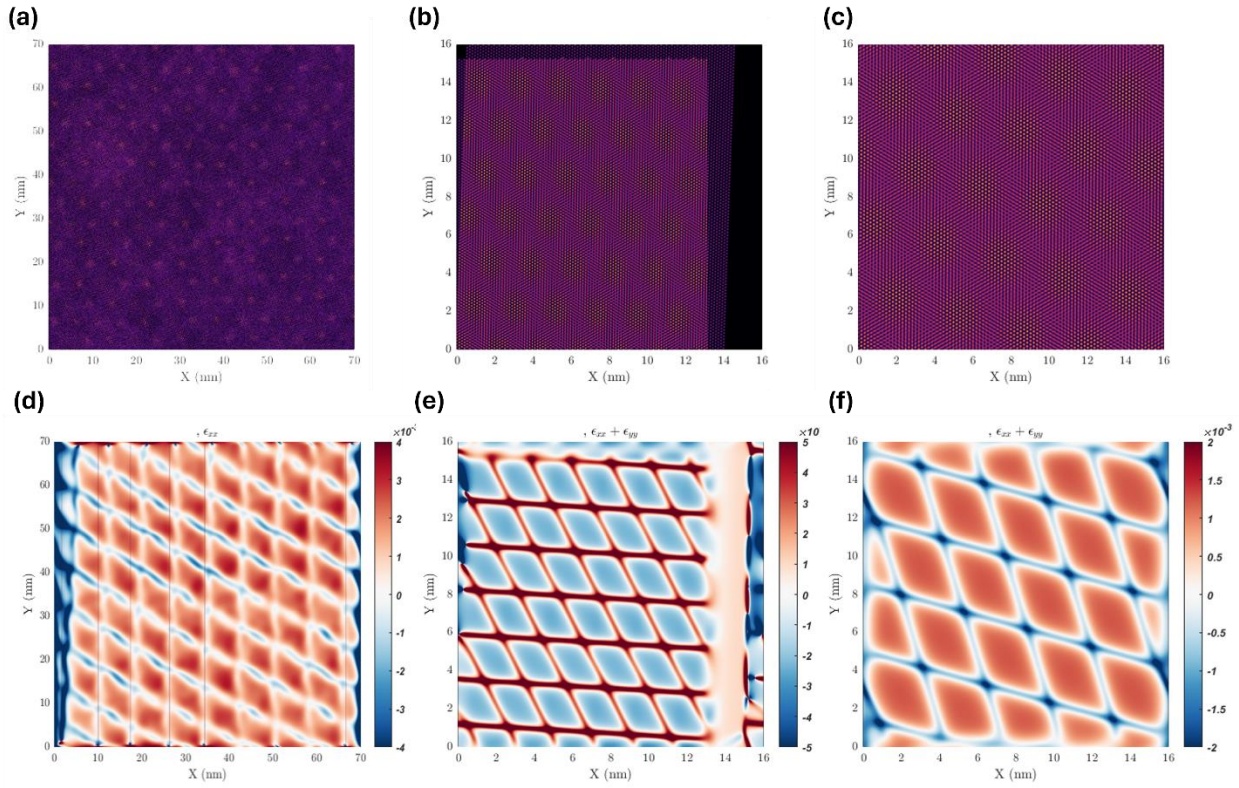

Figure 4.8: Artifacts in GPA analysis of moiré images with lattice resolution. (a) HRTEM image of a WS_2/WSe_2 moiré superlattice. Adapted from: "*Atomic-Scale Insights of Exciton-Moiré Coupling in WSe_2/WS_2 Superlattices*,**"** Elizaveta Tiukalova, Yuzhou Zhao, Xiao-Wei Zhang, Rohan Mewada, Andrew R. Lupini, Jihui Yang, Di Xiao, Ting Cao, Xiaodong Xu, and Juan Carlos Idrobo, *unpublished* (2024). **(b)** Simulated WS_2/WSe_2 moiré superlattice with a 1^o twist. **(c)** Different way to simulate a moiré lattice with a 1^o twist. (d) GPA-calculated ϵ_{xx} for the data in (a) showing emergence of what appears to be a strain field with a rhombohedral tiling. **(e, f)** GPA-calculated $\epsilon_{xx} + \epsilon_{yy}$ (biaxial strain) for the simulated moiré lattices in (b) and (c), respectively reveal that the rhombohedral strain field that emerges is an artifact since the simulated lattices include no relaxation that could give rise to a real lattice strain.

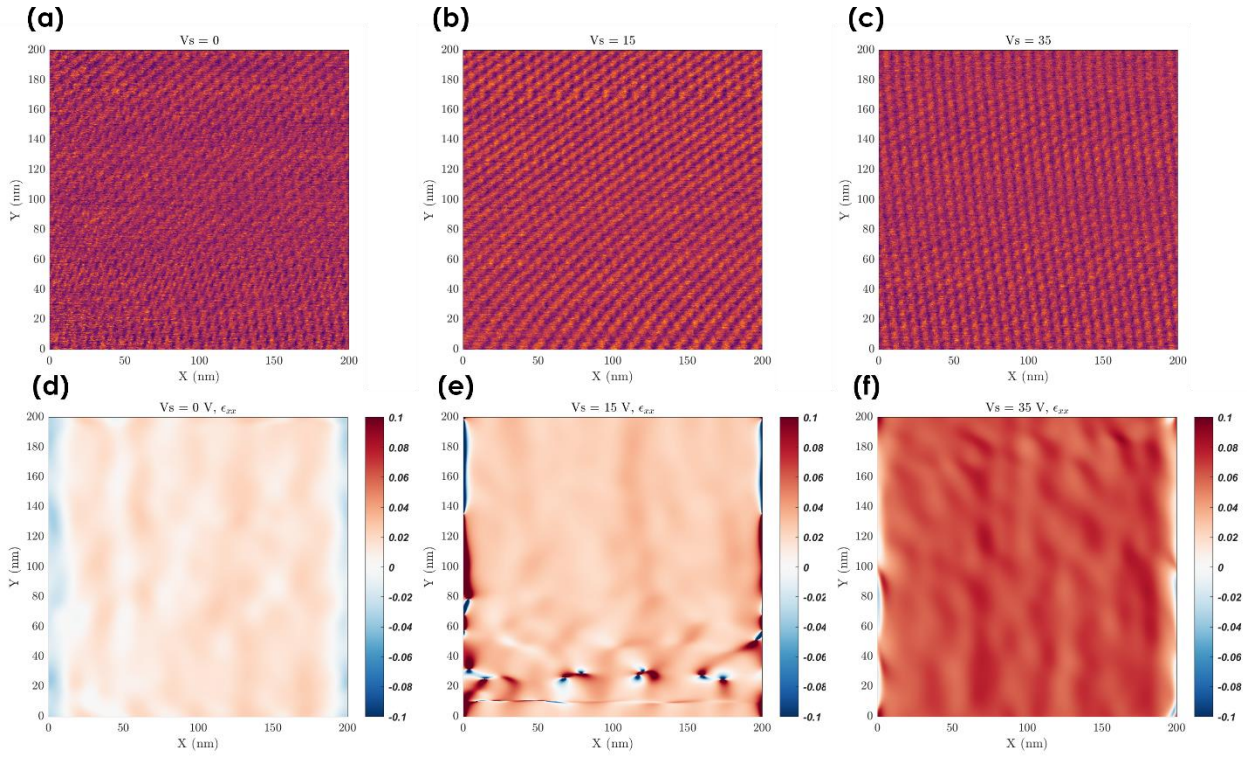

Figure 4.9: PFM images at 3 different strains and corresponding ϵ_{xx} maps. PFM data at 0V **(a)**, 15V **(b)**, and 35V **(c)** of applied strain. **(d-f)** GPA computed ϵ_{xx} maps at each strain value.

Having established the validity of applying GPA on a moiré superlattice, we can now use it as a tool to understand the localized strain transfer to the WS_2/WSe_2 moiré interface as we increase strain. **Figure 4.9**a-c shows PFM images at 0V, 15V, and 35V of applied strain, while **Figure 4.9**d-f plots the ϵ_{xx} component of the strain tensor at each applied strain voltage. GPA requires the use of "reference" reciprocal lattice vectors, and for the strain-dependent GPA, the dominant lattice peaks at 0V applied strain are used as a reference, so all subsequent strain maps are relative to the "unstrained" PFM image. Despite using the 0V image as a reference, inhomogeneous variation in ϵ_{xx} can still be observed as variation in color within the image (**Figure 4.9**d). **Figure 4.9**d-f show a clear trend of increasing overall longitudinal strain across the entire image; however, they also revel the gentle variation within each image that demonstrates

inhomogeneous strain transfer on a length scale on the order of 2-3 times the moiré unit cell. The singularities observed in **Figure 4.9**e toward the bottom of the image are artifacts where the distortion measured by the AFM (most likely due to a line scan artifact) are too great to be accurately captured by GPA, which is specifically sensitive to very small deviations in the reciprocal lattice vector and cannot be expected to capture all forms of variation that can introduce larger aperiodicities to the image[269,270,272]. PFM images and GPA-calculated ϵ_{xx} and ϵ_{yy} maps for all strain values 0V – 40V can be found in Appendix C, **Figure C.1** and **Figure C.2**

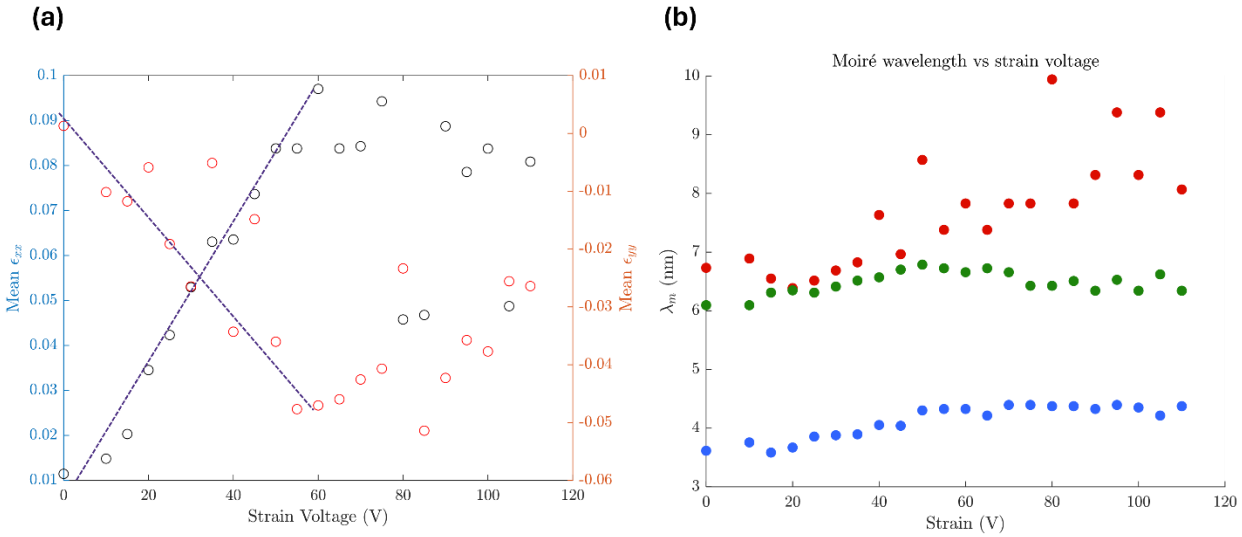

Figure 4.10: Comparison of average GPA-calculated uniaxial and Poisson strain with FFT-calculated strain analysis. (a) Mean ϵ_{xx} (black dots) and ϵ_{yy} (red dots) versus applied strain voltage. Dotted purple lines serve as a guide to the eye. **(b)** Magnitude of the moiré lattice vectors from **Figure 4.4**b replotted.

Having used GPA to quantify a percentage change in the moiré periodicity parallel to and perpendicular to the applied stress and to visualize the localized inhomogeneity in this strain, we can also compare these results to our original FFT analysis. We begin by extracting the average

uniaxial strain ϵ_{xx} and Poisson strain $\epsilon_{yy} = -\nu\epsilon_{xx}$ at each strain value and plotting them against applied strain voltage (**Figure 4.10**a). From 0V to 60V, the mean ϵ_{xx} increases by 10% while the mean ϵ_{yy} is reduced by ~ 5%. The increase in longitudinal periodicity of 10% matches well with the FFT analysis, which shows a comparable increase over the same voltage range (**Figure 4.10**b, replotted for convenience). Furthermore, because GPA produces a strain matrix with axes aligned with the applied strain, we see that the trend in increasing average ϵ_{xx} is even clearer than the corresponding increase in moiré lattice vector magnitude. This can be explained because the Poisson shrinking requires a compression transverse to the strain, but since the FFT peaks do not lie purely along Cartesian axes, their change in position is not exactly representative of the sample strain since only biaxial strain would cause *all* moiré periodicities to increase.

It is worth noting that while 10% uniaxial strain is within the plausible limit for a 2D material, it is more likely that there is a heterostrain effect that causes the WS_2 crystal to be strained more than the WSe_2 monolayer on top and that a 10% change in *moiré wavelength* actually represents a combination of homostrain and heterostrain. In the limit of pure heterostrain on a 1^o twisted WS_2/WSe_2 heterostructure a lattice strain of less than 0.5% produces an increase in moiré wavelength of 10% (calculated based on equations 4.1, 4.2, and 4.3).

In conclusion, this chapter outlines how the technique of geometric phase analysis has been ported over from the fields of electron and scanning probe microscopy and employed on comparatively low-resolution AFM images of moiré superlattices as a new metrology tool for an accessible measurement technique on a particularly widely studied material system. In this chapter, I have demonstrated how from this analysis, moiré wavelength variation across the AFM scan window can be quantified and spatially resolved. Additionally, I have shown how the strain-induced change in moiré wavelength can be characterized as uniaxial strain is applied *in-situ* to a

WS_2/WSe_2 moiré heterostructure. Some of the known artifacts[271] of employing GPA on the underlying crystal lattice vectors when a moiré pattern is present are also explored. As far as this author is aware, this is the first instance in which this technique has been used to extrapolate and quantify strain transfer and strain inhomogeneity from a PFM image of a moiré superlattice, though this preliminary investigation has only scratched the surface of what utility may be found from using this inexpensive, computationally accessible technique on the wide variety of AFM images of moiré superlattices generated in the course of 2D materials research. Future experimental work and theoretical investigation will likely provide clearer bounds on the limitations and opportunities for this technique, as well as on the underlying lattice strain and rotation.

Chapter 5 | Engineering robust strain transmission in van der Waals crystals and heterostructures

This chapter consists of my as-yet unpublished work: John Cenker†, **Jordan Fonseca**†, Mai Nguyen†, Chaowei Hu, Jiun-Haw Chu, Xiaodong Xu, "Engineering robust strain transmission in van der Waals crystals and heterostructures," *in preparation* (2024) X.X., J.F., and J.C. conceived of the experiment. C.H. synthesized and characterized bulk Bi_2SeO_5. J.C., J.F., and M.N. prepared samples. J.C., J.F., and M.N. performed optical measurements. J.C., J.F., and M.N. wrote the paper, with input from all authors. All authors discussed the results. J.C., J.F., and M.N. all contributed equally to this work.

The mechanical deformation of a crystal lattice by strain can have profound effects on the material's properties[79,273–275]. In bulk crystals, strain has been shown to be an effective tuning knob of several quantum phenomena including magnetic[12,13], superconducting[14,276], and topological states of matter[143,277]. The accessible strain range in standard experiments is limited by the strength of the crystal, which depends on the number of defects and imperfections in the crystal. Reducing the dimensionality of the crystal from the 3D bulk to the 2D limit reduces the total number of defects, making atomically thin van der Waals (vdW) crystals the strongest materials ever measured[77,247]. In addition to their exceptional strength, these materials and their heterostructures host fascinating 2D quantum phases including correlated insulating states[44,47,52], nematicity[278–281], frustrated magnetic orders[46,172,282–284], and integer and fractional quantum Hall effects[233,277,285–288]. The combination of unique mechanical durability and rich physics make atomically thin van der Waals crystals a promising platform for strain engineering.

An essential ingredient for many of the quantum phases to emerge, however, is high device quality and the ability to control the carrier density and applied electric field via electrostatic gating. This is usually achieved via encapsulation[267] with hexagonal boron nitride (hBN) and/or graphite. Sandwiching the atomically thin crystals between hBN flakes screens the charge traps and roughness of the silicon substrate[267,289], protects air-sensitive materials from the environment[290], and enables the in-situ modulation of electronic properties through electrostatic gating. However, hBN and graphite have weak interfacial and interlayer strain transmission[136,291], thereby posing fundamental challenges to the realization of high-quality devices capable of sustaining large strains. To date, the maximum in-situ strain tuning of hBN-encapsulated samples is well below 1% despite efforts to clamp the sample with evaporated metal layers to increase strain transmission[292].

In this work, we investigate the interlayer strain transmission in several materials with the goal of maximizing the in-situ strain tuning capabilities in vdW heterostructures at cryogenic temperatures. We begin with the layered orthorhombic crystal CrSBr (see crystal structure in **Figure 5.1**a), as the strain response is well calibrated (Methods). **Figure 5.1**b shows Raman scattering from the phonon peak centered around 345 cm^{-1} of an unclamped thin bulk CrSBr flake deposited on a polyimide substrate with 0 V (blue) and 100 V (black) applied to the strain cell at a nominal sample temperature of ~ 5 K (**Methods**). Despite the lack of a metal clamping layer, the phonon mode exhibits a large redshift of ~ 6.8 cm^{1} when the piezo voltage is increased from 0 to 100 V. This corresponds to a uniaxial tensile strain of ~ 1.6 % using the previously determined[293] strain shift rate of ~ 4.2 cm^{-1}/%. Applying this analysis to the entire strain dependence reveals a linear application of strain with negligible change to the width of the phonon peak (**Figure 5.1**c). These results demonstrate a remarkably robust interlayer strain transmission in CrSBr, standing in

stark contrast with other common vdW materials, such as graphite, where the Raman shift under strain quickly vanishes in the few layers and bulk limit[291]. Moreover, we find that the unclamped CrSBr samples can survive to exceptionally high strains, with some samples sustaining ~ 3 % strain before slippage (**Figure 5.2**).

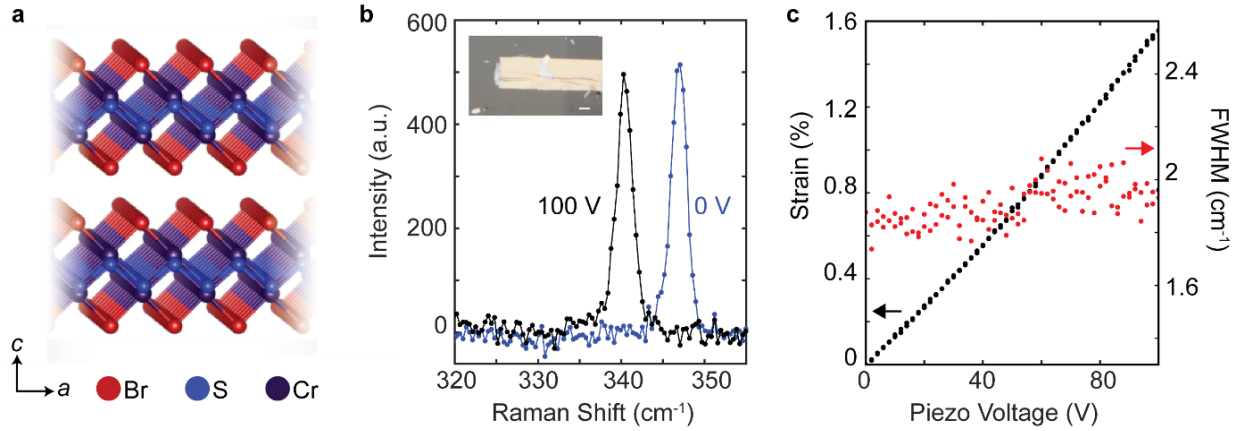

Figure 5.1: Efficient interlayer strain transmission in van der Waals crystal CrSBr. (a) Side view of CrSBr crystal structure, consisting of monolayer planes stacked along the c axis. **(b)** Raman spectra taken on a thick (> 100 nm, optical image inset) exfoliated CrSBr flake with 0 V (blue) and 100 V (black) applied to the piezoelectric strain cell. The phonon mode shifts by ~ 6.8 cm^{-1}, corresponding to a strain of ~ 1.6 % (see **Methods**). **(c)** Measured strain as a function of piezo voltage applied to the strain cell. The thick flake shows a continuous shift with little change to the full-width at half maximum (FWHM) of the Raman peak (red).

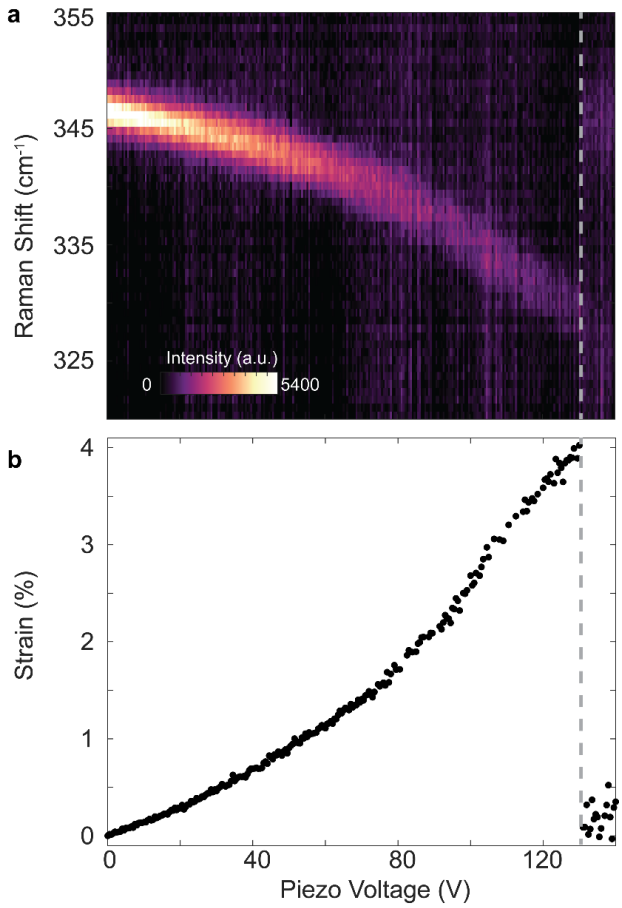

Figure 5.2: High strain behavior in unclamped thin bulk CrSBr. (a) Colormap of Raman scattering from the P_3 peak as a function of piezo voltage. **(b)** Extracted peak energy obtained by fitting the spectra with Lorentzian functions. At a large strain approaching 4% (denoted by the grey line), the sample suddenly slips and the strain is released. The measurement was performed at a nominal temperature of 40 K to increase the piezo displacement and applied strain.

The efficient interlayer strain transmission, endurance to extreme strains, and well calibrated strain response make CrSBr a convenient sensor of strain transmission in vdW heterostructures. Unlike graphene and transition metal dichalcogenides (TMDCs) which require mono- or few-layer flakes for sensing functionality, CrSBr flakes with a wide range of thicknesses can be used, significantly streamlining sample fabrication. We first test the strain transmission

through the ubiquitously used hexagonal boron nitride, which has a hexagonal lattice as shown in **Figure 5.3**a. In contrast to CrSBr, where the exterior Br bonds extend vertically along the stacking direction, the bonds in hBN are essentially entirely within the plane. Moreover, the hexagonal crystal structure has two stacking configurations close in energy[294] (with AA' being the most stable one), whereas CrSBr has only a single stable stacking configuration[293]. These differences in crystal structure can have important consequences on the tendency for soliton formation[263] and interfacial and interlayer strain transmission. **Figure 5.3**b shows the strain response of a CrSBr flake stacked on top of hBN (red) and another CrSBr deposited directly on the polyimide substrate adjacent to the hBN (black). The strain transmission through hBN is an order of magnitude less than CrSBr. Moreover, the hBN sample exhibited extreme wrinkling after the strain cycling, while the CrSBr remained unchanged (**Figure 5.4**). These results confirm that the use of hBN can limit the strain tunability of vdW devices, consistent with the reduced strain ranges reported in previous devices[292].

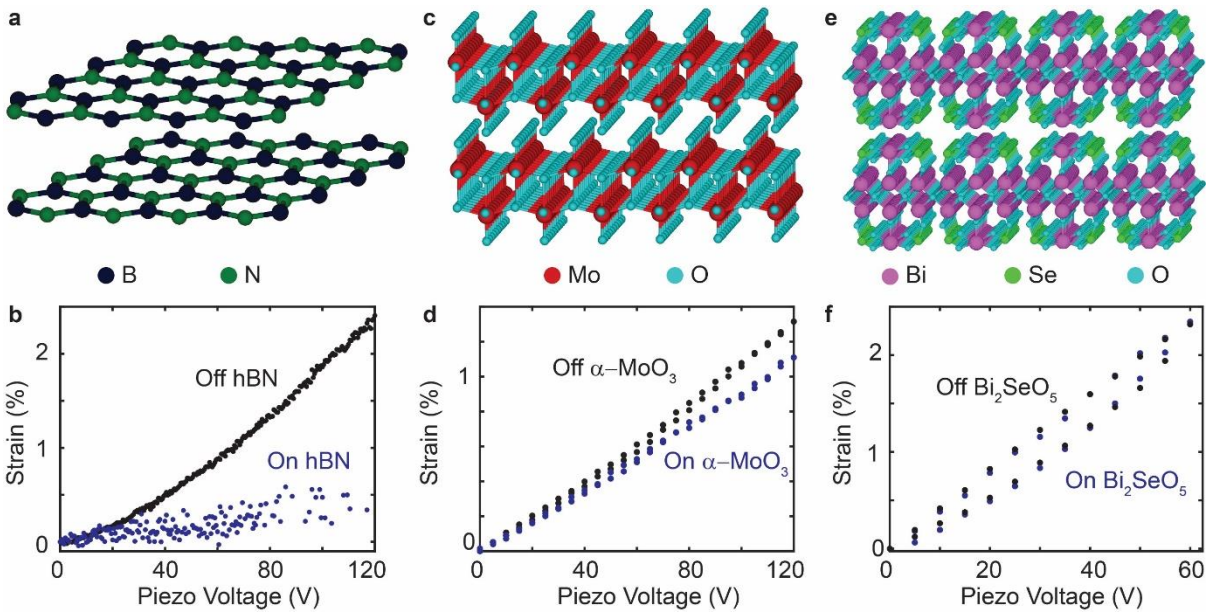

Figure 5.3: Measuring strain transmission in vdW crystals via a CrSBr strain sensor. (a) Crystal structure of hexagonal boron nitride (hBN). (**b)** Measured strain as a function of piezo voltage directly on the polyimide substrate (black) and through a thin bulk (~20-30 nm) hBN crystal. (**c-f)** Side view crystal structure and strain transmission characteristics of α-MoO_3 (**c, d**) and Bi_2SeO_5 (**e, f**). The strain in all measurements is determined by using the calibrated Raman response of a CrSBr flake deposited on top as a sensor (**Methods**).

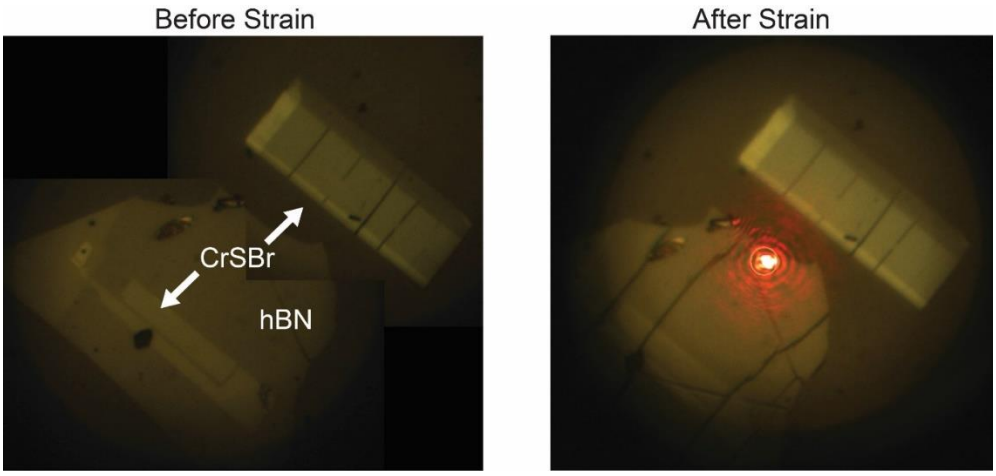

Figure 5.4: Optical images of CrSBr/hBN heterostructure before and after applying strain. Optical image of a thin bulk CrSBr flake and a CrSBr / hBN heterostructure deposited on the same polyimide substrate at 0 V before (left) and after (right) a piezo voltage of 120 V was applied to the strain cell. The hBN heterostructure demonstrates a variety of new wrinkles after strain cycling, while the CrSBr flake does not.

Since hBN is widely used as a substrate and gate dielectric in high-quality vdW devices, its poor strain transmission properties pose a significant challenge towards utilizing strain as a tuning knob for the rich quantum phases which emerge in sufficiently clean and cold 2D systems. The desirable mechanical properties of CrSBr, on the other hand, suggest that it may be used as an alternative component in new strain-tuned vdW devices and heterostructures. However, the magnetic and semiconducting properties of CrSBr can result in significant magnetic proximity and charge transfer effects[295,296]. While these effects are interesting, an ideal straintronic dielectric substrate should provide an inert, atomically flat surface akin to hBN. Fortunately, the constantly expanding number of 2D materials provides new building blocks for devices with enhanced functionality. Two materials which have recently[297–300] been identified as promising dielectric insulators are α-MoO_3 and Bi_2SeO_5. Unlike hBN and graphite, these crystals have orthorhombic

crystal structures (**Figure 5.3**c, d), with α-MoO_3 having a buckled, anisotropic crystal structure that resembles CrSBr. **Figure 5.3**e,f show the strain transmission characteristics of α-MoO_3 and Bi_2SeO_5, respectively, as measured by a CrSBr strain sensor. The strain measured through both crystals is comparable with that of the CrSBr deposited directly on the polyimide substrate, indicating efficient strain transmission.

The exceptional stability and insulating nature of Bi_2SeO_5 combined with its adequate strain transfer properties make it a particularly appealing candidate for use as a hBN substitute in high-quality vdW devices. To explore this possibility, we fabricated a top-gated monolayer WS_2 device (see schematic in **Figure 5.5a** and **Methods**). **Figure 5.5b** shows photoluminescence (PL) measurements of the monolayer WS_2 at top gate voltages of -9.8 V and 7.3 V, respectively, with the entire gate dependence shown in **Figure 5.6**. Due to the n-type doping in WS_2, the negative gate voltage brings the Fermi level closer to charge neutrality, while applying a positive top gate voltage efficiently dopes electrons into the monolayer. Based on previous reports[301], we assign the exciton features at low doping as the neutral exciton (X^0), negatively charged trion (X^-), and biexciton (XX). In the highly doped spectra, however, a single peak dominates the spectra. We label this peak as $X^{-'}$ following the convention used for monolayer WSe_2. We note that the origin of $X^{-'}$ in TMD monolayers is still unclear, with previous works in WSe_2 suggesting exotic many-body states[302], trion fine structures[31], or the second trion charging state[301,303]. The detailed experimental and theoretical understanding of this peak is beyond the scope of this work. Yet, the simplicity of the highly doped spectra makes it a more convenient probe than the more complicated undoped one. Importantly, the strain shift rate of $X^{-'}$ is very similar to the neutral exciton (see **Figure 5.8** and **Methods**).

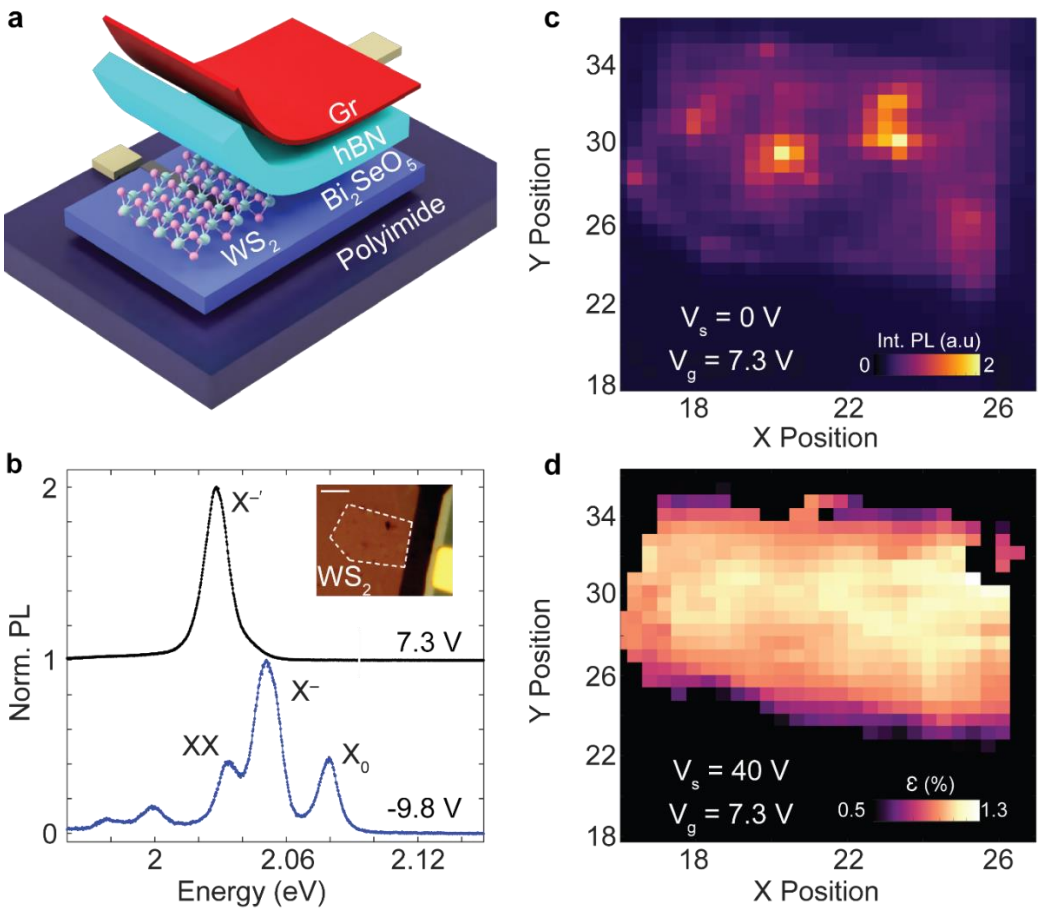

Figure 5.5: Bi_2SeO_5: a promising straintronic dielectric substrate. (a) Schematic of top-gated strain tuned vdW device. A standard graphite/hBN top gate is used to pick up and stack a monolayer WS_2 flake onto a pre-patterned platinum (grey) contact deposited on top of the bottom Bi_2SeO_5 layer. The entire device is assembled on a flexible polyimide strain substrate which is then attached to the strain cell. (**b)** Photoluminescence measurements of the monolayer WS_2 device at top gate voltages of -9.8 V (blue) and 7.3 V (black). An optical image of the device is inset, scale bar 5 µm. (**c)** Spatial map of PL intensity integrated over the entire spectral range with voltages of 0 and 7.3 V applied to the strain cell and top gate, respectively. (**d)** Spatial mapping of tensile strain taken at a piezo voltage of 40 V (**Methods**).

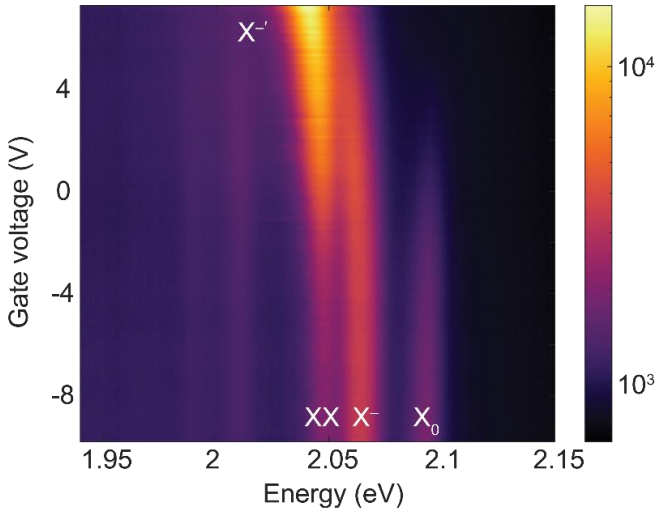

Figure 5.6: Gate-dependent photoluminescence of monolayer WS_2 strain device. PL measurements taken with 0 V applied to the strain cell as a function of voltage applied to the top gate. The sample is excited by σ^+ light, and the detected signal is co-circularly polarized with respect to the excitation.

To confirm the high quality of the sample and to study the homogeneity of strain transmission in the heterostructure, we performed spatial mapping at different piezo and gate voltages. **Figure 5.5**c shows the spatial dependence of PL from the sample with the gate voltage fixed at 7.3 V, i.e., high electron doping. In this condition, strong PL is observed across the sample, with enhanced intensity at certain spots corresponding to bubbles or contamination commonly found in vdW heterostructures[304]. When the piezo voltage is increased, the spectra red shift as expected for tensile strain[305,306]. Extracting the peak energy at every point with Gaussian fits and comparing with the 0 V value (see **Methods** and **Figure 5.7**) enables the construction of a strain map as presented in Figure 5.5d, which shows the spatial dependence of strain at V_p = 40 V. The sample shows a large (> 1%) relatively homogeneous strain throughout the majority of the heterostructure region. These results further confirm that Bi_2SeO_5 is capable of sustaining and

transmitting large strains, thereby demonstrating a new, bottom-up path towards strain engineering in optoelectronic vdW devices that does not rely on metal clamping schemes which are less robust to large strains and may also induce spatially inhomogeneous strain[292].

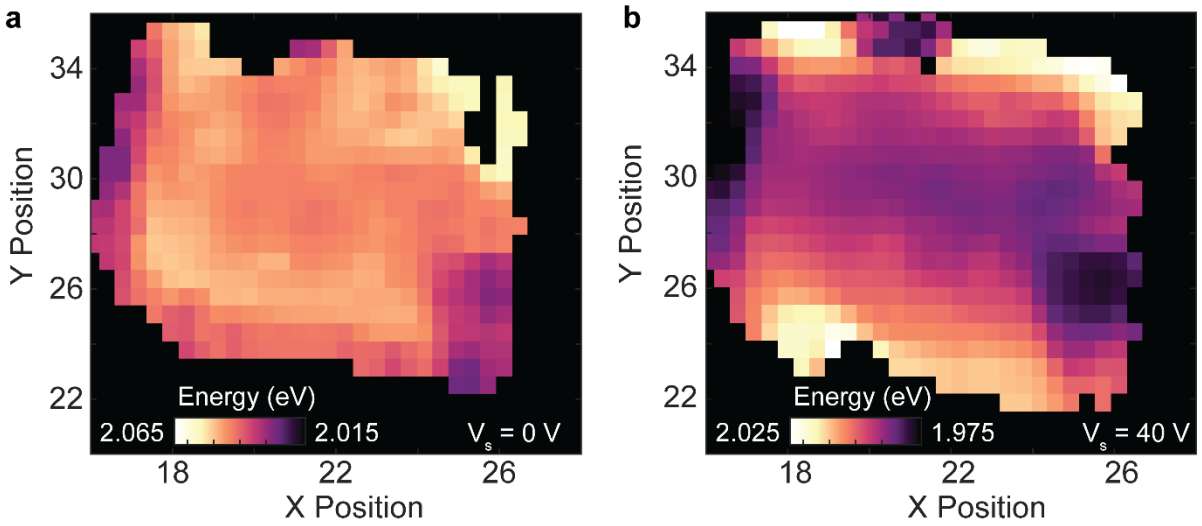

Figure 5.7: Spatial map of photoluminescence energy at low and high strains. PL spatial maps at strain voltages of 0 V (**a**) and 40 V (**b**) with an applied gate voltage V_g = 7.3 V. The peak center energy is obtained by a Gaussian fit of X^{-} at each coordinate.

The ability to apply large strain to a gated monolayer semiconductor device at cryogenic temperatures enables the study of strain effects on the rich excitonic species in these systems. **Figure 5.8**a and **Figure 5.8**b show strain-dependent co-circularly polarized, i.e., both exciting with and collecting σ^+ light, PL measurements taken at gate voltages of -9.8 V and 7.3 V, respectively. The spectra show continuous tuning with piezo voltage, with the PL energy returning to the same value when the strain is cycled (**Figure 5.9**), further confirming the efficient strain transfer and lack of slipping in the heterostructure. By fitting the piezo voltage dependent spectra in both cases, we find that all features exhibit a similar energy shift under strain (**Figure 5.8**c). On the other hand,

the change in degree of circular polarization (DOCP), given by $\frac{\sigma^+-\sigma^-}{\sigma^++\sigma^-}$, of the peaks shows noticeable differences, with $X^{-'}$ having a larger change than the other exciton species.

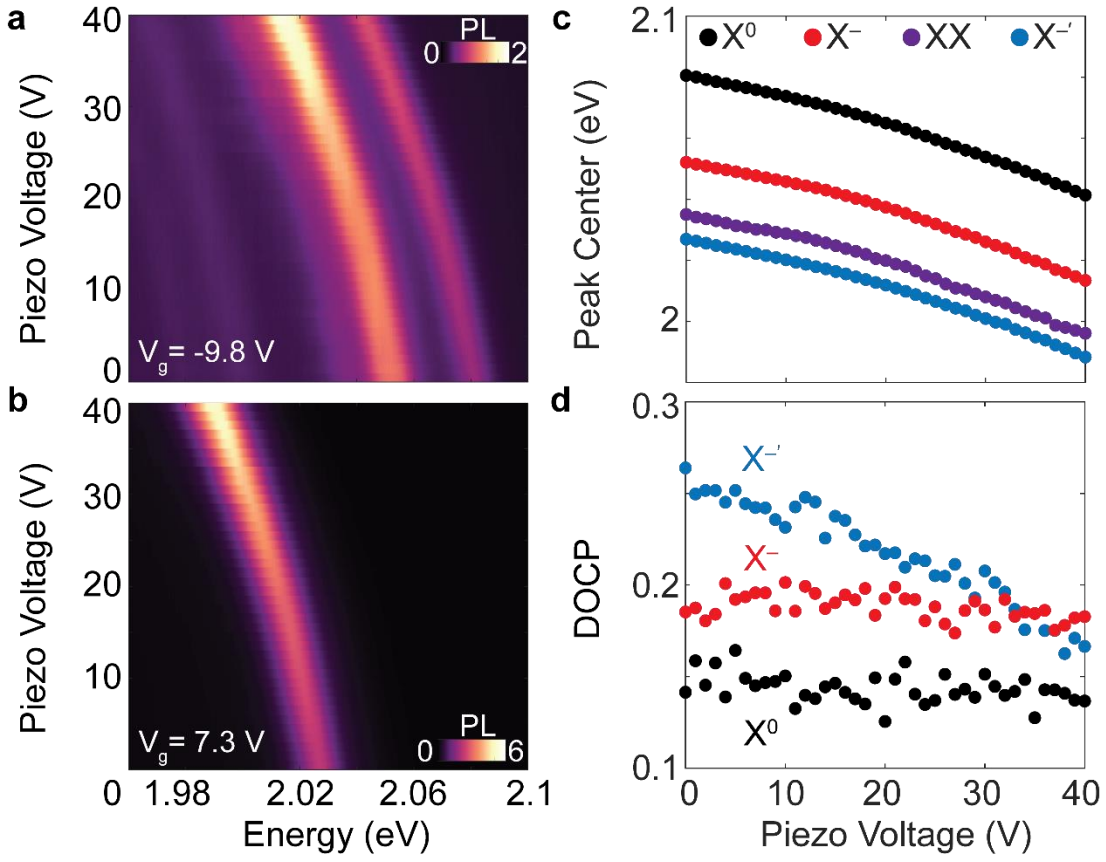

Figure 5.8: Strain tuning of exciton species in monolayer WS_2. (a, b) Strain-dependent co-circularly polarized photoluminescence measurements with the top gate voltage fixed at -9.8 V (**a**) and 7.3 V (**b**). (**c**) Extracted peak energy and degree of circular polarization, DOCP = $\frac{\sigma^+-\sigma^-}{\sigma^++\sigma^-}$, of the various PL peaks as a function of piezo voltage obtained from the spectra in (**a**) and (**b**).

Due to the strong optical selection rules in monolayer TMDCs, the DOCP is a readout of valley polarization[31,35]. The measured decrease in circular polarization with increasing strain has been observed in previous works with explanations including the decrease in the energy difference of the valence band at the Γ and K points of the Brillouin zone[94], a reduction of the 3-fold rotational

symmetry due to the uniaxial strain[307], and changes in the electron-hole exchange interaction[308]. Modeling the contribution of these different effects to our experimental observations is an interesting direction for future theoretical investigations. Understanding the origins of the strain-dependent DOCP may prove useful in establishing the true nature of the X^{-}‘ peak since it has a larger strain dependence than the other exciton and trion features. In this regard, the expanded strain range combined with gating capabilities in our devices may provide a powerful tool for both controlling and understanding excitonic physics in 2D semiconductors.

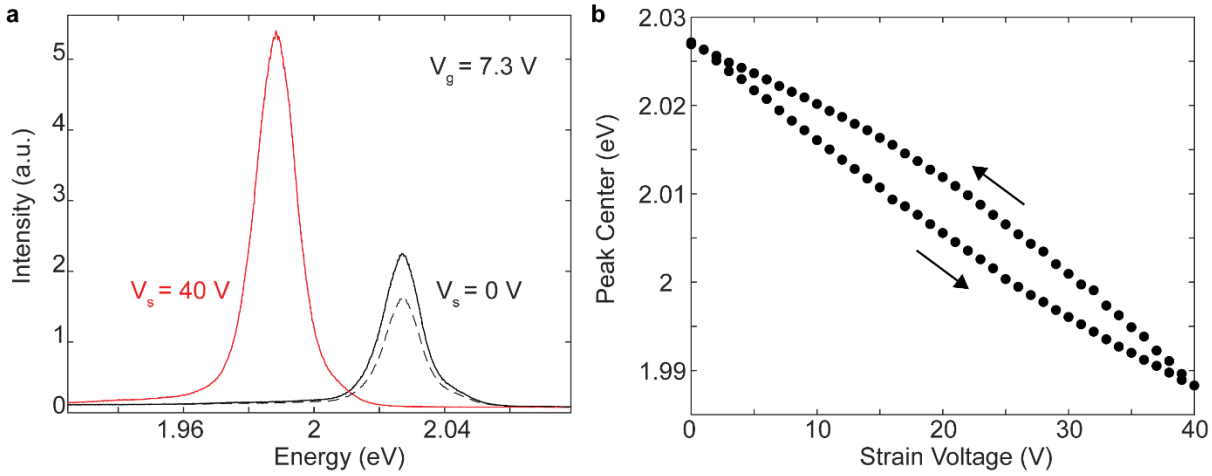

Figure 5.9: Photoluminescence measurements taken during strain cycling. (a) PL spectra taken as the strain is swept from 0 V (solid black curve) to 40 V (red) and then back to 0 V (dashed black curve). The gate voltage is kept fixed at 7.3 V. **(b)** Extracted peak position plotted for versus applied strain voltage for sweep in (a).

In conclusion, we have explored the strain transmission characteristics in vdW crystals and heterostructures. We found that the robust interlayer strain transmission in recently studied orthorhombic crystals CrSBr, α-MoO_3, and Bi_2SeO_5 enable the fabrication of high-quality straintronic vdW devices capable of sustaining strains well over 1% at cryogenic temperatures. Moreover, our work provides new guidance and opportunities for engineering strain transmission

in vdW devices. For instance, fabricating heterostructures which combine materials with weak and strong strain transmission, i.e., hBN and Bi_2SeO_5, respectively, may enable the design of on-demand and in-situ tunable strain gradients. These results could enable the combined exploration of electrostatic gating and large homo- and heterogeneous strains effects on 2D quantum matter for the first time.

Methods

Sample fabrication and strain calibration: Bulk CrSBr crystals were grown following the same recipe[309] as before. The bulk α-MoO_3 and WS_2 crystals were purchased from a commercial source (2D semiconductors). Single crystals of Bi_2SeO_5 were grown by the chemical vapor transport method[299]. Around 1 g of Bi_2O_3 powder (Alfa Aesar, 99.999%) and SeO_2 powder (Alfa Aesar, 99.999%) are mixed and ground together with the molar ratio of 1:1. The mixture was then sealed in an evacuated quartz tube under vacuum with 20 mg of I_2. The growth was performed in the one-zone furnace with the temperature set at 860 °C in the center of the furnace. In 40 days, mm to cm sized plate-like Bi_2SeO_5 single crystals were obtained at the cold end. The crystal is subsequently characterized by X-ray diffraction using a Rigaku MiniFlex 600 system, with a Cu source and Hy-Pix 400MF 2D detector to confirm its phase.

The bulk crystals were exfoliated using standard methods and suitable flakes were identified by optical contrast. The strain sensing heterostructures were then assembled through a dry transfer technique with a stamp consisting of a polypropylene carbonate (PPC) film placed on a polydimethylsiloxane (PDMS) cylinder. The CrSBr strain sensor flake was picked up followed by the target crystal (either hBN, α-MoO_3, or Bi_2SeO_5) and deposited onto the polyimide strain substrate. The strain substrate consisted of transparent 20 μm thick polyimide epoxied onto flexure

sample plates produced by Razorbill instruments with Stycast 2850 FT epoxy. The long axis of the CrSBr flake was aligned with the strain axis for consistency with the previous studies[293].

To fabricate the gated monolayer WS_2 device, we first dropped a Bi_2SeO_5 flake on the polyimide substrate and evaporated platinum contacts of ~ 7 nm thickness which were connected to larger Cr/Au (7 nm / 70 nm thick) pads following standard lithography techniques. After patterning the Bi_2SeO_5, we cleaned the surface with several rounds of contact mode AFM cleaning. Then, we picked up graphite, hBN, and monolayer WS_2 with a polycarbonate (PC) / PDMS stamp. The device was completed by melting this stack down so that the monolayer WS_2 contacted the platinum, and the top gate graphite contacted a separate gold contact.

After fabrication, the sample plate was screwed into a symmetric three-piezo strain cell previously with the same design used in our previous experiments. For the strain sensing measurement, we used the same Raman shift rate of ~ 4.2 cm^{-1}/% for the mode near ~ 346 cm^{-1} that we determined previously[38]. In all measurements, we use the zero piezo voltage value as the zero-strain reference, which does not account for potential built-in strains during fabrication. Additionally, we note that there are a variety of reported PL shift rates for TMDC monolayers[108]. For this study, we used a rate of 50 meV/%, which is consistent with the majority of the literature values. The energies of the optical features were obtained by fitting the Raman and PL spectra with Lorentzian and Gaussian functions, respectively.

Optical measurements: Optical measurements were performed using a backscattering geometry in two closed-cycle helium cryostats: Opticool by Quantum Design (α-MoO_3 strain transmission, Figure 5.3b) and C2 by Montana Instruments (all other measurements). An objective lens focused 632.8 nm light from a He/Ne laser to a spot size of ~ 1 μm. For Raman measurements, a He/Ne laser with wavelength of 632.8 nm and power below 1mW was used. The collected signal was

dispersed using a 1800 mm^{-1} groove-density grating and then detected by an LN-cooled charge-coupled device (CCD). BragGrate^{TM} notch filters were used to filter out Rayleigh scattering down to ~10 cm^{-1}. A roughly linear background from the polyimide substrate was subtracted to increase the accuracy of the fitting results. For photoluminescence measurements of WS_2, we used a laser wavelength of 532 nm and power of 10 μW. The collected PL was dispersed by a 600 mm^{-1} groove-density grating and detected by a CCD.

Chapter 6 | Cryogenic strain tuning of moiré excitons in gated WS_2/WSe_2 heterostructures

This chapter consists of my as-yet unpublished work that to date only appears in this dissertation. Author contributions are as follows: X.X., J.F., and J.C. conceived the experiment. C.H. grew and characterized Bi_2SeO_5, J.Y. grew WSe_2, and K.W. and T.T. synthesized hBN. J.F. fabricated samples, assisted by J.C., M.N., E.Z., X.W., and G.R. Z.L assisted with electrical wiring to devices. J.F. performed optical measurements, assisted by J.C. J.F., J.C., and X.X. wrote the paper, with input from all authors. All authors discussed the results. J.F. and J.C. contributed equally to this work.

Moiré superlattices of van der Waals semiconductors have emerged in recent years as an ideal platform for exploring a broad range of quantum phenomena[57,58]. Because the superlattice constant is determined by the twist angle or lattice mismatch between constituent flakes, the size of the moiré unit cell can be controlled during device fabrication. In addition to the twist degree of freedom, the atomic thickness of van der Waals heterostructures makes it possible to change carrier density and to apply strong and uniform symmetry-breaking electric and magnetic fields. These factors endow TMD moirés with many tuning knobs allowing them to serve as a Hubbard[310] and many-body Hamiltonian[311] quantum simulator in which electronic correlations[312], emergent magnetism[284], symmetry-broken electronic phases[313], and topological physics[314] can all be observed. In each of these cases, the symmetry and lattice constants of the constituent materials and the emergent superlattice all play an interrelated and critical role in the resulting physics.

The recent advancements in applying tunable strain to 2D materials could provide a new avenue to tune the emergent strongly correlated physics in moiré systems. Prior work in bulk quantum materials has demonstrated that magnetic[315], superconducting[316], nematic[274], and

topological phases[317] can be tuned by directly modifying the lattice constant and symmetry of a given crystal via strain. Strain has also been extensively applied to tune the electronic and magnetic structure of 2D materials[318], resulting in direct-to-indirect band structure transitions[118,319–321] and the emergence of valley magnetoelectricity[322] in monolayer TMDs. These effects may be amplified in moiré heterobilayers[323] given the incredible sensitivity of the device physics to the structural properties of the moiré. Interesting effects have been predicted in these structures, such as a strain-induced topological phase transition resulting in the formation of a topological moiré network[324]. However, much of the existing research has focused on the effects of fabrication-induced strain on moiré superlattices[87,88,91,325–327], whether intended or unintended[235]. While there is extensive research on dynamic strain-tuning of atomically thin TMDs[25,93,97,108,116,117,328] and heterostructures[74,98,114], including several reviews[251,329,330], to our knowledge, no experiment to date has successfully demonstrated large *in-situ* strain tuning of gated TMD moiré heterostructures, especially at the cryogenic temperatures required for quantum phenomena to emerge.

In this work, we study the effects of simultaneously tunable electrostatic gating and uniaxial tensile strain up to ~1% in nearly aligned WS_2/WSe_2 heterostructures at cryogenic temperatures. This is achieved by using a piezoelectric strain cell[79,293,331] (**Figure 6.1**A) to apply strain to a transparent, insulating polyimide substrate upon which the heterostructure is deposited. The device schematic is shown in Figure 6.1B, consisting of a graphite/hBN top gate, the WSe_2/WS_2 moiré heterobilayer, and a Bi_2SeO_5 bottom layer. Bi_2SeO_5 is chosen due to its efficient strain transmission in comparison to more commonly used hBN (see Chapter 5), a dielectric constant that is not altered by strain[332], and an atomically flat surface for the moiré heterostructure[299]. These advantages are described in greater detail in Chapter 5. During fabrication, contact mode cleaning

is performed to ensure clean interfaces, and PFM is used to visualize the moiré pattern and determine the twist angle before the top gate is stacked on top (**Figure 6.1**C, **Methods**). The finished device and strain flexure (**Figure 6.1**D) is carefully screwed to the strainer and wired for measurement. All data were collected at a base temperature of ~4 K unless otherwise noted.

Results

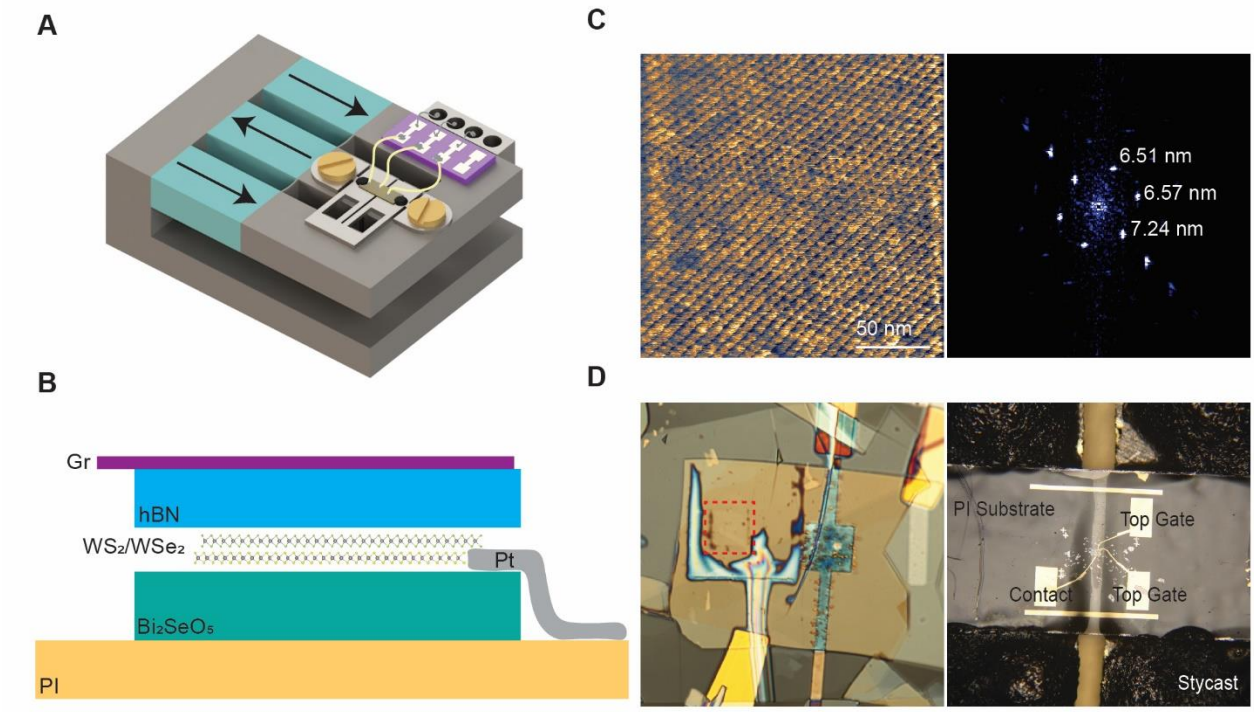

Figure 6.1: Fabrication of high-quality strain- and gate-tunable WS_2/WSe_2 moiré superlattice devices. (A) Schematic of cryogenic strain apparatus, adapted to facilitate simultaneous electrostatic gating. **(B)** Cartoon of device architecture. **(C)** PFM of moiré pattern (left) measured before addition of top gate to show device quality on Bi_2SeO_5/PI and to extract moiré wavelength and corresponding twist angle from FFT of PFM image (right). **(D)** 100x optical image of finished top-gated device on PI with heterostructure region outlined by a red dashed line (left). 5x optical image with contact pads labeled (right).

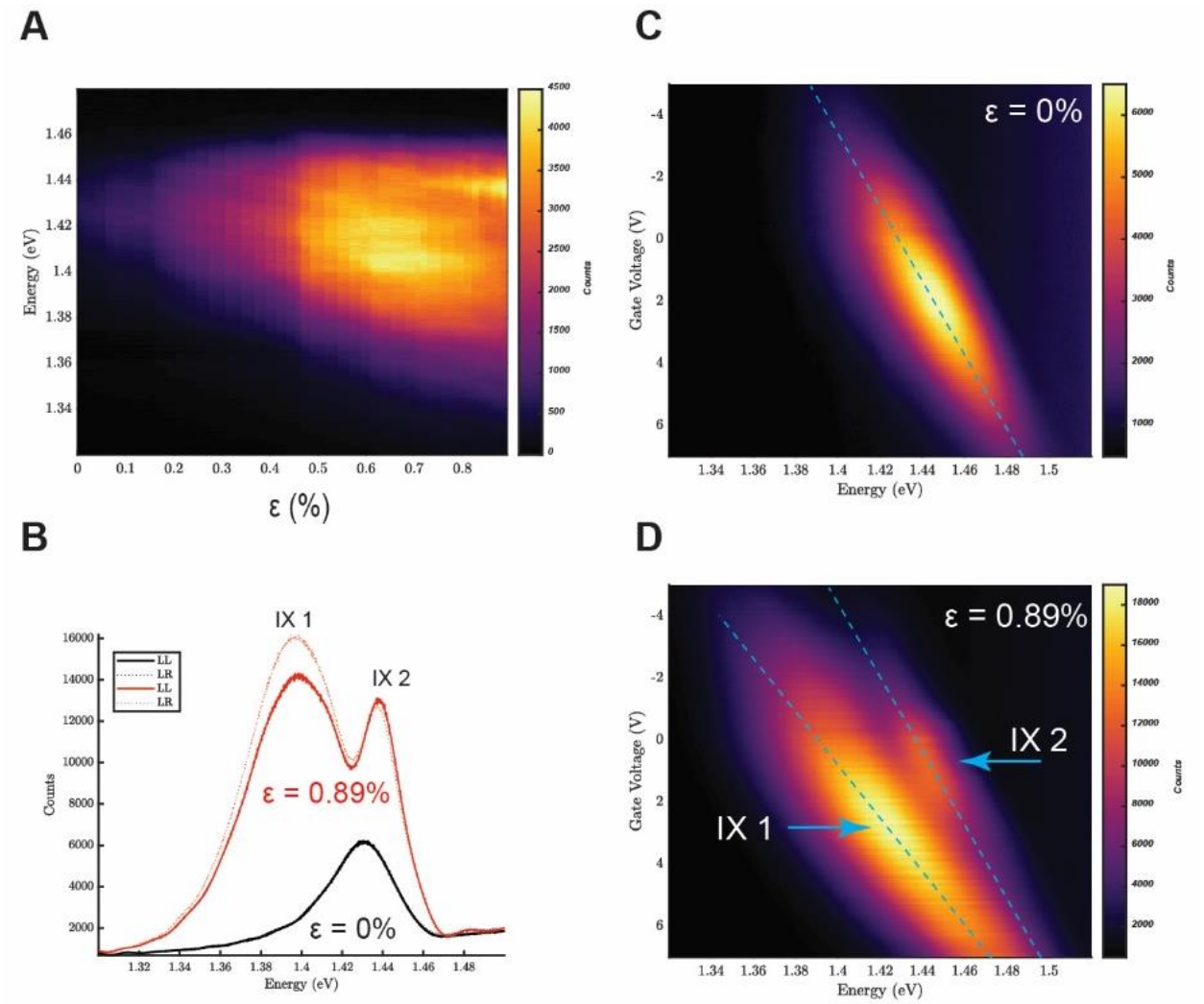

Figure 6.2: Independent gate- and strain- tunability of IX PL. (A) Strain tuning of WS_2/WSe_2 IX PL feature, which demonstrates strain transfer without slipping. Shift in emission energy and oscillator strength transfer to high energy feature at $\epsilon \approx 0.75\%$ can both be observed. **(B)** Linecuts from (C) and (D) at zero gate voltage to show change in IX PL shape and energy from $\epsilon = 0\%$ to $\epsilon = 0.89\%$. Top gate dependence of IX at $\epsilon = 0\%$ **(C)** and $\epsilon = 0.89\%$ **(D)**, shows both redshift and peak splitting under applied uniaxial strain.

We first verify the independent ability to strain and gate our sample. **Figure 6.2**A shows interlayer exciton photoluminescence as the piezo voltage applied to the strain cell is increased.

The PL spectra continuously redshift by 40 meV over 100V of applied tensile strain, corresponding to a maximum of ~0.89% additional strain in this device. We extract the conversion from piezo voltage to sample strain from Raman measurements of the WSe_2 E_{2g} mode in the measured area (**Methods**, **Figure 6.5**). We note that the reported values of strain here use the zero piezo voltage as a zero-strain reference point due to an inability to reliably measure strains which occur during fabrication and device cooling. The continuous strain shift and reversibility under loading and unloading demonstrates that this uniaxial strain is transferred to the moiré heterostructure reversibly with no slipping of the sample (Figure 6.7). As strain is applied, the spectra of the IX PL changes dramatically, switching from a single peak in the low strain condition to two distinct peaks at $\epsilon \approx 0.75\%$, which we have labeled IX1 and IX2 in **Figure 6.2**B and **Figure 6.2**D. The IX peak splitting under uniaxial strain was observed at multiple spots in this device (D1), as well as in a second measured device D2 (**Figure 6.8**).

The capability to gate the moiré superlattice device provides additional insight into the nature of IX 2. **Figure 6.2**C shows the gate dependence of the IX PL at $\epsilon = 0\%$. With a single gate, the applied gate voltage has the effect of jointly changing the out-of-plane electric field and sample carrier density. The slope in the PL results from the electric-field induced DC stark shift of the out-of-plane IX dipole moment, while the change in PL intensity is primarily a consequence of tuning the carrier density. **Figure 6.2**D plots the gate dependence at $\epsilon = 0.89\%$. At this strain, IX 2 has a dipole moment 1.5 times smaller than that of the IX 1. In addition to a different dipole moment, IX 2 is significantly more co-circularly polarized than IX 1, indicating that IX 2 has a smaller vertical spatial separation between electron and hole.

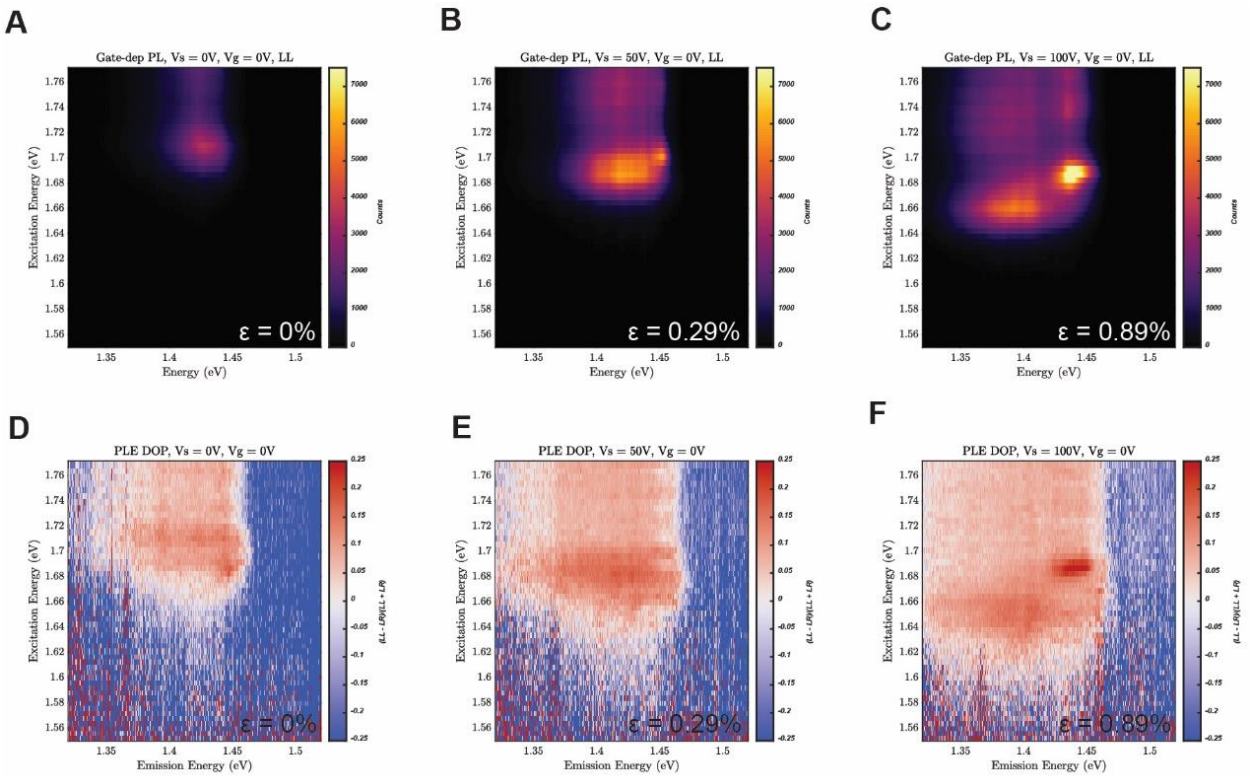

Figure 6.3: Band structure engineering with strain probed by PLE. (A-C) Strain-dependent co-circularly polarized PLE showing evolution of IX feature under increasing tensile strain. **(D-F)** DOCP associated with PLE in panels A-C showing ~100% enhancement in DOCP of IX2 relative to IX1.

In addition to the distinct dipole moment, the higher-energy IX 2 feature that appears at high tensile strain exhibits markedly different resonance and polarization response than IX 1. **Figure 6.3**A-C show photoluminescence excitation (PLE) maps taken at $\epsilon = 0\%, 0.29\%$, and 0.89%. As the strain is increased, the lowest energy WSe_2 absorption feature shifts from 1.71 eV at $\epsilon = 0\%$ to 1.66 eV at $\epsilon = 0.89\%$. Comparing this absorption-based measurement with the Raman calibration gives a gauge factor for the monolayer WSe_2 A exciton of 56 meV/%, which is consistent with the range of values reported in the literature of 47-56 meV/%[25,116,117,328], excluding the larger gauge factor of up to 109 meV/% reported when monolayer flakes are dual-encapsulated

with stretchable polymers[97]. With increasing strain, the overall IX emission is enhanced, and IX2 emerges with a strong, distinct resonance (Figure 6.3C). IX 2 emission is 40 meV blue shifted and is resonantly excited at 1.69 eV, 25 meV lower than the resonance of the IX 1 feature. Examining the degree of circular polarization (DOCP) as a function of excitation energy at $\epsilon = 0\%, 0.29\%,$ and 0.89% (**Figure 6.3**D-F) reveals that IX 2 is substantially more co-circularly polarized than IX 1 and is enhanced over a smaller wavelength window than the broader IX 1.

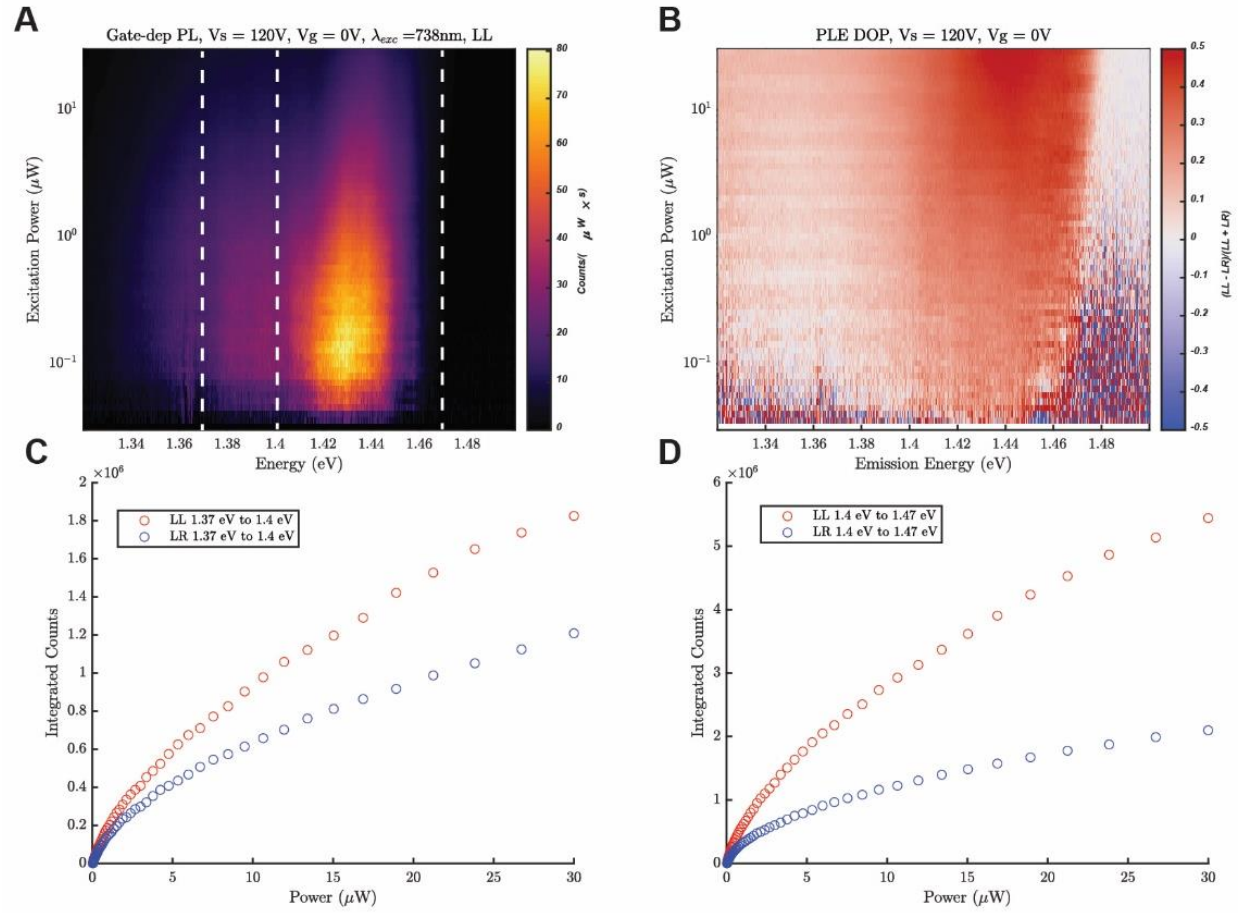

Figure 6.4: Power dependence of IX PL at $\epsilon = 1\%$. (A) Co-circularly polarized PL vs. excitation power for powers ranging from 30 nW to 30 μW. Excitation wavelength is fixed at 738 nm, and PL is normalized to excitation power and CCD integration time, so linear power dependence is represented by a constant color. The spectrum taken at 30 nW is subtracted from all

data to remove a background artifact at 1.36 eV. **(B)** DOCP for the data shown in (A). **(C)** Integrated co-circularly polarized PL from 1.37 eV to 1.4 eV versus excitation power for IX 1. **(D)** Integrated co-circularly polarized PL from 1.4 eV to 1.47 eV versus excitation power for IX 2.

From power-dependent polarization-resolved PL measurements taken at $\epsilon = 1\%$ Figure 6.4A, a few things are notable. Consistent with our other data, at high strain, IX 2 has the dominant spectral weight. Both IX 1 and IX 2 exhibit qualitatively similar super-linear power dependence up to ~120 nW followed by sublinear power dependence for increasing power. **Figure 6.4**B shows the power-dependence of the DOCP, which reveals that the DOCP for IX 2, which already exceeds that of IX 1 at minimum power, increases substantially to above a value of 0.5 at 30 μW. The difference in overall peak intensity and DOCP is more clearly illustrated by **Figure 6.4**C and **Figure 6.4**D, which show spectrally integrated linecuts of IX 1 and IX 2, respectively. The saturation of more rapid saturation of cross-circularly polarized PL from IX 2 is readily apparent.

Discussion

Our investigation of the strain- and gate- tunable WS_2/WSe_2 superlattice device reveals the emergence of a new IX species at high strain with distinct interlayer spacing, circular polarization, and power dependence. Since similar behavior is observed not only in several spots in multiple devices localized emitters due to defects are unlikely to be the origin of IX 2. One possible mechanism intrinsic to WSe_2/WS_2 moiré systems is the emergence of a higher energy interlayer exciton with a similar peak splitting of ~40 meV due to dipolar repulsion within the same moiré trapping potential.[333] However, if Hubbard-*U* repulsion were responsible for the peak splitting, higher-energy peaks would only appear above threshold exciton densities when additional excitons must fill a moiré potential well already occupied by an exciton. Since this is not the case, we rule out this potential mechanism.

It is well-known that distinct intra- and inter-layer exciton species are localized at different high-symmetry points in the real-space lattice which correspond to high-symmetry points of the reciprocal lattice. Similarly, in nearly aligned WS_2/WSe_2 heterostructures there is significant registry-dependent strain[311] that is relaxed by corrugation that alters interlayer separation within the moiré unit cell[334,335]. This change in interlayer separation is perhaps the most obvious possible explanation for a difference in out-of-plane dipole moments; however, the change in interlayer separation only ranges from 0.63 nm to 0.69 nm[334], a change of 10%, which does not explain the dipole moment reduction of up to 1.5 times that we observe in our work.

The change in degree of circular polarization between IX 1 and IX2 could arise from several causes. Perhaps the most obvious explanation for a change in circular polarization in TMD systems is a strain-induced change to spin-valley physics. Because a uniform uniaxial strain field cannot break time-reversal symmetry and a complex, periodic strain gradient is required to produce the pseudomagnetic fields that could do so, this is not a likely explanation for the polarization changes we observe. Intervalley scattering in TMD systems is mediated by phonons, however, which can be significantly tuned by strain. Furthermore, uniaxial tensile strain is known to dramatically tune exciton-phonon coupling for WS_2 and WSe_2[109,328]. Uniaxial strain reduces the lattice and moiré symmetries from C_3 to C_2, which can alter selection rules for both intra- and inter-layer excitons and phonons. It has also been predicted that under uniaxial *hetero*strain, moiré excitons in a WS_2/WSe_2 superlattice will experience a strain-induced wavefunction distribution across the moiré unit cell that alters emission DOCP[231]; however, we note that we have no direct evidence of the presence of heterostrain in our devices.

We hope that the observations shared here prompt further experimental and theoretical study into the behavior of uniaxially-strained WS_2/WSe_2 moiré heterostructures under the charge doping and electric fields applied by an electrostatic gate.

Conclusion

We have demonstrated the ability to continuously, independently, and simultaneously tune electrostatic gate and uniaxial strain up to nearly 1% in a high-quality moiré superlattice device at cryogenic temperatures while optically probing the interlayer exciton. This work extends the use of the cryogenic strain apparatus previously used to apply strain to 2D materials, leverages improved strain transfer through dielectric Bi_2SeO_5 compared to the typical hBN used for high quality devices, but is otherwise compatible with state-of-the-art fabrication techniques including multi-stage dry transfers, AFM cleaning, PFM/TFM moiré characterization, and optical measurement. We expect this technique to be fully compatible with a wide variety of additional fabrication and measurement techniques such as flake cutting/etching prior to transfer. We also note that though adaptation to each system is unique, the relatively small physical profile and simple electronics of the strain/gating cell should be compatible with cryogenic electrical transport measurements, and even more sophisticated scanning-probe techniques such as STM, sSNOM, or the recently developed QTM[228].

Our work builds on nearly two decades of developments in 2D strain techniques, optical strain characterization, and van der Waals device fabrication including AFM-based cleaning and moiré imaging. What we present here only scratches the surface of what we expect to be possible at the intersection of cryogenic, *in-situ* strain- and gate- tunability of moiré devices. In particular, we anticipate that the techniques presented here provide the ingredients to probe the effects of strain on the symmetries of many-body correlated physics of a wide variety of TMD superlattices

such as multi-particle charged species including moiré trions in $MoSe_2/WSe_2$ heterostructures (which exhibit different nematicity at distinct fractional fillings) [336–339] or the FQAHE states in twisted $MoTe_2$[233,340–342], which depend sensitively on doping and out-of-plane electric fields. Beyond superlattice physics, there are van der Waals systems that are expected to exhibit gate- and strain-tunable QAH effects[343] and serve as a platform for strain-tunable FETs[344], phenomena only discernible when the full phase space spanned by uniaxial strain and carrier density can be traversed.

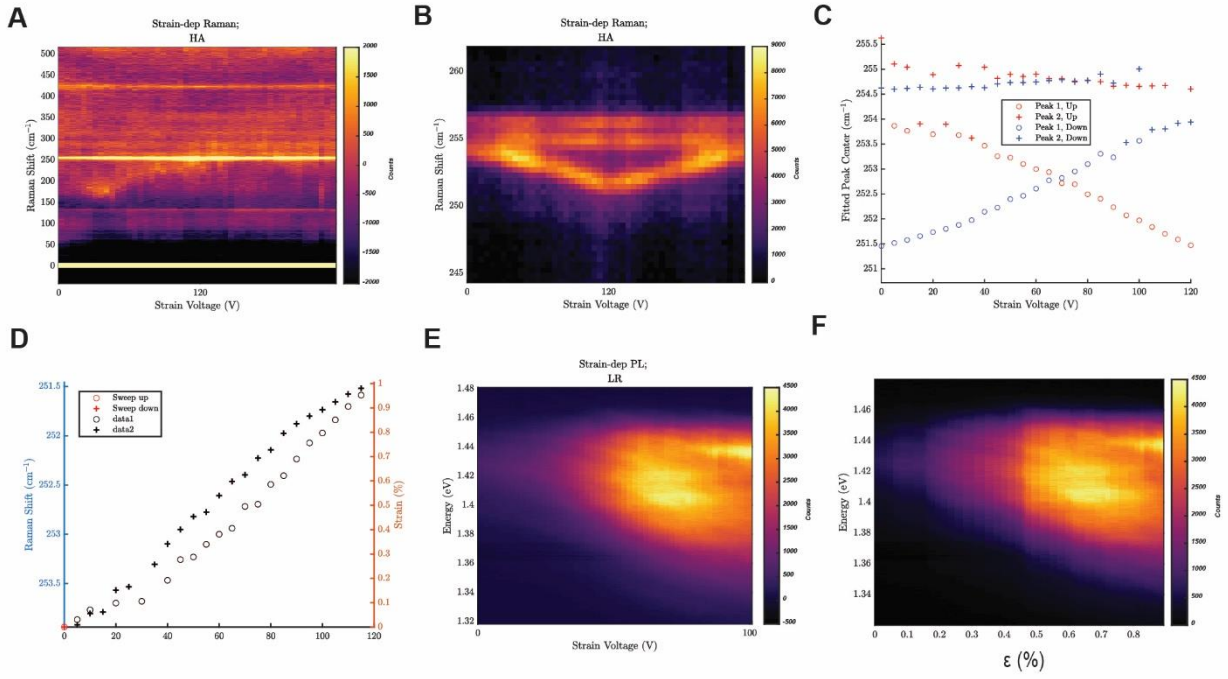

Figure 6.5: Extracting strain from Raman measurements. (A) Strain-dependent Raman measurements on the WS_2/WSe_2 heterostructure. **(B)** Expanded view of (A) to show shift of the WSe_2 A_{1g} and E_{2g} modes. The in-plane E_{2g} modes lose their degeneracy under strain, with the E_{2g}^{-} mode experiences the greatest shift. **(C)** Peak positions of the $E_{2g}^{+/-}$ modes extracted via peak fitting with an algorithm developed by Tom O'Haver[345]. **(D)** Fitted E_{2g}^{-} mode vs. strain while

sweeping up and down from (C), manually cleaned up to remove outliers and account for incorrectly fitted peaks. A calibrated strain axis is extracted based on a mode shift rate of -2.47 cm^{-1}/% tensile strain[107] (more conservative than a different report of 2 cm^{-1}/%[114]) and shown on the right. **(E)** Raw strain-dependent cross-circularly polarized PL from **Figure 6.2**A vs. applied piezo voltage. **(F)** Same data as in (E), identical to Figure 6.2A, with x-axis interpolated from strain calibration extracted from (D).

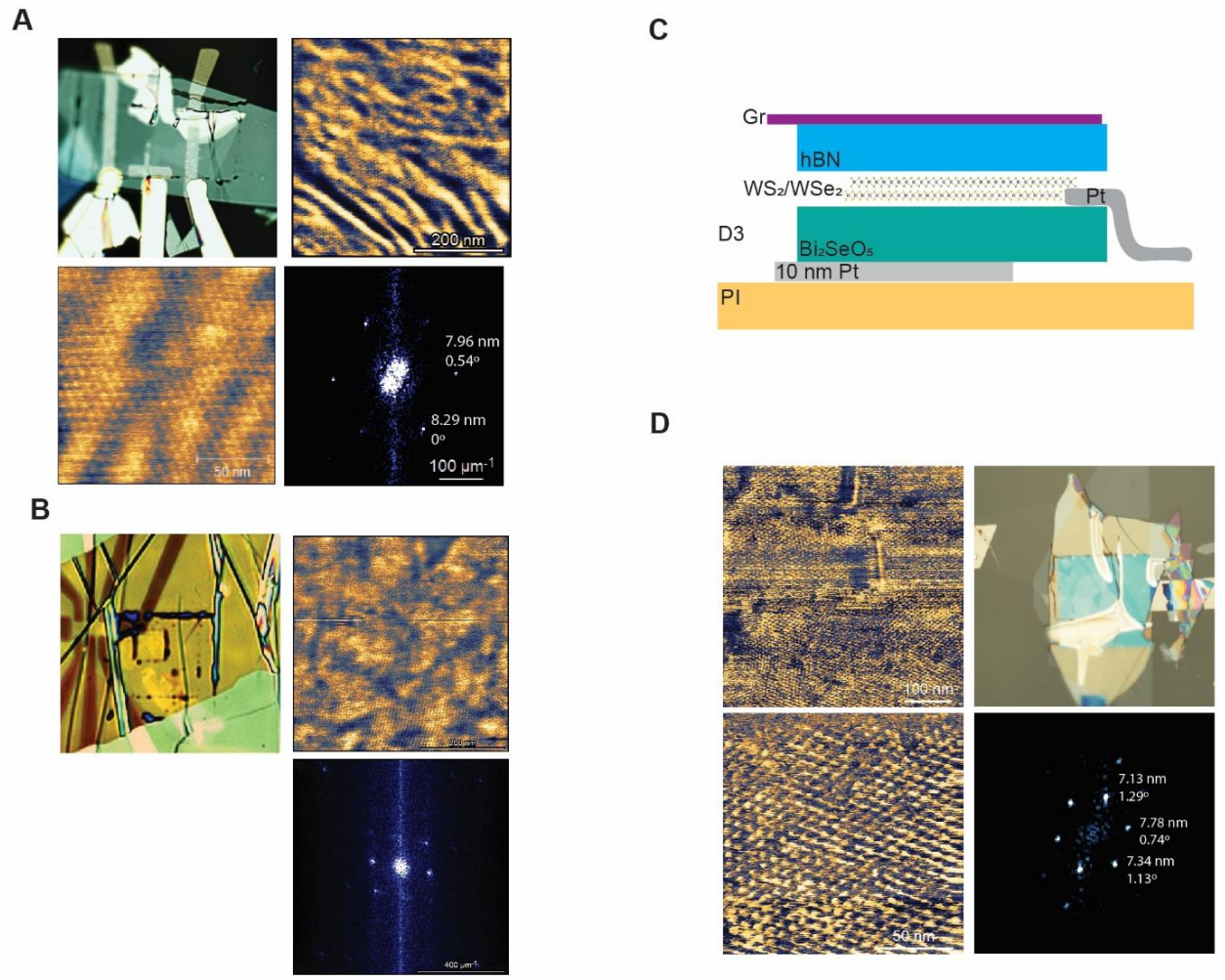

Figure 6.6: Additional measured devices. (A) Optical image, PFM, and FFT of moiré pattern for device D2, with identical stacking design as device D1 in the main text. **(B)** Optical image, TFM, and FFT of moiré pattern for device D3, with identical stacking design as device D1 and D2 in the main text. **(C)** Device D4, identical in design to D1-D3 except that 10 nm of PT are evaporated onto the PI prior to transferring the Bi_2SeO_5 to test strain transmission through a thin layer of metal that could eventually be used as a back-gate. **(D)** PFM images of moiré superlattice from D4 showing a clear moiré pattern.

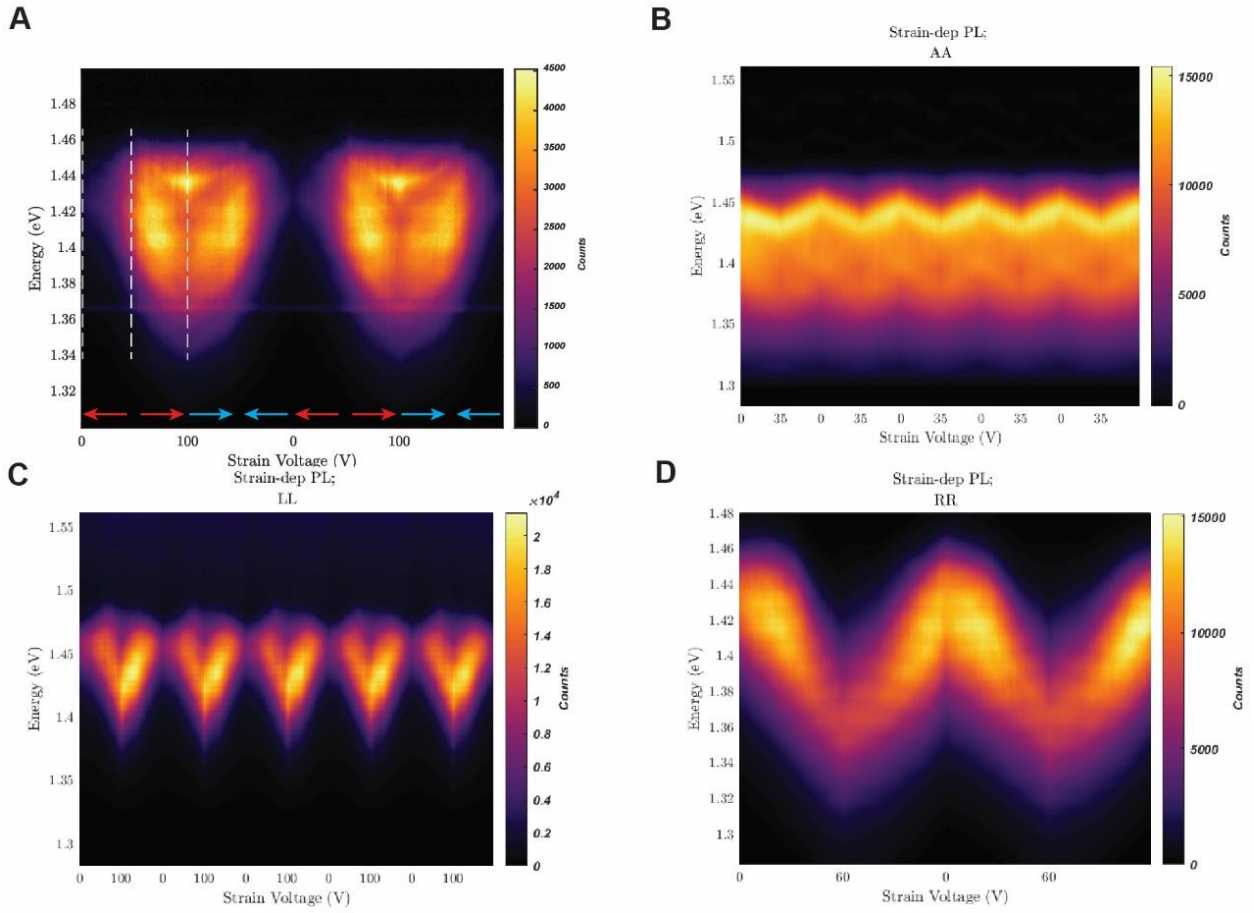

Figure 6.7: Repeatable, reversible strain cycling on D1-D3. (A) Full data set from **Figure 6.2**A showing two full strain cycles. **(B)** Strain-dependent PL on device D2 showing same repeatable, continuous redshift and blueshift of the IX PL across five cycles on a second device. **(C)** Strain cycling on D1 at a gate voltage of 3V, so IX 2 does not emerge at high strain showing consistent behavior across 5 cycles. **(D)** Strain cycling on D3 across two cycles.

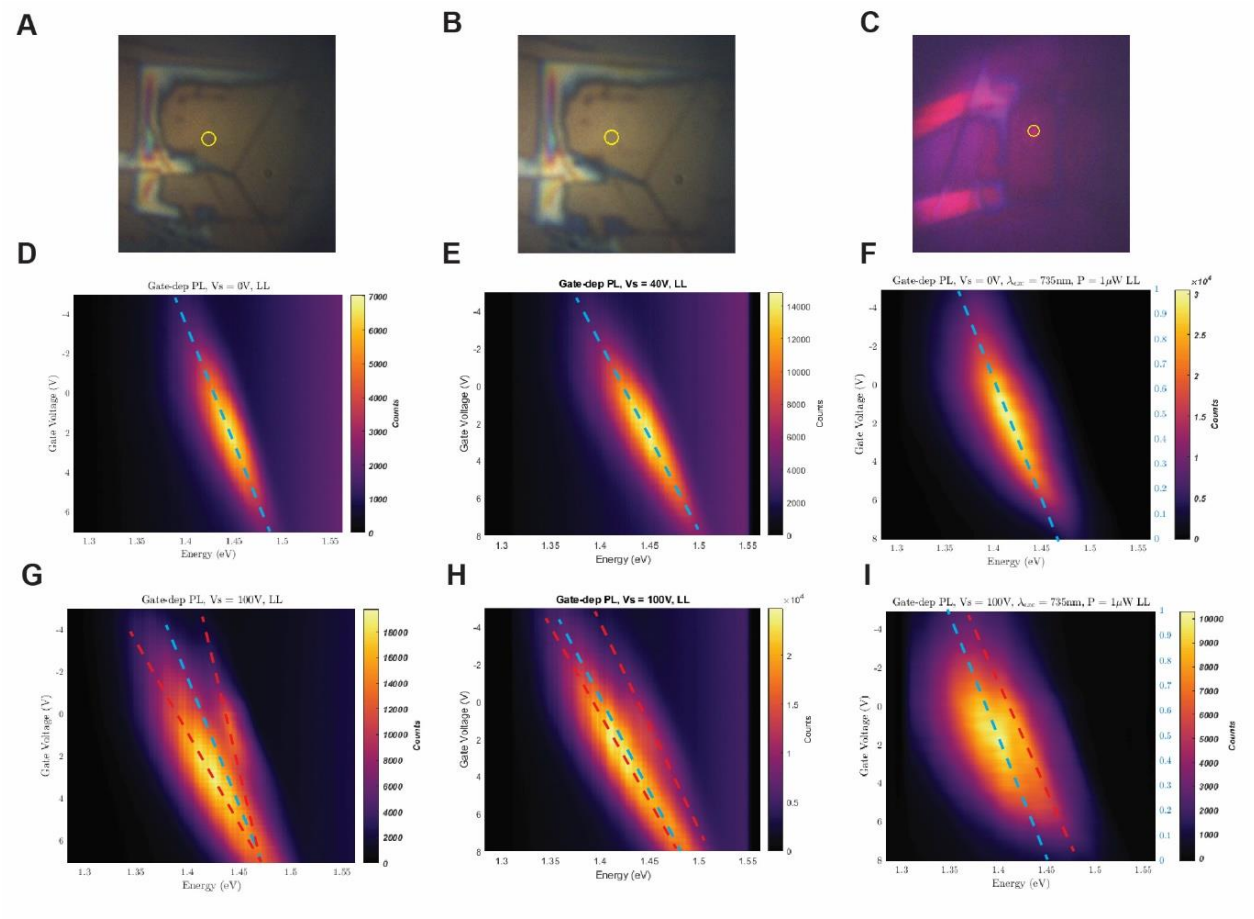

Figure 6.8: Strain-induced splitting of IX1 and IX2 at multiple spots on D1 and D2. Optical images showing two measured regions on D1 **(A, B)** and one on D2 **(C)**. Gate-dependent co-circularly polarized PL from two different spots on D1 (D, E) and one spot on D2 (F) at zero applied strain. **(G-I)** Gate-dependent PL at same spots at high strain showing emergence of secondary peak.

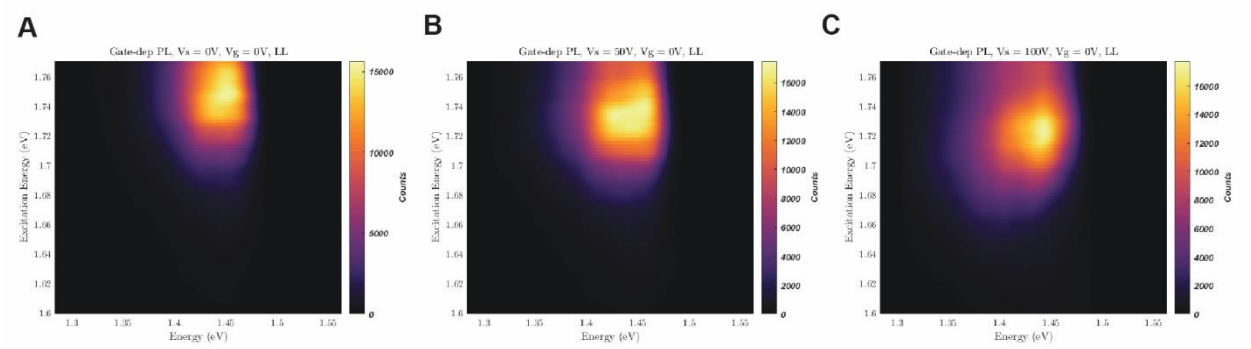

Figure 6.9: PLE at three different strains on D2. Co-circularly polarized PLE from D2 at 0V **(A)**, 50V **(B)**, and 100V **(C)** of applied strain. Though less distinct, the trends reproduce those observed from an identical measurement on D1 shown in Figure 6.3A-C.

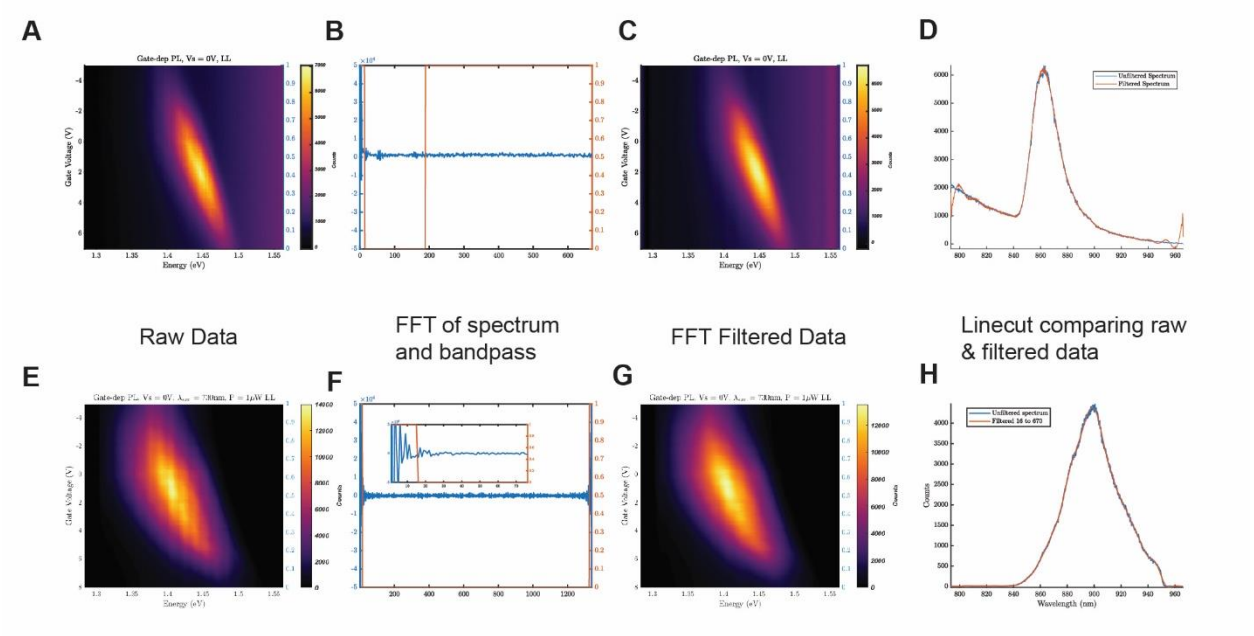

Figure 6.10: Effects of FFT Filtering PL Spectra. (A) Raw data from **Figure 6.2**C. **(B)** FFT of linecut from (A) (blue) with bandpass filter indicating that the range of values from index 14 to index 188 will be removed from the FFT (orange). **(C)** Spectra in (A) after bandpass filtering spectra at each gate voltage. **(D)** Line cuts from (A) and (C) showing the effect of FFT filtering in greater detail. **(E)** Raw data from gate-dependent PL on D2. **(F)** FFT of linecut from (E) (blue) with bandpass filter indicating that the range of values from index 14 to index 188 will be removed from the FFT (orange). **(G)** Same spectra as in (E) after bandpass filtering at each gate voltage. **(H)** Line cuts from (A) and (C) showing the effect of FFT filtering in greater detail. (E) Raw data from gate-dependent PL on D2.

Methods

Strainer cell assembly: Strain mounts depicted in **Figure 6.1**A were assembled as described in Cenker et al[293]. Additionally, a small printed circuit board (PCB) with gold pads and a set of dip sockets were attached to the Ti W-shaped block with Stycast 2850. Wires were soldered between

the PCB and the dip sockets so that devices could be electrically connected to the source voltages with gold wires secured by silver paint.

Device fabrication: Single crystals of Bi_2SeO_5 were grown by the chemical vapor transport method[299]. Around 1 g of Bi_2O_3 powder (Alfa Aesar, 99.999%) and SeO_2 powder (Alfa Aesar, 99.999%) are mixed and ground together with the molar ratio of 1:1. The mixture was then sealed in an evacuated quartz tube under vacuum with 20 mg of I_2. The growth was performed in the one-zone furnace with the temperature set at 860 °C in the center of the furnace. In 40 days, mm to cm sized plate-like Bi_2SeO_5 single crystals were obtained at the cold end. The crystal is subsequently characterized by X-ray diffraction using a Rigaku MiniFlex 600 system, with a Cu source and Hy-Pix 400MF 2D detector to confirm its phase.

To prepare the strain substrates, 25 μm transparent, insulating PI film was cut into narrow strips, cleaned with Gel Pak, and secured to Ti flexures with Stycast 2850 (Figure 6.1a). All work was done by hand under a stereo microscope. Bi_2SeO_5 flakes were exfoliated onto PDMS and then transferred from PDMS to the PI strain substrate with a standard solvent-free PPC transfer. In some cases, the PDMS with exfoliated Bi_2SeO_5 was first carefully inverted onto a Si/SiO_2 chip before the transfer. Contacts were fabricated on the Bi_2SeO_5 with a round of EBL and Pt evaporation. Subsequently, a separate round of EBL was used to deposit 50-100 nm of Au contacts. Since devices are wired with silver paste rather than bonded, no sticking layer is required to prevent Au contact peeling.

After lithography, a clean area of the Bi_2SeO_5 near the Pt contacts is AFM cleaned with an OTESPA-R3 tip engaged in contact mode at ++0.2 V with a surface velocity below 5 μm/s and a line density below the 7 nm/line corresponding to the tip radius. After cleaning, TMDs are transferred using a standard PC dry-transfer method. The relative twist angle between WS_2 and

WSe_2 is targeted to be 0° or 60°, as established from rotational anisotropy second harmonic generation on each flake prior to fabrication. After transfer and PC washoff, the heterostructure area is AFM cleaned again with similar parameters. The moiré wavelength and homogeneity are then measured using PFM, which is sensitive to the moiré domain walls[257] (recently, the mechanism for achieving phase contrast while doing PFM on Bruker Dimension Icon has been attributed to crosstalk between the torsional piezos[256]). Finally, a graphite/hBN top gate is transferred onto the device with a PC dry transfer to complete the fabrication. Because polyimide is soft compared to typical Si/SiO2 substrates, electrical contact between the PCB and the gating pads is achieved by manually gluing gold wires with silver paint.

Optical measurements: Measurements were conducted in either a Dynacool Opticool cryostat or a Montana Instruments C2 Cryostation with home-built adapters to hold the strain cell. The strain cell was controlled with a Keithley 2450 voltage source with electrostatic gating voltages applied via a DAC. Photoluminescence measurements were performed with either a 632.8 nm HeNe (for screening devices), a NKT Super continuum, or a M2 Solstis (for resonant excitation). Except as noted, excitation power was kept below 1 μW. Spectra were dispersed and collected by a Princeton Instruments spectrometer with groove density of 300, 600, or 1200 g/mm and an attached Pylon liquid nitrogen cooled CCD.

Raman measurements were performed using a 532 nm DPSS laser. Powers were kept below 500 μW, which gives an irradiance of 64 kW/cm^2 for a diffraction-limited gaussian beam with a 1 μm waist. The Raman signal was isolated from Rayleigh scatter using Bragg notch filters and dispersed on a Princeton Instruments spectrometer with groove density of 1800 g/mm and an attached Pylon liquid nitrogen cooled CCD.

Data processing: Working with devices fabricated on PI introduces a few challenges in the fabrication and measurement process that must be worked around. PI is largely transparent at optical wavelengths but exhibits a relatively strong background photoluminescence in the NIR that overlaps some with emission from the TMD intralayer and interlayer excitons. To minimize the effects of interference in our data, we FFT filter out interfering frequencies in most of the data shown here. **Figure 6.10** shows an example of this process, as well how this filtering has no material impact on the features that we are trying to highlight and study in this work. This filtering is done to make presentation of the relevant details clearer.

Additionally, in the data shown in **Figure 6.3** and **Figure 6.4**, there was a spurious background signal that could not be removed during data collection. For improved readability, this background signal is removed during post-processing. In **Figure 6.3**, the spectra taken at the lowest excitation energy (bottom of each plot) is treated as a background signal and subtracted from each spectrum. This is done for co- and cross-circularly polarized data at each strain value. In Figure 6.4, we use the spectrum taken at -6V gate voltage to be the background, which is subtracted from each spectra at each excitation power and polarization. In both of these cases, the absence of PL in the respective background spectra make this a perfectly valid background signal to use that cause negligible quantitative or qualitative changes to our data while significantly improving clarity and readability.

Conversion of applied piezo voltage to uniaxial strain: We convert the piezo voltages to applied tensile strain using the shift of the lower energy branch of the WSe_2 E_{2g} mode, which can be measured via Raman and becomes nondegenerate under uniaxial strain (**Figure 6.5**). Raman measurements were performed on the measured region of the WS_2/WSe_2 heterostructure, at the same temperatures, and during the same cryostat load as the PL data collection to improve their

reliability. Because of the butterfly-shaped stress-strain curve for piezos on loading/unloading, strain is always applied from low-strain to high-strain to improve the accuracy of our calibrated strain values. Strain values are extracted based on literature values for the shift rates of the Raman modes as a function of uniaxial tensile strain[107,114]. While this process is the best way to correlate optical measurements of a sample with applied strain and gives us a gauge factor for the WSe_2 A exciton that is consistent with literature reports[25,97,116,117,328], accurately calibrating sample strain from measurement to measurement remains a challenge of straining 2D devices.

Appendix A | Rotational Anisotropy Fitting of $MnBi_2Te_4$ SHG

We compute the XX and XY polarization dependence of our measured SHG using the techniques described in.[346]

For the *2 SL AFM state*, the combination of P_2T symmetry and mirror symmetry along the $\Gamma - K$ line restricts the effective nonlinear tensor to

$$d_{eff} = \begin{vmatrix} d_{11} & -d_{11} & 0 & 0 & 0 & 0 \\ 0 & 0 & 0 & 0 & 0 & -d_{11} \\ 0 & 0 & 0 & 0 & 0 & 0 \end{vmatrix} \text{(ref. 177)}$$

With backscattering geometry, we can construct the electric fields of the excitation beam

$$E_x = E\cos(\theta - \varphi)$$

$$E_y = \mathrm{E}\sin(\theta - \varphi)$$

$$E_z = 0$$

With θ the rotation angle of the light polarization and φ an offset between the initial polarization and crystal axis. From this excitation beam, we calculate the nonlinear polarization induced in the crystal:

$$P_x = E^2 d_{11}(\cos(\theta - \varphi)^2 - \mathrm{E}\sin(\theta - \varphi)^2)$$

$$P_y = -2E^2 d_{11}\sin(\theta - \varphi)\cos(\theta - \varphi)$$

$$P_z = 0$$

For comparison with our measurement, we convert these nonlinear polarizations into terms co- and cross-polarized with the normally incident beam using the relations

$$P_{xx} = P_x\cos(\theta - \varphi) + P_y\sin(\theta - \varphi)$$

$$P_{xy} = P_x\sin(\theta - \varphi) - P_y\cos(\theta - \varphi)$$

Finally, we model the shape of the normalized second harmonic response with

$$I_{xx}^{2\omega}(\theta,\varphi) \propto P_{xx}^2 = d_{11}^2 \cos^2[3(\theta-\varphi)] \quad \text{A.1}$$

$$I_{xy}^{2\omega}(\theta,\varphi) \propto P_{xy}^2 = d_{11}^2 \sin^2[3(\theta-\varphi)] \quad \text{A.2}$$

Nonmagnetic bulk $MnBi_2Te_4$ crystallizes in the space group $D_{3d}^{(5)}$, which is centrosymmetric with $d_{eff} = 0$ identically. At the surface, however, there is natural symmetry breaking at the interface between crystal and vacuum/substrate, which, like Bi_2Te_3 and Bi_2Se_3, has the point group symmetry C_{3v},[178,347] consisting of a three-fold rotation about the $\hat{z}$ axis and three vertical mirror planes. This point group has the following effective nonlinear tensor

$$d_{eff} = \begin{vmatrix} 0 & 0 & 0 & 0 & d_{42} & -d_{22} \\ d_{22} & -d_{22} & 0 & d_{42} & 0 & 0 \\ d_{13} & d_{13} & d_{33} & 0 & 0 & 0 \end{vmatrix} 346$$

This form, despite its apparently greater complexity, simplifies for light normally incident on the (0001) surface to produce the same six-fold pattern, but with the position of XX and XY lobes reversed:

$$I_{xx}^{2\omega}(\theta,\varphi) \propto P_{xx}^2 = d_{22}^2 \sin^2[3(\theta-\varphi)]$$

$$I_{xy}^{2\omega}(\theta,\varphi) \propto P_{xy}^2 = d_{22}^2 \cos^2[3(\theta-\varphi)]$$

Appendix B | Theory of Geometric Phase Analysis

The following derivation of the theory underlying the GPA process is reproduced from refs. [269,270,272]. We can represent an image of a periodic structure $I(\vec{r})$, such as a crystal lattice or moiré superlattice, as a Fourier decomposition of plane waves corresponding to the set of reciprocal lattice vectors $\{\vec{g}\}$, each with complex amplitude H_g:

$$I(\vec{r}) = \sum_g H_g e^{2\pi i \vec{g}\cdot\vec{r}} \quad \text{B.1}$$

The complex amplitudes of each of these wave vectors can in turn be represented by a real amplitude A_g and phase P_g.

$$H_g = A_g e^{iP_g} \quad \text{B.2}$$

We now allow that this complex amplitude can vary across the image according to irregularities in the lattice.

$$H_g \rightarrow H_g(\vec{r}) \quad \text{B.3}$$

$$I(\vec{r}) = \sum_g H_g(\vec{r}) e^{2\pi i \vec{g}\cdot\vec{r}} \quad \text{B.4}$$

If we consider the Fourier transform of the image as a continuous summation of plane waves with wavector $\vec{k}$ (which do not necessarily correspond to reciprocal lattice vectors), we can then write

$$I(\vec{r}) = \iint \tilde{I}(\vec{k}) e^{2\pi i \vec{k}\cdot\vec{r}} \quad \text{B.5}$$

But for an image of a highly periodic structure, such as a lattice, this continuous representation reduces to a discrete sum of the complex amplitudes of each *k-space representation* of the plane waves selected out by the reciprocal lattice vectors:

$$\tilde{I}(\vec{k}) = \sum_g \widetilde{H_g}(\vec{k}) \otimes \delta(\vec{k} - \vec{g}) \tag{B.6}$$

$$\tilde{I}(\vec{k}) = \widetilde{H_g}(\vec{k} - \vec{g}) \tag{B.7}$$

We can subsequently apply a masking function in reciprocal space $\widetilde{M}(\vec{k})$ that picks out a *single* reciprocal lattice vector.

$$\widetilde{H_g}(\vec{k}) = \tilde{I}(\vec{k} + \vec{g})\widetilde{M}(\vec{k}) \tag{B.8}$$

Then, by re-expressing equation B.1 with H_g given by equation B.2 and using the fact that for a real image, there is a conjugate symmetry between the Fourier components so $H_g^*(\vec{r}) = H_{-g}(\vec{r})$, we can re-express the image as

$$I(\vec{r}) = A_0 + \sum_{g>0} 2A_g \cos(2\pi\vec{g} \cdot \vec{r} + P_g) \tag{B.9}$$

The image produced by a given set of lattice fringes with reciprocal vector $\vec{g}$ selected out with the masking function is then

$$B_g(\vec{r}) = 2A_g \cos(2\pi\vec{g} \cdot \vec{r} + P_g) \tag{B.10}$$

Variation across the image of the lattice fringes masked by $\widetilde{M}(k)$ is then given by

$$B_g(\vec{r}) = 2A_g(\vec{r}) \cos\left(2\pi\vec{g} \cdot \vec{r} + P_g(\vec{r})\right) \tag{B.11}$$

We can describe this variation as a spatially dependent deviation from the reference lattice vector

$$\vec{g} \rightarrow \vec{g} + \Delta\vec{g} \tag{B.12}$$

So equation B.11 takes the final form

$$B_g(\vec{r}) = 2A_g(\vec{r})\cos\left(2\pi\vec{g}\cdot\vec{r} + 2\pi\Delta\vec{g}\cdot\vec{r} + P_g\right) \tag{B.13}$$

Importantly, the phase image $P_g(\vec{r})$ now is directly proportional the quantity $\Delta\vec{g}\cdot\vec{r}$, which captures spatially resolved deviations of the reciprocal lattice vector from the "reference" reciprocal lattice vector:

$$P_g(\vec{r}) = 2\pi\Delta\vec{g}\cdot\vec{r} \tag{B.14}$$

Thus, the *spatially dependent* phase term is a direct measurement of fluctuations of the lattice fringes from the reference lattice vector. The linear phase ramp term $2\pi\vec{g}\cdot\vec{r}$ is a typical artifact of taking the Fourier transform of a peak displaced from the origin in reciprocal space and can be subtracted from each image in data processing since it varies linearly across the image.

Taking the gradient of equation B.14 gives

$$\nabla P_g(\vec{r}) = 2\pi\Delta\vec{g} \tag{B.15}$$

This establishes the theoretical grounds for why the geometric phase of a Fourier transform of a masked reciprocal lattice vector provides a direct, sensitive way to quantify the deviation of said reciprocal lattice vector from a reference. The reader is

referred to ref. [272] and **Figure B.1**, **Figure B.2**, and **Figure B.3** for description and demonstration of how this process can be applied to real images of a moiré superlattice.

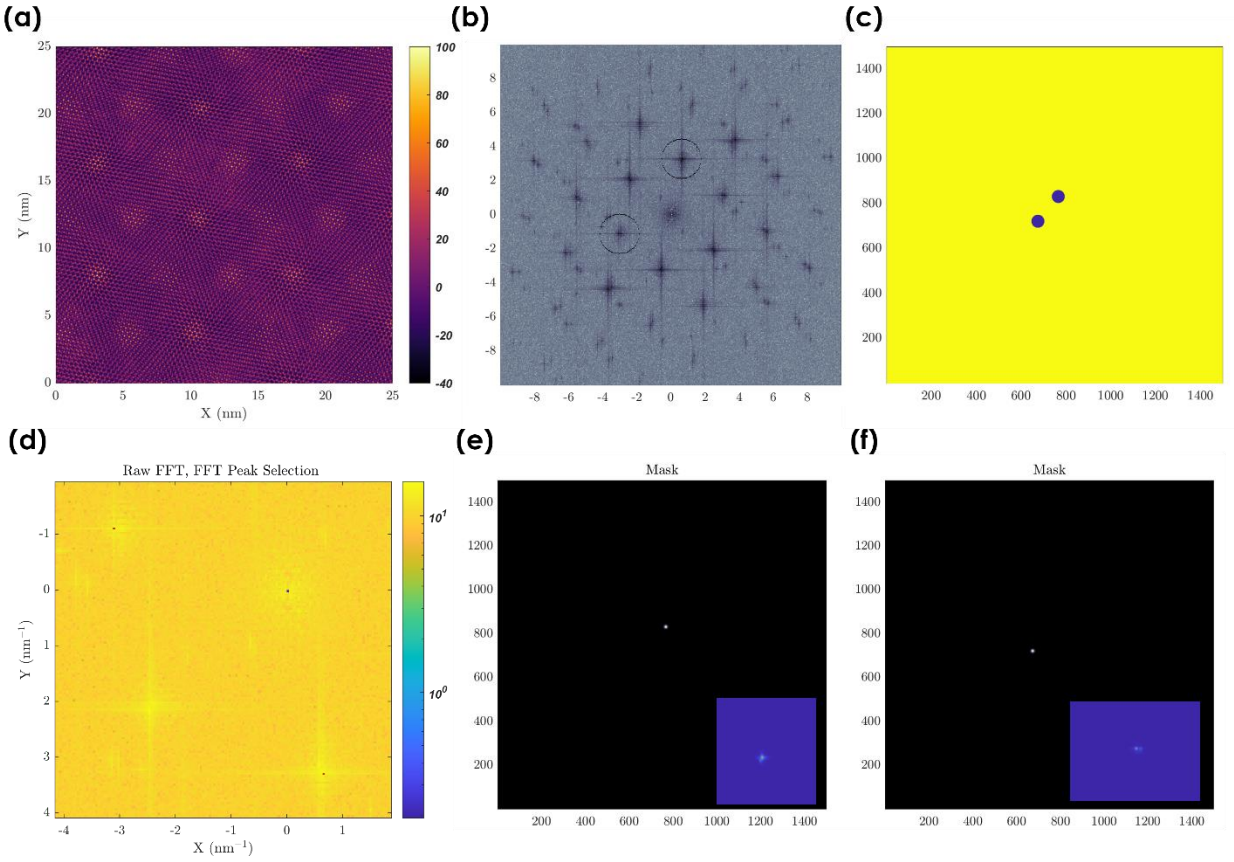

Figure B.1: Description of how peaks are selected from image for GPA. (a) Zoomed in HRTEM image of WS_2/WSe_2 moiré superlattice (same data as **Figure 4.8**a). **(b)** FFT of (a) with two peaks and masking radius identified. **(c)** Generated mask that will be applied (one circle at a time) to FFT image. **(d)** Zoomed-in image of (b) with points that will be used as reference reciprocal lattice vectors highlighted by red pixels. **(e, f)** Gaussian mask generated for each reciprocal moiré lattice vector (inset is FFT after applying mask).

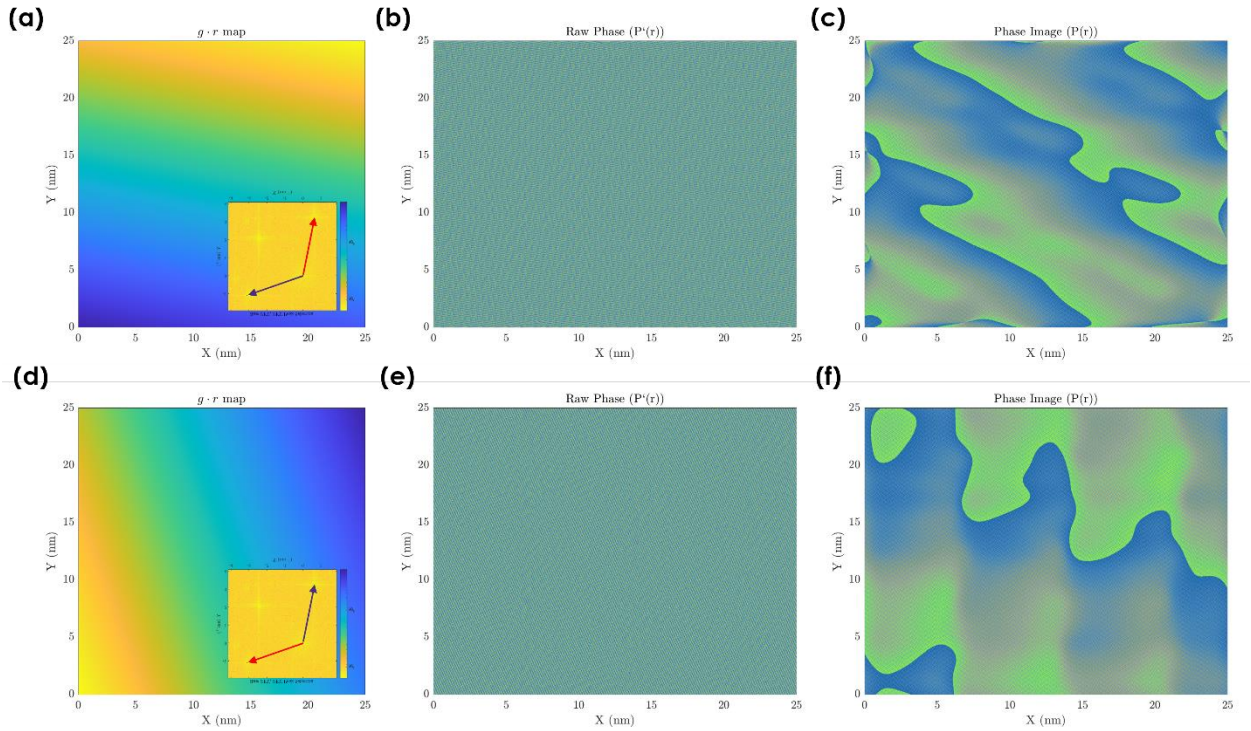

Figure B.2: Demonstration of phase image formed from each masked peak during GPA. (a, d) $\vec{g} \cdot \vec{r}$ map for each moiré reciprocal lattice vector. This map represents a linear phase ramp due to the peaks being offset from the origin. **(b, e)** Phase image $P_g(\vec{r})$ for each reciprocal lattice vector. (c, f) Processed phase image $P_g(\vec{r})$ after linear phase ramps in (a, d) have been subtracted.

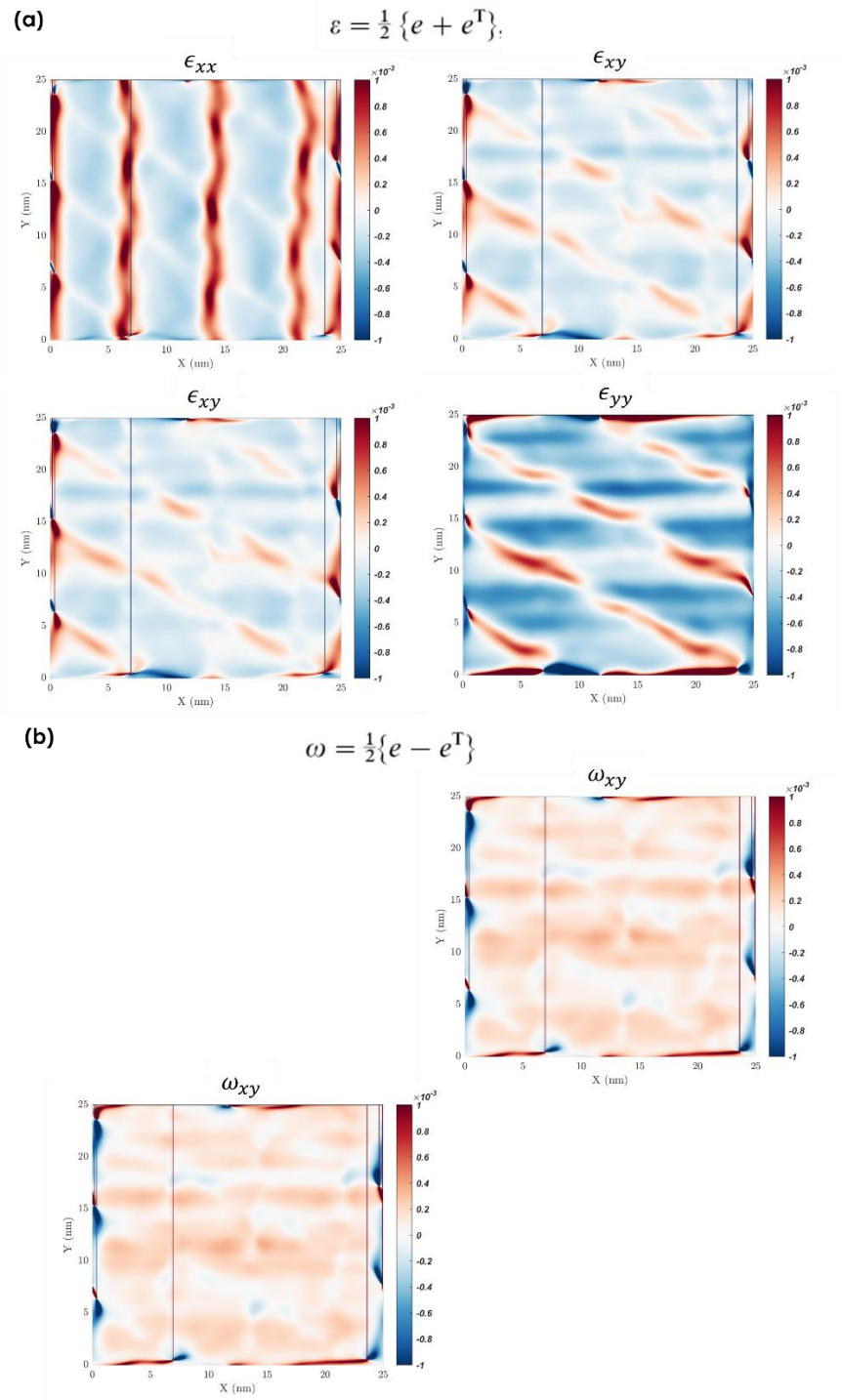

Figure B.3: Symmetrized strain and anti-symmetrized rotation matrix formed from GPA on example image shown in Figure B.1a. Symmetrized GPA-calculated strain matrix (a) and anti-symmetrized rotation matrix (b) for the data shown in **Figure B.1** and worked with in **Figure B.2**.

Appendix C | Strain-dependent PFM images and corresponding GPA matrix components

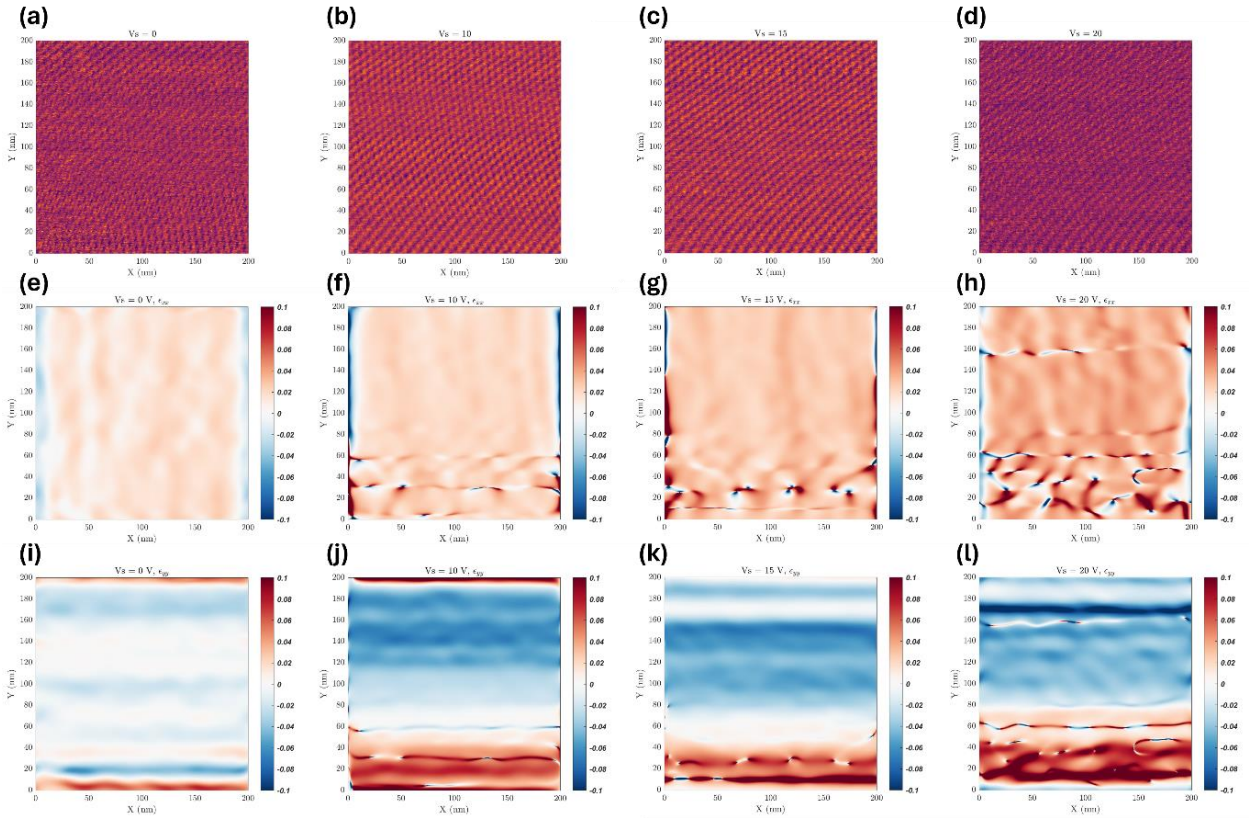

Figure C.1: Raw PFM data (a-d), GPA-computed ϵ_{xx} (e-h), and GPA-computed ϵ_{yy} (i-l) for 0V, 10V, 15V, and 20V of applied strain.

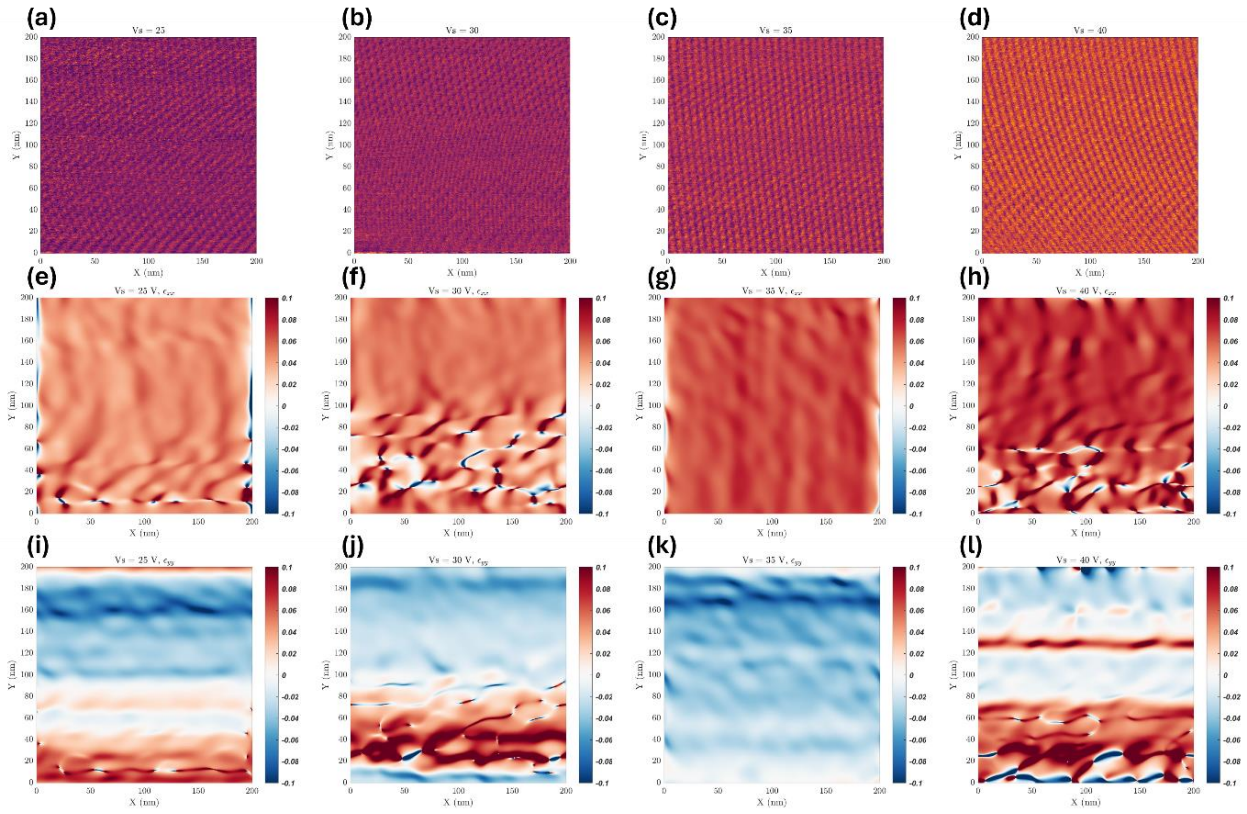

Figure C.2: Raw PFM data (a-d), GPA-computed ϵ_{xx} (e-h), and GPA-computed ϵ_{yy} (i-l) for 25V, 30V, 35V, and 40V of applied strain.

Appendix D | Tabulated Literature on Strained TMDs and Graphite

Table 1: Library of strain studies on 2D graphene, TMDs, and moiré heterostructures.

Material(s)	Temp.	Technique	Max strain	Type of strain	Classification	Ref.
Gr/Gr	RT	process-induced	Not reported	both	Experiment	88
Gr/Gr	NA	NA	NA	biaxial	Theory	253
Gr/Gr	cryogenic	stretchable substrate	<0.3%	uniaxial	Experiment	348
graphene	RT	stressor layer	Not reported		Theory/experiment	103
graphene	RT	sliding contact	Not reported	uniaxial	Experiment	65
graphene		Bent during fab	0.40%		Experiment	230
graphene	RT	process-induced	Not reported	uniaxial	Experiment	90
graphene	RT	bendable substrate	Not reported	uniaxial	Experiment	292
graphene/hBN	RT	suspension	1.80%	uniaxial	Experiment	127
hBN	RT	bendable substrate	~0.4%	uniaxial	Experiment	92
Moiré	RT	NA	NA	NA	Theory	74
MoS2	RT	process-induced	0.85%	uniaxial	Experiment	91
MoS2	RT	flexible substrate	Not reported	uniaxial	Experiment	67
MoS2	RT	bendable substrate	0.52%	uniaxial	Experiment	93
MoS2	RT	bendable substrate	0.80%	uniaxial	Experiment	94
MoS2	RT	piezoelectric film	0.35%	uniaxial	experiment	349
MoS2	RT	pressurized membrane	5.60%	biaxial	experiment	350
MoS2	RT	process-induced	0.85%	uniaxial	experiment	83
MoS2	RT	process-induced	Not reported	biaxial, local	Experiment	87
MoS2	RT	bubbles	2%	biaxial	Experiment	319
MoS2	RT		1.20%	uniaxial	Experiment	351
MoS2	RT	stretchable substrate	3.60%	uniaxial	Experiment	125
MoS2	RT	patterned substrate	1.20%	uniaxial	Experiment	352
MoS2	RT	stretchable substrate	1%	uniaxial	Experiment	120
MoS2	RT		3%	uniaxial	Experiment	353

MoS2	NA	NA	NA	uniaxial	Theory	[353]
MoS2	RT	flexible substrate	0.70%	uniaxial	Experiment	[123]
MoS2	RT	MEMS	1.30%	uniaxial	Experiment	[354]
MoS2	RT	bendable substrate	3%	biaxial	Experiment	[96]
MoS2	RT	bendable substrate	1.49%	uniaxial	Experiment	[97]
MoS2	RT	etched/bendable substrate	0.70%	biaxial	Experiment	[355]
MoS2	RT	bendable substrate	2.20%	uniaxial	Experiment	[99]
MoS2	RT	AFM manipulation	Not reported		Experiment	[356]
MoS2	RT	flexible substrate	2%	uniaxial	Experiment	[66]
MoS2/hBN	cryogenic	process-induced	0.50%	both	Experiment	[89]
MoS2/MoS2	RT	fabrication induced	Not reported	uniaxial	Experiment	[326]
MoS2/WSe2	RT	wrinkled substrate	~1%	uniaxial	Experiment	[357]
MoS2/WSe2	RT	bendable substrate	1.20%	uniaxial	Experiment	[98]
MoSe2/WS2	RT	bendable substrate	1.50%	uniaxial	Experiment	[100]
MoSe2/WSe2	RT	NA	5%	biaxial	Theory	[358]
MoSe2/WSe2	cryogenic	nanopillars	Not reported	local	Experiment	[86]
MoTe2	RT	fabrication induced	Not reported	local, biaxial	Experiment	[359]
MoTe2	RT	bendable substrate	1.90%	uniaxial	Experiment	[101]
MoTe2	RT	suspended/microcavity	0.20%	biaxial	Experiment	[360]
MoTe2	RT	bendable substrate	1.72%	uniaxial	Experiment	[118]
NA	NA	NA	NA	NA	NA	[361]
NA	NA	NA	NA	NA	NA	[250]
NA	NA	NA	NA	biaxial	Theory	[362]
NA	NA	NA	NA	NA	Theory	[363]
NA	NA	NA	NA	NA	NA	[330]
NA	NA	patterned substrate	NA	NA	Theory	[325]
TMDs			NA	NA	Theory	[364]
TMDs		NA	NA	uniaxial	Theory	[365]
TMDs	RT	bendable substrate	1%	uniaxial	Experiment	[105]
TMDs	cryogenic	temp-shrunk film	1.20%	biaxial	Experiment	[130]
TMDs	NA	NA	2.50%		Theory	[306]

TMDs	RT	piezoelectric film	small	biaxial	Experiment	[308]
TMDs	RT	bendable substrate	1.40%	uniaxial	Experiment	[108]
TMDs	RT	bendable substrate	1.48%	uniaxial	Experiment	[109]
TMDs	NA	NA	NA	both	Theory	[366]
TMDs	NA	NA	NA	uniaxial	Theory	[367]
TMDs	NA	NA	NA	biaxial	Theory	[368]
TMDs	RT	thermal substrate	3%	biaxial	Experiment	[95]
TMDs	RT	bendable substrate	0.20%	uniaxial	Experiment	[25]
TMDs	NA	NA	NA	uniaxial	Theory	[369]
TMDs	RT	bendable substrate	3.59%	uniaxial	Experiment	[110]
TMDs/moiré	NA	NA	0.50%	uniaxial heterostrain	Theory	[370]
variety	RT		NA	uniaxial	Theory	[254]
WS2	RT	bending apparatus	0.51%	Biaxial	Experiment	[122]
WS2	RT	suspended/conformed		biaxial	Experiment	[24]
WS2	RT	bendable substrate	2.50%	uniaxial	Experiment	[111]
WS2	RT	patterned substrate	NA	local	Experiment	[371]
WS2	RT	bendable substrate	0.78%	uniaxial	Experiment	[112]
WS2	RT	bendable substrate	0.70%	uniaxial	Experiment	[113]
WS2, MoS2	RT	patterned substrate		local	Experiment	[85]
WS2/WS2	RT	fabrication induced	0.40%	heterostrain	Experiment	[372]
WS2/WSe2	RT	bendable substrate	1.36%	uniaxial	Experiment	[114]
WS2/WSe2	RT	stretchable substrate	1.60%	uniaxial	Experiment	[126]
WS2/WSe2	RT	bendable substrate	0.75%	uniaxial	Experiment	[115]
WSe2	cryogenic	Suspension, gate	3%	biaxial	Experiment	[373]
WSe2	RT	Au nanopillars	not reported	biaxial	Experiment	[374]
WSe2	RT	Bendable substrate	1.40%	uniaxial	Experiment & Theory	[116]
WSe2	cryogenic	fiber pressure	not reported	biaxial/pressure	Experiment	[375]
WSe2	RT	bendable substrate	2.1	uniaxial	Experiment	[117]
WSe2	RT	flexible substrate	1.35%	uniaxial	Experiment	[124]
WSe2	RT	tip on bubble		local	Experiment	[376]

Wse2	RT	fabrication induced		uniaxial	Experiment	[377]
WSe2	RT		2%	uniaxial	Experiment	[106]
WSe2	RT	bubble		local	Experiment	[304]
WSe2	RT	patterned substrate		local, biaxial	Experiment	[378]
WSe2	RT	bendable substrate	1.51%	uniaxial	Experiment	[104]
WSe2	cryogenic	nanopartical/patterned substrate		local	Experiment	[129]
WSe2	RT	AFM indentation		local	Experiment	[379]
WSe2	RT	bendable substrate	0.40%	uniaxial	Experiment	[119]
WSe2	RT	??	2.10%	uniaxial	Experiment	[328]
WSe2, WS2	RT	bendable substrate	> 5%	uniaxial	Experiment	[107]
WSe2, WSe2/gr	RT	stretchable substrate	2.40%	uniaxial	Experiment	[380]
WSe2/MoSe2	4K	fabrication induced	not reported	Uniaxial	Experiment	[381]
WSe2/MoSe2	cryogenic	bendable substrate	<0.4%	uniaxial	Experiment	[382]
WSe2/WSe2	RT			biaxial	Theory	[383]
ZnO/WSe2/graphene	RT	nanopillar	4%	biaxial	Experiment	[384]
		NA				[385]
		NA			Theory	[386]
		fabrication induced			Computational	[238]
MoS2	RT	wrinkled substrate	not reported	Uniaxial, local	Experiment	[70]

References

1. Andersen, P. W. More is different. *Science (1979)* **177**, 393–396 (1972).
2. Sanchez-Juarez, J., Granados-Baez, M., Aguilar-Lasserre, A. A. & Cardenas, J. Automated system for the detection of 2D materials using digital image processing and deep learning. *Opt Mater Express* **12**, 1856 (2022).
3. Masubuchi, S. *et al.* Autonomous robotic searching and assembly of two-dimensional crystals to build van der Waals superlattices. *Nat Commun* **9**, 1–12 (2018).
4. Novoselov, K. S. *et al.* Electric field in atomically thin carbon films. *Science (1979)* **306**, 666–669 (2004).
5. Reina, A. *et al.* Transferring and identification of single- and few-layer graphene on arbitrary substrates. *Journal of Physical Chemistry C* **112**, 17741–17744 (2008).
6. Vogl, T., Campbell, G., Buchler, B. C., Lu, Y. & Lam, P. K. Fabrication and Deterministic Transfer of High-Quality Quantum Emitters in Hexagonal Boron Nitride. *ACS Photonics* **5**, 2305–2312 (2018).
7. Cheliotis, I. & Zergioti, I. A review on transfer methods of two-dimensional materials. *2D Materials* vol. 11 022004 Preprint at https://doi.org/10.1088/2053-1583/ad2f43 (2024).
8. Kim, K. *et al.* Van der Waals Heterostructures with High Accuracy Rotational Alignment. *Nano Lett* **16**, 1989–1995 (2016).
9. Wallace, P. R. The band theory of graphite. *Physical Review* **71**, 622–634 (1947).
10. Massabeau, S. *et al.* Evidence of Fermi level pinning at the Dirac point in epitaxial multilayer graphene. *Phys Rev B* **95**, 85311 (2017).
11. Castro Neto, A. H., Guinea, F., Peres, N. M. R., Novoselov, K. S. & Geim, A. K. The electronic properties of graphene. *Rev Mod Phys* **81**, 109–162 (2009).
12. Huang, B. *et al.* Layer-dependent ferromagnetism in a van der Waals crystal down to the monolayer limit. *Nature* **546**, 270–273 (2017).
13. Gong, C. *et al.* Discovery of intrinsic ferromagnetism in two-dimensional van der Waals crystals. *Nature* **546**, 265–269 (2017).
14. Xi, X. *et al.* Ising pairing in superconducting NbSe2 atomic layers. *Nat Phys* **12**, 139–143 (2016).
15. Kim, W. *et al.* Exciton-Sensitized Second-Harmonic Generation in 2D Heterostructures. *ACS Nano* **17**, 20580–20588 (2023).
16. Seyler, K. L. *et al.* Electrical control of second-harmonic generation in a WSe2 monolayer transistor. *Nat Nanotechnol* **10**, 407–411 (2015).

17. Wang, Y. *et al.* Giant All-Optical Modulation of Second-Harmonic Generation Mediated by Dark Excitons. *ACS Photonics* **8**, 2320–2328 (2021).

18. Zhang, M. *et al.* Emergent second-harmonic generation in van der Waals heterostructure of bilayer MoS 2 and monolayer graphene. *Sci Adv* **9**, 1–9 (2023).

19. Li, Y. *et al.* Probing symmetry properties of few-layer MoS2 and h-BN by optical second-harmonic generation. *Nano Lett* **13**, 3329–3333 (2013).

20. Janisch, C. *et al.* Extraordinary second harmonic generation in Tungsten disulfide monolayers. *Sci Rep* **4**, (2014).

21. Yuan, Y. *et al.* Probing the Twist-Controlled Interlayer Coupling in Artificially Stacked Transition Metal Dichalcogenide Bilayers by Second-Harmonic Generation. *ACS Nano* **17**, 17897–17907 (2023).

22. Malard, L. M., Alencar, T. V, Barboza, A. P. M., Mak, K. F. & De Paula, A. M. Observation of intense second harmonic generation from MoS2 atomic crystals. *Phys Rev B Condens Matter Mater Phys* **87**, 201401 (2013).

23. Paradisanos, I. *et al.* Second harmonic generation control in twisted bilayers of transition metal dichalcogenides. (2021).

24. Kourmoulakis, G. *et al.* Strain distribution in WS 2 monolayers detected through Polarization-resolved Second Harmonic Generation.

25. Mennel, L., Paur, M. & Mueller, T. Second harmonic generation in strained transition metal dichalcogenide monolayers: MoS2 , MoSe2 , WS2 , and WSe2. *APL Photonics* **4**, 34404 (2019).

26. Zeng, H. *et al.* Optical signature of symmetry variations and spin-valley coupling in atomically thin tungsten dichalcogenides. *Sci Rep* **3**, 11 (2013).

27. Schaibley, J. R. *et al.* Valleytronics in 2D materials. *Nat Rev Mater* **1**, 1–15 (2016).

28. Vitale, S. A. *et al.* Valleytronics: Opportunities, Challenges, and Paths Forward. *Small* **14**, 1–15 (2018).

29. Mak, K. F., McGill, K. L., Park, J. & McEuen, P. L. The valley Hall effect in MoS2 transistors. *Science (1979)* **344**, 1489–1492 (2014).

30. He, M. *et al.* Valley phonons and exciton complexes in a monolayer semiconductor. *Nat Commun* **11**, 1–7 (2020).

31. Jones, A. M. *et al.* Optical generation of excitonic valley coherence in monolayer WSe 2. *Nat Nanotechnol* **8**, 634–638 (2013).

32. Lee, J., Mak, K. F. & Shan, J. Electrical control of the valley Hall effect in bilayer MoS 2 transistors. *Nat Nanotechnol* **11**, 421–425 (2016).

33. Wang, G. *et al.* Valley dynamics probed through charged and neutral exciton emission in monolayer WSe2. *Phys Rev B* **90**, 075413 (2014).

34. Koperski, M. *et al.* Orbital, spin and valley contributions to Zeeman splitting of excitonic resonances in MoSe2, WSe2 and WS2 Monolayers. *2d Mater* **6**, (2019).

35. Xiao, D., Liu, G. Bin, Feng, W., Xu, X. & Yao, W. Coupled spin and valley physics in monolayers of MoS 2 and other group-VI dichalcogenides. *Phys Rev Lett* **108**, 1–5 (2012).

36. Wang, G. *et al.* Colloquium: Excitons in atomically thin transition metal dichalcogenides. *Rev Mod Phys* **90**, (2018).

37. Xu, X., Yao, W., Xiao, D. & Heinz, T. F. Spin and pseudospins in transition metal dichalcogenides. *Nat Phys* **10**, 343–350 (2014).

38. Wu, F. *et al.* Giant Correlated Gap and Possible Room-Temperature Correlated States in Twisted Bilayer MoS 2. *Phys Rev Lett* **131**, (2023).

39. Iwakiri, S. *et al.* Tunable quantum interferometer for correlated moiré electrons. *Nat Commun* **15**, (2024).

40. Xiong, R. *et al.* Correlated insulator of excitons in WSe2/WS2 moiré superlattices. *Science (1979)* **380**, 860–864 (2023).

41. Ma, L. *et al.* Strongly correlated excitonic insulator in atomic double layers. (2021).

42. Sun, X. *et al.* Correlated states in doubly-aligned hBN/graphene/hBN heterostructures. *Nat Commun* **12**, (2021).

43. Tan, Q. *et al.* Layer-dependent correlated phases in WSe2/MoS2 moiré superlattice. *Nat Mater* **22**, 605–611 (2023).

44. Xu, Y. *et al.* Correlated insulating states at fractional fillings of moiré superlattices. *Nature* **587**, 214–218 (2020).

45. Wang, L. *et al.* Correlated electronic phases in twisted bilayer transition metal dichalcogenides. *Nat Mater* **19**, 861–866 (2020).

46. Anderson, E. *et al.* Programming correlated magnetic states with gate-controlled moiré geometry. *Science (1979)* **381**, 325–330 (2023).

47. Huang, X. *et al.* Correlated insulating states at fractional fillings of the WS2/WSe2 moiré lattice. *Nat Phys* **17**, 715–719 (2021).

48. Li, H. *et al.* Imaging local discharge cascades for correlated electrons in WS2/WSe2 moiré superlattices. *Nat Phys* **17**, 1114–1119 (2021).

49. Chen, D. *et al.* Tuning moiré excitons and correlated electronic states through layer degree of freedom. *Nature Communications 2022 13:1* **13**, 1–8 (2022).

50. Zhang, L. *et al.* Correlated States in Strained Twisted Bilayer Graphenes Away from the Magic Angle. *Nano Lett* **22**, 3204–3211 (2022).

51. Zhang, Z. *et al.* Correlated interlayer exciton insulator in heterostructures of monolayer WSe2 and moiré WS2/WSe2. *Nat Phys* (2022) doi:10.1038/s41567-022-01702-z.

52. Cao, Y. *et al.* Correlated insulator behaviour at half-filling in magic-angle graphene superlattices. *Nature* **556**, 80–84 (2018).

53. Wu, F. *et al.* Coupled ferroelectricity and correlated states in a twisted quadrilayer MoS 2 moiré superlattice. *Chinese Physics Letters* (2023) doi:10.1088/0256-307x/40/4/047303.

54. Liu, E. *et al.* Excitonic and Valley-Polarization Signatures of Fractional Correlated Electronic Phases in a WSe2/WS2 Moiré Superlattice. *Phys Rev Lett* **127**, (2021).

55. Xian, L., Kennes, D. M., Tancogne-Dejean, N., Altarelli, M. & Rubio, A. Multiflat Bands and Strong Correlations in Twisted Bilayer Boron Nitride: Doping-Induced Correlated Insulator and Superconductor. *Nano Lett* **19**, 4934–4940 (2019).

56. Zhou, B. T., Egan, S. & Franz, M. Moiré flat Chern bands and correlated quantum anomalous Hall states generated by spin-orbit couplings in twisted homobilayer MoS 2.

57. Mak, K. F. & Shan, J. Semiconductor moiré materials. *Nat Nanotechnol* **17**, 686–695 (2022).

58. Wilson, N. P., Yao, W., Shan, J. & Xu, X. Excitons and emergent quantum phenomena in stacked 2D semiconductors. *Nature* vol. 599 383–392 Preprint at https://doi.org/10.1038/s41586-021-03979-1 (2021).

59. Liu, Y. *et al.* Moiré superlattices and related moiré excitons in twisted van der Waals heterostructures. *Chemical Society Reviews* vol. 50 6401–6422 Preprint at https://doi.org/10.1039/d0cs01002b (2021).

60. Koblischka, M. R. & Koblischka-Veneva, A. Review of Moiré superconductivity and application of the Roeser-Huber formula. *Superconductivity* vol. 9 100073 Preprint at https://doi.org/10.1016/j.supcon.2023.100073 (2024).

61. Rakib, T., Pochet, P., Ertekin, E. & Johnson, H. T. Moiré engineering in van der Waals heterostructures. *Journal of Applied Physics* vol. 132 120901 Preprint at https://doi.org/10.1063/5.0105405 (2022).

62. He, F. *et al.* Moiré Patterns in 2D Materials: A Review. *ACS Nano* vol. 15 5944–5958 Preprint at https://doi.org/10.1021/acsnano.0c10435 (2021).

63. Kennes, D. M. *et al.* Moiré heterostructures as a condensed-matter quantum simulator. *Nature Physics* vol. 17 155–163 Preprint at https://doi.org/10.1038/s41567-020-01154-3 (2021).

64. Regan, E. C. *et al.* Emerging exciton physics in transition metal dichalcogenide heterobilayers. *Nature Reviews Materials* vol. 7 778–795 Preprint at https://doi.org/10.1038/s41578-022-00440-1 (2022).

65. Li, Z. *et al.* Strain Releasing of Flexible 2D Electronics through van der Waals Sliding Contact. *ACS Nano* **16**, 13152–13159 (2022).

66. Chen, W. *et al.* Improving the strain control performance of MoS 2 monolayer to develop flexible electronics. *Adv Eng Mater* (2023) doi:10.1002/ADEM.202301470.

67. Tsai, M. Y. *et al.* Flexible MoS2 Field-Effect Transistors for Gate-Tunable Piezoresistive Strain Sensors. *ACS Appl Mater Interfaces* **7**, 12850–12855 (2015).

68. Ouyang, D., Zhang, N., Li, Y. & Zhai, T. Emerging Nonplanar van der Waals Nanoarchitectures from 2D Allotropes for Optoelectronics. *Advanced Functional Materials* vol. 33 2208321 Preprint at https://doi.org/10.1002/adfm.202208321 (2023).

69. Zhao, B. *et al.* High-order superlattices by rolling up van der Waals heterostructures. *Nature* **591**, 385–390 (2021).

70. Castellanos-Gomez, A. *et al.* Local strain engineering in atomically thin MoS2. *Nano Lett* **13**, 5361–5366 (2013).

71. Sonelastic. Polymers elastic modulus and Poisson ratio | Sonelastic®. https://www.sonelastic.com/en/fundamentals/tables-of-materials-properties/polymers.html (2016).

72. Polyimide. https://www.mit.edu/~6.777/matprops/polyimide.htm.

73. JR., W. D. C. Modulus Of Elasticity For Metals. *Material Science and Engineering: An Introduction* 1–4 (2007).

74. Kögl, M. *et al.* Moiré straintronics: a universal platform for reconfigurable quantum materials. *NPJ 2D Mater Appl* **7**, (2023).

75. Young's modulus - Wikipedia. https://en.wikipedia.org/wiki/Young%27s_modulus (2022).

76. Yang, S., Chen, Y. & Jiang, C. Strain engineering of two-dimensional materials: Methods, properties, and applications. *InfoMat* vol. 3 397–420 Preprint at https://doi.org/10.1002/inf2.12177 (2021).

77. Bertolazzi, S., Brivio, J. & Kis, A. Stretching and breaking of ultrathin MoS 2. *ACS Nano* **5**, 9703–9709 (2011).

78. Griffits, A. A. The phenomena of rupture and flow in solids. *Masinovedenie* **4**, 9–14 (1995).

79. Hicks, C. W., Barber, M. E., Edkins, S. D., Brodsky, D. O. & Mackenzie, A. P. Piezoelectric-based apparatus for strain tuning. *Review of Scientific Instruments* **85**, 65003 (2014).

80. Vinograd, I. *et al.* Using strain to uncover the interplay between two- and three-dimensional charge density waves in high-temperature superconducting YBa2Cu3Oy. *Nat Commun* **15**, 1–9 (2024).

81. Hicks, C. W. *et al.* Strong increase of Tc of Sr2RuO4under both tensile and compressive strain. *Science* vol. 344 283–285 Preprint at https://doi.org/10.1126/science.1248292 (2014).

82. Malinowski, P. *et al.* Suppression of superconductivity by anisotropic strain near a nematic quantum critical point. *Nat Phys* **16**, 1189–1193 (2020).

83. Peña, T. *et al.* Strain engineering 2D MoS2with thin film stress capping layers. *2d Mater* **8**, 45001 (2021).

84. Gao, X. *et al.* Heterostrain-enabled dynamically tunable moiré superlattice in twisted bilayer graphene. *Sci Rep* **11**, 21402 (2021).

85. Park, M. U. *et al.* Funnel Devices Based on Asymmetrically Strained Transition Metal Dichalcogenides. *Advanced Materials* **35**, 2209788 (2023).

86. Wang, W. & Ma, X. Strain-Induced Trapping of Indirect Excitons in MoSe2/WSe2Heterostructures. *ACS Photonics* **7**, 2460–2467 (2020).

87. Zhang, Y. *et al.* Patternable Process-Induced Strain in 2D Monolayers and Heterobilayers. *ACS Nano* **18**, 4205–4215 (2024).

88. Peña, T. *et al.* Moiré Engineering in 2D Heterostructures with Process-Induced Strain. *ArXiv* **10**, 3480 (2022).

89. Peña, T. *et al.* Temperature and time stability of process-induced strain engineering on 2D materials. *J Appl Phys* **131**, 24304 (2022).

90. Azizimanesh, A. *et al.* Strain engineering in 2D hBN and graphene with evaporated thin film stressors. *Appl Phys Lett* **123**, 43504 (2023).

91. Azizimanesh, A., Peña, T., Sewaket, A., Hou, W. & Wu, S. M. Uniaxial and biaxial strain engineering in 2D MoS2with lithographically patterned thin film stressors. *Appl Phys Lett* **118**, 213104 (2021).

92. Androulidakis, C. *et al.* Strained hexagonal boron nitride: Phonon shift and Grüneisen parameter. *Phys Rev B* **97**, 241414 (2018).

93. He, K., Poole, C., Mak, K. F. & Shan, J. Experimental demonstration of continuous electronic structure tuning via strain in atomically thin MoS2. *Nano Lett* **13**, 2931–2936 (2013).

94. Zhu, C. R. *et al.* Strain tuning of optical emission energy and polarization in monolayer and bilayer MoS2. *Phys Rev B* **88**, 121301 (2013).

95. Frisenda, R. *et al.* Biaxial strain tuning of the optical properties of single-layer transition metal dichalcogenides. *NPJ 2D Mater Appl* **1**, 1–7 (2017).

96. Carrascoso, F., Frisenda, R. & Castellanos-Gomez, A. Biaxial versus uniaxial strain tuning of single-layer MoS2. *Nano Materials Science* **4**, 44–51 (2022).

97. Li, Z. *et al.* Efficient strain modulation of 2D materials via polymer encapsulation. *Nat Commun* **11**, 1–8 (2020).

98. Ren, L. *et al.* Efficient modulation of MoS 2 /WSe 2 interlayer excitons via uniaxial strain. *Appl Phys Lett* **120**, 053107 (2022).

99. Conley, H. J. *et al.* Bandgap engineering of strained monolayer and bilayer MoS2. *Nano Lett* **13**, 3626–3630 (2013).

100. Hu, J. *et al.* Moiré-Assisted Strain Transfer in Vertical van der Waals Heterostructures. *Nano Lett* **23**, 10051–10057 (2023).

101. Yin, Z. *et al.* Directionally-Resolved Phononic Properties of Monolayer 2D Molybdenum Ditelluride (MoTe2) under Uniaxial Elastic Strain. *Nano Lett* **23**, 11763–11770 (2023).

102. Georgoulea, N. C., Power, S. R. & Caffrey, N. M. Strain-induced stacking transition in bilayer graphene. (2022).

103. Dey, A., Azizimanesh, A., Wu, S. M. & Askari, H. Uniaxial Strain-Induced Stacking Order Change in Trilayer Graphene. *ACS Appl Mater Interfaces* (2023) doi:10.1021/acsami.3c19101.

104. Desai, S. B. *et al.* Strain-induced indirect to direct bandgap transition in multilayer WSe 2. *Nano Lett* **14**, 4592–4597 (2014).

105. Mennel, L. *et al.* Band Nesting in Two-Dimensional Crystals: An Exceptionally Sensitive Probe of Strain. *Nano Lett* **20**, 4242–4248 (2020).

106. Tang, N., Du, C., Wang, Q. & Xu, H. Strain engineering in bilayer WSe2 over a large strain range. *Microelectron Eng* **223**, 111202 (2020).

107. Dadgar, A. M. *et al.* Strain Engineering and Raman Spectroscopy of Monolayer Transition Metal Dichalcogenides. *Chemistry of Materials* **30**, 5148–5155 (2018).

108. Carrascoso, F., Li, H., Frisenda, R. & Castellanos-Gomez, A. Strain engineering in single-, bi- and tri-layer MoS2, MoSe2, WS2 and WSe2. *Nano Res* **14**, 1698–1703 (2021).

109. Niehues, I. *et al.* Strain Control of Exciton-Phonon Coupling in Atomically Thin Semiconductors. *Nano Lett* **18**, 1751–1757 (2018).

110. Wu, W. *et al.* Giant Mechano-Optoelectronic Effect in an Atomically Thin Semiconductor. *Nano Lett* **18**, 2351–2357 (2018).

111. Tweedie, M. E. P. *et al.* Inhomogeneous Strain Release during Bending of WS2 on Flexible Substrates. *ACS Appl Mater Interfaces* **10**, 39177–39186 (2018).

112. Yang, S. *et al.* Strain-Dependent Band Splitting and Spin-Flip Dynamics in Monolayer WS2. *Nano Lett* **23**, 11 (2023).

113. Michail, A. *et al.* Tuning the Photoluminescence and Raman Response of Single-Layer WS2 Crystals Using Biaxial Strain. *Journal of Physical Chemistry C* **127**, 3506–3515 (2022).

114. Xu, X. *et al.* Strain regulated interlayer coupling in WSe2/WS2heterobilayer. *Nanotechnology* **33**, (2022).

115. Zhu, M. *et al.* Exchange between Interlayer and Intralayer Exciton in WSe2/WS2Heterostructure by Interlayer Coupling Engineering. *Nano Lett* **22**, 4528–4534 (2022).

116. Schmidt, R. *et al.* Reversible uniaxial strain tuning in atomically thin WSe2. *2d Mater* **3**, 021011 (2016).

117. Aslan, O. B., Deng, M. & Heinz, T. F. Strain tuning of excitons in monolayer WSe2. *Phys Rev B* **98**, 115308 (2018).

118. Yu, Y., Dong, C. D., Binder, R., Schumacher, S. & Ning, C. Z. Strain-Induced Indirect-to-Direct Bandgap Transition, Photoluminescence Enhancement, and Linewidth Reduction in Bilayer MoTe2. *ACS Nano* **17**, 4230–4238 (2023).

119. Hu, W. *et al.* Straining of atomically thin WSe2crystals: Suppressing slippage by thermal annealing. *J Appl Phys* **132**, 085104 (2022).

120. Çakıroğlu, O., Island, J. O., Xie, Y., Frisenda, R. & Castellanos-Gomez, A. An Automated System for Strain Engineering and Straintronics of 2D Materials. *Adv Mater Technol* **8**, 2201091 (2023).

121. Carrascoso, F. *et al.* Improved strain engineering of 2D materials by adamantane plasma polymer encapsulation. *NPJ 2D Mater Appl* **7**, (2023).

122. Roy, S., Yang, X. & Gao, J. Biaxial strain tuned upconversion photoluminescence of monolayer WS2. *Sci Rep* **14**, 3860 (2024).

123. Datye, I. M. *et al.* Strain-Enhanced Mobility of Monolayer MoS2. *Nano Lett* **22**, 8052–8059 (2022).

124. Shen, T., Penumatcha, A. V. & Appenzeller, J. Strain Engineering for Transition Metal Dichalcogenides Based Field Effect Transistors. *ACS Nano* **10**, 4712–4718 (2016).

125. Wang, Y., Cong, C., Qiu, C. & Yu, T. Raman spectroscopy study of lattice vibration and crystallographic orientation of monolayer mos2 under uniaxial strain. *Small* **9**, 2857–2861 (2013).

126. Shan, Y. *et al.* Pristine Interlayer Coupling for Strain Engineering of WS2/WSe2Nanosheet-Based van der Waals Heterostructures. *ACS Appl Nano Mater* **5**, 17986–17994 (2022).

127. Nazzari, D. *et al.* Reliably straining suspended van der Waals heterostructures. *APL Mater* **11**, 111123 (2023).

128. Cai, T. *et al.* Radiative Enhancement of Single Quantum Emitters in WSe2 Monolayers Using Site-Controlled Metallic Nanopillars. *ACS Photonics* **5**, 3466–3471 (2018).

129. Xu, D. D. *et al.* Sub-Diffraction Correlation of Quantum Emitters and Local Strain Fields in Strain-Engineered WSe 2 Monolayers. *Advanced Materials* (2024) doi:10.1002/adma.202314242.

130. Henríquez-Guerra, E. *et al.* Large Biaxial Compressive Strain Tuning of Neutral and Charged Excitons in Single-Layer Transition Metal Dichalcogenides. *ACS Appl Mater Interfaces* **15**, 57369–57378 (2023).

131. From Cannon Balls to Pressure Seals: Graphite for Sealing - EGC Enterprises. https://egcgraphite.com/from-cannon-balls-to-pressure-seals-graphite-for-sealing/.

132. Lubrication by lamellar solids. *Proc R Soc Lond A Math Phys Sci* **243**, 464–482 (1958).

133. Scharf, T. W. & Prasad, S. V. Solid lubricants: A review. *J Mater Sci* **48**, 511–531 (2013).

134. Liu, Y. *et al.* Interlayer friction and superlubricity in single-crystalline contact enabled by two-dimensional flake-wrapped atomic force microscope tips. *ACS Nano* **12**, 7638–7646 (2018).

135. Barabas, A. Z. *et al.* Mechanically reconfigurable van der Waals devices via low-friction gold sliding. *Sci Adv* **9**, 2536 (2023).

136. Lee, C. *et al.* Frictional characteristics of atomically thin sheets. *Science (1979)* **328**, 76–80 (2010).

137. Liao, M. *et al.* UItra-low friction and edge-pinning effect in large-lattice-mismatch van der Waals heterostructures. *Nat Mater* **21**, 47–53 (2022).

138. Vazirisereshk, M. R. Exploring Flatlands: Atomic Scale Characterization of Friction, Adhesion, and Contact of 2D Materials. Preprint at https://escholarship.org/uc/item/0h5312w4 (2021).

139. Fonseca, J. *et al.* Anomalous Second Harmonic Generation from Atomically Thin MnBi2Te4. *Nano Lett* **22**, 10134–10139 (2022).

140. Otrokov, M. M. *et al.* Prediction and observation of an antiferromagnetic topological insulator. *Nature* **576**, 416–422 (2019).

141. Liu, C. *et al.* Robust axion insulator and Chern insulator phases in a two-dimensional antiferromagnetic topological insulator. *Nat Mater* **19**, 522–527 (2020).

142. Ge, J. *et al.* High-Chern-number and high-temperature quantum Hall effect without Landau levels. *Natl Sci Rev* **7**, 1280–1287 (2020).

143. Ovchinnikov, D. *et al.* Intertwined Topological and Magnetic Orders in Atomically Thin Chern Insulator MnBi2Te4. *Nano Lett* **21**, 2544–2550 (2021).

144. Gao, A. *et al.* Layer Hall effect in a 2D topological axion antiferromagnet. *Nature* **595**, (2021).

145. Deng, Y. *et al.* Quantum anomalous Hall effect in intrinsic magnetic topological insulator MnBi2Te4. *Science (1979)* **367**, 895–900 (2020).

146. Yang, S. *et al.* Odd-Even Layer-Number Effect and Layer-Dependent Magnetic Phase Diagrams in MnBi2Te4. *Phys Rev X* **11**, (2021).

147. Yan, J. Q. *et al.* Crystal growth and magnetic structure of MnBi2Te4. *Phys Rev Mater* **3**, (2019).

148. Otrokov, M. M. *et al.* Prediction and observation of an antiferromagnetic topological insulator. *Nature* **576**, 416–422 (2019).

149. Otrokov, M. M. *et al.* Unique Thickness-Dependent Properties of the van der Waals Interlayer Antiferromagnet MnBi2Te4 Films. *Phys Rev Lett* **122**, (2019).

150. Liu, C. *et al.* Robust axion insulator and Chern insulator phases in a two-dimensional antiferromagnetic topological insulator. *Nat Mater* **19**, 522–527 (2020).

151. Ying, Z. *et al.* Experimental evidence for dissipationless transport of the chiral edge state of the high-field Chern insulator in MnBi2Te4 nanodevices. *Phys Rev B* **105**, 85412 (2022).

152. Hu, C. *et al.* Growth, characterization, and Chern insulator state in MnBi2Te4 via the chemical vapor transport method. *Phys Rev Mater* **5**, 124206 (2021).

153. Li, Y. *et al.* Nonlocal Transport and One-dimensional Conduction in the Axion Insulator State of MnBi2Te4. 1–15 (2021).

154. Cai, J. *et al.* Electric control of a canted-antiferromagnetic Chern insulator. *Nat Commun* **13**, (2022).

155. Liu, C. *et al.* Magnetic-field-induced robust zero Hall plateau state in MnBi2Te4 Chern insulator. *Nat Commun* **12**, (2021).

156. Gao, A. *et al.* Layer Hall effect in a 2D topological axion antiferromagnet. *Nature* **595**, 521–525 (2021).

157. Shikin, A. M. *et al.* Nature of the Dirac gap modulation and surface magnetic interaction in axion antiferromagnetic topological insulator MnBi 2Te 4. *Sci Rep* **10**, 15 (2020).

158. Chen, Y. J. *et al.* Topological Electronic Structure and Its Temperature Evolution in Antiferromagnetic Topological Insulator MnBi2Te4. *Phys Rev X* **91**, (2019).

159. Hao, Y. J. *et al.* Gapless Surface Dirac Cone in Antiferromagnetic Topological Insulator MnBi2Te4. *Phys Rev X* **91**, (2019).

160. Yan, J. The elusive quantum anomalous Hall effect in MnBi2Te4: a materials perspective. (2021).

161. Hou, F. *et al.* Te-Vacancy-Induced Surface Collapse and Reconstruction in Antiferromagnetic Topological Insulator MnBi2Te4. *ACS Nano* **14**, 11262–11272 (2020).

162. Lin, Z. *et al.* Magnetism and Its Structural Coupling Effects in 2D Ising Ferromagnetic Insulator VI3. *Nano Lett* **21**, 9180–9186 (2021).

163. Li, T. *et al.* Pressure-controlled interlayer magnetism in atomically thin CrI3. *Nature Materials* vol. 18 1303–1308 Preprint at https://doi.org/10.1038/s41563-019-0506-1 (2019).

164. Song, T. *et al.* Switching 2D magnetic states via pressure tuning of layer stacking. *Nature Materials* vol. 18 1298–1302 Preprint at (2019).

165. Yang, F. *et al.* Tunable Second Harmonic Generation in Twisted Bilayer Graphene. *Matter* **3**, 1361–1376 (2020).

166. Yao, K. *et al.* Enhanced tunable second harmonic generation from twistable interfaces and vertical superlattices in boron nitride homostructures. *Sci Adv* **7**, (2021).

167. Hsu, W. T. *et al.* Second harmonic generation from artificially stacked transition metal dichalcogenide twisted bilayers. *ACS Nano* **8**, 2951–2958 (2014).

168. Schaibley, J. R. *et al.* Directional interlayer spin-valley transfer in two-dimensional heterostructures. *Nat Commun* **7**, 1–6 (2016).

169. Fiebig, M., Fröhlich, D., Krichevtsov, B. B. & Pisarev, R. v. Second harmonic generation and magnetic-dipole-electric-dipole interference in antiferromagnetic Cr2O3. *Phys Rev Lett* **73**, 2127–2130 (1994).

170. Chu, H. *et al.* Linear Magnetoelectric Phase in Ultrathin MnPS3 Probed by Optical Second Harmonic Generation. *Phys Rev Lett* **124**, (2020).

171. Sun, Z. *et al.* Giant nonreciprocal second-harmonic generation from antiferromagnetic bilayer CrI3. *Nature* **572**, 497–501 (2019).

172. Ni, Z. *et al.* Imaging the Néel vector switching in the monolayer antiferromagnet MnPSe3 with strain-controlled Ising order. *Nat Nanotechnol* **16**, 782–787 (2021).

173. Li, H. *et al.* Antiferromagnetic topological insulator MnBi2Te4: Synthesis and magnetic properties. *Physical Chemistry Chemical Physics* **22**, 556–563 (2020).

174. Yan, J. Q. *et al.* Evolution of structural, magnetic, and transport properties in MnBi2-xSbxTe4. *Phys Rev B* **100**, (2019).

175. Pei, C.-Y. *et al.* Pressure-Induced Topological and Structural Phase Transitions in an Antiferromagnetic Topological Insulator. *Chinese Physics Letters* **37**, (2020).

176. Ding, L. *et al.* Crystal and magnetic structures of magnetic topological insulators MnBi2Te4 and MnBi4Te7. *Phys Rev B* **101**, 1–7 (2020).

177. Fei, R., Song, W. & Yang, L. Giant photogalvanic effect and second-harmonic generation in magnetic axion insulators. *Phys Rev B* **102**, 35440 (2020).

178. Hsieh, D. *et al.* Nonlinear optical probe of tunable surface electrons on a topological insulator. *Phys Rev Lett* **106**, (2011).

179. Li, J. *et al.* Intrinsic magnetic topological insulators in van der Waals layered MnBi2Te4-family materials. *Sci Adv* **5**, 1–8 (2019).

180. Lee, K. *et al.* Magnetic Order and Symmetry in the 2D Semiconductor CrSBr. *Nano Lett* **21**, 3511–3517 (2021).

181. McIver, J. W. *et al.* Theoretical and experimental study of second harmonic generation from the surface of the topological insulator Bi 2Se 3. *Phys Rev B Condens Matter Mater Phys* **86**, 35327 (2012).

182. Yan, J.-Q. *et al.* Crystal growth and magnetic structure of ${\rm MnBi}_2{\rm Te}_4$. *Phys Rev Mater* **3**, (2019).

183. Velický, M. *et al.* Mechanism of gold-assisted exfoliation of centimeter-sized transition-metal dichalcogenide monolayers. *ACS Nano* **12**, 10463–10472 (2018).

184. Huang, Y. *et al.* Universal mechanical exfoliation of large-area 2D crystals. *Nat Commun* **11**, (2020).

185. Momma, K. & Izumi, F. VESTA 3 for three-dimensional visualization of crystal, volumetric and morphology data. *J Appl Crystallogr* **44**, 1272–1276 (2011).

186. Deng, Y. *et al.* Quantum anomalous Hall effect in intrinsic magnetic topological insulator MnBi2Te4. *Science (1979)* **367**, 895–900 (2020).

187. Cho, Y. *et al.* Phonon modes and Raman signatures of MnBi2nTe3n+1(n=1,2,3,4) magnetic topological heterostructures. *Phys Rev Res* **4**, (2022).

188. Choe, J. *et al.* Electron-Phonon and Spin-Lattice Coupling in Atomically Thin Layers of MnBi2Te4. *Nano Lett* **21**, 6139–6145 (2021).

189. Yan, J. J.-Q. The elusive quantum anomalous Hall effect in MnBi2Te4: a materials perspective. *ECS Journal of Solid State Science and Technology* **11**, 063007 (2021).

190. Lai, Y., Ke, L., Yan, J., McDonald, R. D. & McQueeney, R. J. Defect-driven ferrimagnetism and hidden magnetization in MnBi2Te4. *Phys Rev B* **103**, 184429 (2021).

191. Wu, X. *et al.* Irremovable Mn-Bi Site Mixing in MnBi2Te4. *Nano Lett* **23**, 5048–5054 (2023).

192. Garnica, M. *et al.* Native point defects and their implications for the Dirac point gap at MnBi2Te4(0001). *NPJ Quantum Mater* **7**, (2022).

193. Huang, Z., Du, M. H., Yan, J. & Wu, W. Native defects in antiferromagnetic topological insulator MnBi2Te4. *Phys Rev Mater* **4**, 121202 (2020).

194. Liu, Y. *et al.* Site Mixing for Engineering Magnetic Topological Insulators. *Phys Rev X* **11**, 021033 (2021).

195. Lüpke, F. *et al.* Anti-site defect-induced disorder in compensated topological magnet MnBi2-xSbxTe4. *Commun Mater* **4**, 1–7 (2023).

196. Ahn, J., Kang, S. H., Yoon, M., Ganesh, P. & Krogel, J. T. Stacking Faults and Topological Properties in MnBi2Te4: Reconciling Gapped and Gapless States. *Journal of Physical Chemistry Letters* **14**, 9052–9059 (2023).

197. Yamanaka, K., Ogiso, H. & Kolosov, O. Ultrasonic force microscopy for nanometer resolution subsurface imaging. *Appl Phys Lett* **64**, 178–180 (1994).

198. Yamanaka, K., Ogiso, H. & Kolosov, O. Analysis of subsurface imaging and effect of contact elasticity in the ultrasonic force microscope. *Jpn J Appl Phys* **33**, 3197–3203 (1994).

199. Thomsen, C., Grahn, H. T., Maris, H. J. & Tauc, J. Surface generation and detection of phonons by picosecond light pulses. *Phys Rev B* **34**, 4129–4138 (1986).

200. Thomsen, C. *et al.* Coherent phonon generation and detection by picosecond light pulses. *Phys Rev Lett* **53**, 989–992 (1984).

201. Lin, H.-N., Stoner, R. J., Maris, H. J. & Tauc, J. Phonon attenuation and velocity measurements in transparent materials by picosecond acoustic interferometry. *J Appl Phys* **69**, 3816–3822 (1991).

202. Thompson, E. *et al.* Picosecond laser ultrasonic measurements of interlayer elastic properties of 2H-MoSe2 and 2H-WSe2. *Mater Today Chem* **18**, (2020).

203. Yan, W. *et al.* Nondestructive Picosecond Ultrasonic Probing of Intralayer and van der Waals Interlayer Bonding in α- and β-In2Se3. *Adv Funct Mater* **31**, (2021).

204. Audoin, B., Perton, M., Chigarev, N. & Rossignol, C. Picosecond acoustic diffraction in anisotropic thin film (νm); Application to the measurement of stiffness coefficients. *J Phys Conf Ser* **92**, 012028 (2007).

205. Von Reppert, A. *et al.* Unconventional picosecond strain pulses resulting from the saturation of magnetic stress within a photoexcited rare earth layer. *Structural Dynamics* **7**, 24303 (2020).

206. Wen, Y. C. *et al.* Elastic stiffness of single-crystalline FeSe measured by picosecond ultrasonics. *J Appl Phys* **110**, 073505 (2011).

207. Wright Oliver B Wright, O. B. *et al.* Ultrasonic Detection from Picosecond Surface Vibrations: Application to Interfacial Layer Detection Spectral response of sulfonated polystyrene photonic crystals with varying concentrations of ethanol Platelet size and density affect shear-induced thrombu. *Jpn J Appl Phys* **128**,.

208. Wright, O. B. & Kawashima, K. Coherent phonon detection from ultrafast surface vibrations. *Phys Rev Lett* **69**, 1668–1671 (1992).

209. Khafizov, M. *et al.* Subsurface imaging of grain microstructure using picosecond ultrasonics. *Acta Mater* **112**, 209–215 (2016).

210. Cuffe, J. *et al.* Lifetimes of confined acoustic phonons in ultrathin silicon membranes. *Phys Rev Lett* **110**, 095503 (2013).

211. Soubelet, P. *et al.* The lifetime of interlayer breathing modes of few-layer 2H-MoSe2 membranes. *Nanoscale* **11**, 10446–10453 (2019).

212. Yoon, Y. *et al.* Terahertz phonon engineering and spectroscopy with van der Waals heterostructures. *ArXiv* 1–22 (2023).

213. Klokov, A. Y. *et al.* 3D Hypersound Microscopy of van der Waals Heterostructures. *Nano Lett* **22**, 2070–2076 (2022).

214. Bartram, F. M. *et al.* Ultrafast coherent interlayer phonon dynamics in atomically thin layers of MnBi2Te4. *NPJ Quantum Mater* **7**, (2022).

215. Zalalutdinov, M. K. *et al.* Acoustic cavities in 2D heterostructures. *Nat Commun* **12**, 1–11 (2021).

216. Matsuda, O., Larciprete, M. C., Li Voti, R. & Wright, O. B. Fundamentals of picosecond laser ultrasonics. *Ultrasonics* **56**, 3–20 (2015).

217. signal-processing.com. Ultrasonic or ultrasound sound velocity and impedance | Signal Processing. https://www.signal-processing.com/table.php.

218. Tang, Y. *et al.* One-way Acoustic Beam Splitter. *Sci Rep* **8**, 1–6 (2018).

219. Padmanabhan, H. *et al.* Interlayer magnetophononic coupling in MnBi2Te4. *Nat Commun* **13**, 1–10 (2022).

220. Bartram, F. M. *et al.* Ultrafast coherent interlayer phonon dynamics in atomically thin layers of MnBi2Te4. *NPJ Quantum Mater* **7**, (2022).

221. Yankowitz, M. *et al.* Emergence of superlattice Dirac points in graphene on hexagonal boron nitride. *Nat Phys* **8**, 382–386 (2012).

222. Zhang, L. *et al.* Twist-angle dependence of moiré excitons in WS2/MoSe2 heterobilayers. *Nat Commun* **11**, 1–8 (2020).

223. Dai, D. *et al.* Twist angle–dependent valley polarization switching in heterostructures. *Sci Adv* **10**, 1281 (2024).

224. Yuan, L. *et al.* Twist-angle-dependent interlayer exciton diffusion in WS2–WSe2 heterobilayers. *Nat Mater* **19**, 617–623 (2020).

225. Nayak, P. K. *et al.* Probing Evolution of Twist-Angle-Dependent Interlayer Excitons in MoSe2/WSe2van der Waals Heterostructures. *ACS Nano* **11**, 4041–4050 (2017).

226. Feng, H. F., Liu, B. & Guo, Z. X. Giant twist-angle dependence of thermal conductivity in bilayer graphene originating from strong interlayer coupling. *Phys Rev B* **108**, (2023).

227. Ke, Y., Wan, L., Qin, X., Hu, W. & Yang, J. Proposed Quantum Twisting Scanning Probe Microscope over Twisted Bilayer Graphene. *Nano Lett* **20**, 53 (2024).

228. Inbar, A. *et al.* The Quantum Twisting Microscope. (2022).

229. Yang, Y. *et al.* In situ manipulation of van der Waals heterostructures for twistronics. *Sci Adv* **6**, (2020).

230. Kapfer, M. *et al.* Programming twist angle and strain profiles in 2D materials. *Science (1979)* **381**, 677–681 (2023).

231. Zheng, H., Zhai, D. & Yao, W. Twist versus heterostrain control of optical properties of moiré exciton minibands. *2d Mater* **8**, 44016 (2021).

232. Rosenberger, M. R. *et al.* Twist Angle-Dependent Atomic Reconstruction and Moiré Patterns in Transition Metal Dichalcogenide Heterostructures. *ACS Nano* **14**, 4550–4558 (2020).

233. Cai, J. *et al.* Signatures of fractional quantum anomalous Hall states in twisted MoTe2. *Nature* **622**, 63–68 (2023).

234. Xu, F. *et al.* Observation of Integer and Fractional Quantum Anomalous Hall Effects in Twisted Bilayer MoTe2. *Phys Rev X* **13**, 031037 (2023).

235. Lau, C. N., Bockrath, M. W., Mak, K. F. & Zhang, F. Reproducibility in the fabrication and physics of moiré materials. *Nature* vol. 602 41–50 Preprint at https://doi.org/10.1038/s41586-021-04173-z (2022).

236. Ochoa, H. & Fernandes, R. M. Degradation of phonons in disordered moiré superlattices.

237. Rhodes, D., Chae, S. H., Ribeiro-Palau, R. & Hone, J. Disorder in van der Waals heterostructures of 2D materials. *Nature Materials* vol. 18 541–549 Preprint at https://doi.org/10.1038/s41563-019-0366-8 (2019).

238. Halbertal, D., Shabani, S., Passupathy, A. N. & Basov, D. N. Extracting the Strain Matrix and Twist Angle from the Moiré Superlattice in van der Waals Heterostructures. *ACS Nano* **16**, 1471–1476 (2022).

239. Purdie, D. G. *et al.* Cleaning interfaces in layered materials heterostructures. *Nat Commun* **9**, (2018).

240. Rosenberger, M. R. *et al.* Nano-"Squeegee" for the Creation of Clean 2D Material Interfaces. *ACS Appl Mater Interfaces* **10**, 10379–10387 (2018).

241. Wang, W. *et al.* Ultra-clean assembly of van der Waals heterostructures. 1–23 (2023).

242. Jin, K. *et al.* Suspended dry pick-up and flip-over assembly for van der Waals heterostructures with ultra-clean surfaces. (2023).

243. Bozovic, I., Logvenov, G., Belca, I., Narimbetov, B. & Sveklo, I. Epitaxial Strain and Superconductivity in L×a2−x×S×rx×C×u×O4 Thin Films. *Phys Rev Lett* **89**, (2002).

244. Sato, H. & Naito, M. Increase in the superconducting transition temperature by anisotropic strain effect in (001) La1.85Sr0.15CuO4 thin films on LaSrAlO4 substrates. *Physica C: Superconductivity and its Applications* **274**, 221–226 (1997).

245. Locquet, J. P. *et al.* Doubling the critical temperature of La1.9Sr0.1CuO4 using epitaxial strain. *Nature* **394**, 453–456 (1998).

246. Si, W., Li, H. C. & Xi, X. X. Strain and oxygenation effects on superconductivity of La1.85Sr0.15CuO4 thin films. *Appl Phys Lett* **74**, 2839–2841 (1999).

247. Lee, C., Wei, X., Kysar, J. W. & Hone, J. Measurement of the elastic properties and intrinsic strength of monolayer graphene. *Science (1979)* **321**, 385–388 (2008).

248. Ren, W. *et al.* Impact of moiré superlattice on atomic stress and thermal transport in van der Waals heterostructures. *Appl Phys Rev* **10**, 41404 (2023).

249. Tang, K., Ru, G., Qi, W. & Liu, W. Moiré pattern effect on sliding friction of two-dimensional materials. *Tribol Int* **180**, 108288 (2023).

250. Dai, Z., Liu, L. & Zhang, Z. Strain Engineering of 2D Materials: Issues and Opportunities at the Interface. *Advanced Materials* **31**, 1805417 (2019).

251. Dai, Z., Lu, N., Liechti, K. M. & Huang, R. Mechanics at the interfaces of 2D materials: Challenges and opportunities. *Curr Opin Solid State Mater Sci* **24**, 100837 (2020).

252. Gao, X., Urbakh, M. & Hod, O. Stick-Slip Dynamics of Moiré Superstructures in Polycrystalline 2D Material Interfaces. *Phys Rev Lett* **129**, (2022).

253. Wang, K. *et al.* Strain Engineering Modulates Graphene Interlayer Friction by Moiré Pattern Evolution. *ACS Appl Mater Interfaces* **11**, 36169–36176 (2019).

254. Kumar, H., Dong, L. & Shenoy, V. B. Limits of Coherency and Strain Transfer in Flexible 2D van der Waals Heterostructures: Formation of Strain Solitons and Interlayer Debonding. *Sci Rep* **5**, (2016).

255. Mohiuddin, T. M. G. *et al.* Uniaxial strain in graphene by Raman spectroscopy: G peak splitting, Grüneisen parameters, and sample orientation. *Phys Rev B Condens Matter Mater Phys* **79**, (2009).

256. Pendharkar, M. *et al.* Torsional Force Microscopy of Van der Waals Moirés and Atomic Lattices. *Proceedings of the National Academy of Sciences* **121**, e2314083121 (2023).

257. McGilly, L. J. *et al.* Visualization of moiré superlattices. *Nat Nanotechnol* **15**, 580–584 (2020).

258. Xu, K. *et al.* Validating the Use of Conductive Atomic Force Microscopy for Defect Quantification in 2D Materials. *ACS Nano* **17**, 24743–24752 (2023).

259. Yu, J. *et al.* Imaging Graphene Moiré Superlattices via Scanning Kelvin Probe Microscopy. *Nano Lett* **21**, 3280–3286 (2021).

260. Vizner Stern, M. *et al. Interfacial Ferroelectricity by van Der Waals Sliding*. http://science.sciencemag.org/.

261. Woods, C. R. *et al.* Charge-polarized interfacial superlattices in marginally twisted hexagonal boron nitride. *Nat Commun* **12**, (2021).

262. de Jong, T. A. *et al.* Imaging moiré deformation and dynamics in twisted bilayer graphene. *Nat Commun* **13**, 1–8 (2022).

263. Edelberg, D., Kumar, H., Shenoy, V., Ochoa, H. & Pasupathy, A. N. Tunable strain soliton networks confine electrons in van der Waals materials. *Nat Phys* **16**, 1097–1102 (2020).

264. Benschop, T. *et al.* Measuring local moiré lattice heterogeneity of twisted bilayer graphene. *Phys Rev Res* **3**, 13153 (2021).

265. Cenker, J. *et al.* Strain-programmable van der Waals magnetic tunnel junctions. (2023).

266. Laturia, A., Van de Put, M. L. & Vandenberghe, W. G. Dielectric properties of hexagonal boron nitride and transition metal dichalcogenides: from monolayer to bulk. *NPJ 2D Mater Appl* **2**, 1–7 (2018).

267. Dean, C. R. *et al.* Boron nitride substrates for high-quality graphene electronics. *Nat Nanotechnol* **5**, 722–726 (2010).

268. Piezo Hysteresis, Resolution, Polarity, Stiffness – Piezosystem. https://www.piezosystem.com/piezopedia/properties-and-performance/.

269. Rouvière, J. L. & Sarigiannidou, E. Theoretical discussions on the geometrical phase analysis. *Ultramicroscopy* **106**, 1–17 (2005).

270. Hytch, M. J., International, S. M., National, C. & Scientifique, D. R. Geometric Phase Analysis of High Resolution Electron Microscope Images. *Scanning Microsc* **11**, 53–66 (1997).

271. Pásztor, Á., Pushkarna, I. & Renner, C. Delusive chirality and periodic strain pattern in moiré systems. *2d Mater* (2024) doi:10.1088/2053-1583/ad3cea.

272. Hÿtch, M. J., Snoeck, E. & Kilaas, R. Quantitative measurement of displacement and strain fields from HREM micrographs. *Ultramicroscopy* **74**, 131–146 (1998).

273. Chu, J. H. *et al.* In-plane resistivity anisotropy in an underdoped iron arsenide superconductor. *Science (1979)* **329**, 824–826 (2010).

274. Chu, J. H., Kuo, H. H., Analytis, J. G. & Fisher, I. R. Divergent nematic susceptibility in an iron arsenide superconductor. *Science (1979)* **337**, 710–712 (2012).

275. Ikhlas, M. *et al.* Piezomagnetic switching of the anomalous Hall effect in an antiferromagnet at room temperature. *Nat Phys* **18**, 1086–1093 (2022).

276. Yu, Y. *et al.* High-temperature superconductivity in monolayer Bi2Sr2CaCu2O8+δ. *Nature* **575**, 156–163 (2019).

277. Deng, Y. *et al.* Quantum anomalous Hall effect in intrinsic magnetic topological insulator MnBi2Te4. *Science (1979)* **367**, 895–900 (2020).

278. Fernandes, R. M. & Venderbos, J. W. F. Nematicity with a twist: Rotational symmetry breaking in a moiré superlattice. *Sci Adv* **6**, (2020).

279. Xie, M., Pan, H., Wu, F. & Das Sarma, S. Nematic Excitonic Insulator in Transition Metal Dichalcogenide Moiré Heterobilayers. *Phys Rev Lett* **131**, 046402 (2023).

280. Chen, L., Hu, H. & Si, Q. Fragile Insulator and Electronic Nematicity in a Graphene Moire System. (2020).

281. Hwangbo, K. *et al.* Strain Tuning Three-state Potts Nematicity in a Correlated Antiferromagnet. (2023).

282. Tang, Y. *et al.* Evidence of frustrated magnetic interactions in a Wigner–Mott insulator. *Nat Nanotechnol* **18**, 233–237 (2023).

283. Ciorciaro, L. *et al.* Kinetic magnetism in triangular moiré materials. *Nature* **623**, 509–513 (2023).

284. Wang, X. *et al.* Light-induced ferromagnetism in moiré superlattices. *Nature* **604**, 468–473 (2022).

285. Zeng, Y. *et al.* Thermodynamic evidence of fractional Chern insulator in moiré MoTe2. *Nature* **622**, 69–73 (2023).

286. Lu, Z. *et al.* Fractional Quantum Anomalous Hall Effect in a Graphene Moire Superlattice. (2023).

287. Li, T. *et al.* Quantum anomalous Hall effect from intertwined moiré bands. *Nature* **600**, 641–646 (2021).

288. Serlin, M. *et al.* Intrinsic quantized anomalous Hall effect in a moiré heterostructure. *Science (1979)* **367**, 900–903 (2020).

289. Cadiz, F. *et al.* Excitonic linewidth approaching the homogeneous limit in MoS2-based van der Waals heterostructures. *Phys Rev X* **7**, 021026 (2017).

290. Cao, Y. *et al.* Quality Heterostructures from Two-Dimensional Crystals Unstable in Air by Their Assembly in Inert Atmosphere. *Nano Lett* **15**, 4914–4921 (2015).

291. Gong, L. *et al.* Optimizing the reinforcement of polymer-based nanocomposites by graphene. *ACS Nano* **6**, 2086–2095 (2012).

292. Wang, L. *et al.* In Situ Strain Tuning in hBN-Encapsulated Graphene Electronic Devices. *Nano Lett* **19**, 4097–4102 (2019).

293. Cenker, J. *et al.* Reversible strain-induced magnetic phase transition in a van der Waals magnet. *Nat Nanotechnol* **17**, 256–261 (2022).

294. Matt Gilbert, S. *et al.* Alternative stacking sequences in hexagonal boron nitride. *ArXiv* 1–26 (2018).

295. Ghiasi, T. S. *et al.* Electrical and thermal generation of spin currents by magnetic bilayer graphene. *Nat Nanotechnol* **16**, 788–794 (2021).

296. Tseng, C. C. *et al.* Gate-Tunable Proximity Effects in Graphene on Layered Magnetic Insulators. *Nano Lett* **22**, 8495–8501 (2022).

297. Wang, J. *et al.* High-κ van der Waals Oxide MoO3 as Efficient Gate Dielectric for MoS2 Field-Effect Transistors. *Materials* **15**, 5859 (2022).

298. Andres-Penares, D., Brotons-Gisbert, M., Bonato, C., Sánchez-Royo, J. F. & Gerardot, B. D. Optical and dielectric properties of MoO3nanosheets for van der Waals heterostructures. *Appl Phys Lett* **119**, 223104 (2021).

299. Zhang, C. *et al.* Single-crystalline van der Waals layered dielectric with high dielectric constant. *Nat Mater* **22**, 832–837 (2023).

300. Li, T. *et al.* A native oxide high-κ gate dielectric for two-dimensional electronics. *Nat Electron* **3**, 473–478 (2020).

301. Paur, M. *et al.* Electroluminescence from multi-particle exciton complexes in transition metal dichalcogenide semiconductors. *Nat Commun* **10**, 1–7 (2019).

302. Van Tuan, D., Shi, S. F., Xu, X., Crooker, S. A. & Dery, H. Six-Body and Eight-Body Exciton States in Monolayer WSe2. *Phys Rev Lett* **129**, (2022).

303. Barbone, M. *et al.* Charge-tuneable biexciton complexes in monolayer WSe2. *Nat Commun* **9**, 1–6 (2018).

304. Darlington, T. P. *et al.* Imaging strain-localized excitons in nanoscale bubbles of monolayer WSe2 at room temperature. *Nat Nanotechnol* **15**, 854–860 (2020).

305. Wang, F. *et al.* Strain engineering in monolayer WS2 and WS2 nanocomposites. *2d Mater* **7**, (2020).

306. Aas, S. & Bulutay, C. Strain dependence of photoluminescence and circular dichroism in transition metal dichalcogenides: a k · p analysis. *Opt Express* **26**, 28672 (2018).

307. Feierabend, M., Morlet, A., Berghäuser, G. & Malic, E. Impact of strain on the optical fingerprint of monolayer transition-metal dichalcogenides. *Phys Rev B* **96**, 045425 (2017).

308. An, Z. *et al.* Strain control of exciton and trion spin/valley relaxation time in monolayer transition metal dichalcogenides. *to be submitted.* (2023).

309. Scheie, A. *et al.* Spin Waves and Magnetic Exchange Hamiltonian in CrSBr. *Advanced Science* **9**, (2022).

310. Tang, Y. *et al.* Simulation of Hubbard model physics in WSe2/WS2 moiré superlattices. *Nature* **579**, 353–358 (2020).

311. Wang, X. *et al.* Intercell Moir\'e Exciton Complexes in Electron Lattices. 1–14 (2022).

312. Xu, Y. *et al.* Correlated insulating states at fractional fillings of moiré superlattices. *Nature* **587**, 214–218 (2020).

313. Jin, C. *et al.* Stripe phases in WSe2/WS2 moiré superlattices. *Nat Mater* **20**, 940–944 (2021).

314. Xie, Y. M., Zhang, C. P., Hu, J. X., Mak, K. F. & Law, K. T. Valley-Polarized Quantum Anomalous Hall State in Moiré MoTe2/WSe2 Heterobilayers. *Phys Rev Lett* **128**, (2022).

315. Wang, Y. *et al.* Strain-Sensitive Magnetization Reversal of a van der Waals Magnet. *Advanced Materials* **32**, (2020).

316. Chu, J. H. *et al.* In-plane resistivity anisotropy in an underdoped iron arsenide superconductor. *Science (1979)* **329**, 824–826 (2010).

317. Mutch, J. *et al.* Evidence for a strain-tuned topological phase transition in ZrTe5. *Sci Adv* **5**, (2019).

318. Du, L. *et al.* Engineering symmetry breaking in 2D layered materials. *Nature Reviews Physics* vol. 3 193–206 Preprint at https://doi.org/10.1038/s42254-020-00276-0 (2021).

319. Pető, J. *et al.* Moderate strain induced indirect bandgap and conduction electrons in MoS2 single layers. *NPJ 2D Mater Appl* **3**, (2019).

320. Conley, H. J. *et al.* Bandgap engineering of strained monolayer and bilayer MoS2. *Nano Lett* **13**, 3626–3630 (2013).

321. He, K., Poole, C., Mak, K. F. & Shan, J. Experimental demonstration of continuous electronic structure tuning via strain in atomically thin MoS2. *Nano Lett* **13**, 2931–2936 (2013).

322. Lee, J., Wang, Z., Xie, H., Mak, K. F. & Shan, J. Valley magnetoelectricity in single-layer MoS 2. *Nat Mater* **16**, 887–891 (2017).

323. Cosma, D. A., Wallbank, J. R., Cheianov, V. & Fal'Ko, V. I. Moiré pattern as a magnifying glass for strain and dislocations in van der Waals heterostructures. *Faraday Discuss* **173**, 137–143 (2014).

324. Tong, Q. *et al.* Topological mosaics in moiré superlattices of van der Waals heterobilayers. *Nat Phys* **13**, 356–362 (2017).

325. Adinehloo, D., Hendrickson, J. R. & Perebeinos, V. Wetting and strain engineering of 2D materials on nanopatterned substrates. *Nanoscale Adv* (2024) doi:10.1039/d3na01079a.

326. Quan, J. *et al.* Quantifying Strain in Moiré Superlattice. *Nano Lett* **23**, 11510–11516 (2023).

327. Peña, T. *et al.* Moiré Engineering in 2D Heterostructures with Process-Induced Strain. *ArXiv* **10**, 3480 (2022).

328. Aslan, O. B., Deng, M., Brongersma, M. L. & Heinz, T. F. Strained bilayer WSe2 with reduced exciton-phonon coupling. *Phys Rev B* **101**, 115305 (2020).

329. Du, L. *et al.* Engineering symmetry breaking in 2D layered materials. *Nature Reviews Physics* vol. 3 193–206 Preprint at https://doi.org/10.1038/s42254-020-00276-0 (2021).

330. Roldán, R., Castellanos-Gomez, A., Cappelluti, E. & Guinea, F. *Strain Engineering in Semiconducting Two-Dimensional Crystals*. *Journal of Physics Condensed Matter* vol. 27 313201 (IOP Publishing, 2015).

331. Diederich, G. M. *et al.* Tunable Exciton-Hybridized Magnon Interactions in a Layered Semiconductor. *Nat Nanotechnol* **18**, 23–28 (2022).

332. Dong, X. *et al.* Exploring the high dielectric performance of Bi2SeO5: from bulk to bilayer and monolayer. *Sci China Mater* **67**, 906–913 (2024).

333. Park, H. *et al.* Dipole ladders with large Hubbard interaction in a moiré exciton lattice. *Nat Phys* **19**, 1286–1292 (2023).

334. Li, H. *et al.* Imaging moiré flat bands in three-dimensional reconstructed WSe2/WS2 superlattices. *Nat Mater* **20**, 945–950 (2021).

335. Susarla, S. *et al.* Hyperspectral imaging of exciton confinement within a moiré unit cell with a subnanometer electron probe. *Science (1979)* **378**, 1235–1239 (2022).

336. Wang, X. *et al.* Moiré trions in MoSe2/WSe2 heterobilayers. *Nat Nanotechnol* **16**, 1208–1213 (2021).

337. Liu, E. *et al.* Signatures of moiré trions in WSe2/MoSe2 heterobilayers. *Nature* **594**, 46–50 (2021).

338. Marcellina, E. *et al.* Evidence for Moiré Trions in Twisted MoSe 2 Homobilayers. *Nano Lett* **21**, 4461–4468 (2021).

339. Wu, B. *et al.* Evidence for moiré intralayer excitons in twisted WSe2/WSe2 homobilayer superlattices. *Light Sci Appl* **11**, 1–8 (2022).

340. Antão, T. V. C. & Peres, N. M. R. Strain Engineering of Photo-induced Topological Phases in 2D Ferromagnets. (2023).

341. Qiu, W. X., Li, B., Luo, X. J. & Wu, F. Interaction-Driven Topological Phase Diagram of Twisted Bilayer MoTe2. *Phys Rev X* **13**, (2023).

342. Anderson, E. *et al.* Programming correlated magnetic states with gate-controlled moiré geometry. *Science (1979)* **381**, 325–330 (2023).

343. Wang, Y., Lou, C., Zhao, B., Ma, C. & Zhang, J. Doping- and strain-tuned high Curie temperature half-metallicity and quantum anomalous Hall effect in monolayer NiAl2 S4 with non-Dirac and Dirac states. *Phys Rev B* **107**, (2023).

344. Iordanidou, K. *et al.* Electric Field and Strain Tuning of 2D Semiconductor van der Waals Heterostructures for Tunnel Field-Effect Transistors. *ACS Appl Mater Interfaces* **15**, 1762–1771 (2022).

345. O'Haver, T. C. Interactive Peak Fitter. (computer code) Preprint at https://terpconnect.umd.edu/~toh/spectrum/InteractivePeakFitter.htm (2019).

346. Zernike, F. & Midwinter, J. E. Nonlinear optics. in *Applied Nonlinear Optics* 25–53 (John Wiley and Sons, New York, 1973). doi:10.1007/BF00687147.

347. Bykov, A. Y., Murzina, T. v, Olivier, N., Wurtz, G. A. & Zayats, A. v. Coherent lattice dynamics in topological insulator Bi2 Te3 probed with time-resolved optical second-harmonic generation. *Phys Rev B Condens Matter Mater Phys* **92**, 64305 (2015).

348. Liu, Z. *et al.* Continuously tunable uniaxial strain control of van der Waals heterostructure devices. (2024).

349. Varghese, A. *et al.* Electrically Controlled Reversible Strain Modulation in MoS2 Field-effect Transistors via an Electro-mechanically Coupled Piezoelectric Thin Film. (2023).

350. Lloyd, D. *et al.* Band Gap Engineering with Ultralarge Biaxial Strains in Suspended Monolayer MoS2. *Nano Lett* **16**, 5836–5841 (2016).

351. Yang, L. *et al.* Lattice strain effects on the optical properties of MoS2 nanosheets. *Sci Rep* **4**, 1–7 (2014).

352. Chen, Y. *et al.* Mobility Enhancement of Strained MoS2 Transistor on Flat Substrate. *ACS Nano* **17**, 14954–14962 (2023).

353. Wang, S., Ukhtary, M. S. & Saito, R. Strain effect on circularly polarized electroluminescence in transition metal dichalcogenides. *Phys Rev Res* **2**, 33340 (2020).

354. Christopher, J. W. *et al.* Monolayer MoS2 Strained to 1.3% with a microelectromechanical system. *Journal of Microelectromechanical Systems* **28**, 254–263 (2019).

355. Shin, H. *et al.* Nonconventional Strain Engineering for Uniform Biaxial Tensile Strain in MoS2 Thin Film Transistors. *ACS Nano* **18**, 4414–4423 (2024).

356. Liang, J. *et al.* Shear-strain-induced two-dimensional slip avalanches in rhombohedral MoS 2.

357. Cho, C. *et al.* Highly Strain-Tunable Interlayer Excitons in MoS2/WSe2Heterobilayers. *Nano Lett* **21**, 3956–3964 (2021).

358. Li, L. L., Gillen, R., Palummo, M., Milošević, M. V. & Peeters, F. M. Strain tunable interlayer and intralayer excitons in vertically stacked MoSe2/WSe2 heterobilayers. *Appl Phys Lett* **123**, 33102 (2023).

359. Shafi, A. M. *et al.* Strain Engineering for Enhancing Carrier Mobility in MoTe2 Field-Effect Transistors. *Advanced Science* **10**, (2023).

360. Song, S. *et al.* Room Temperature Semiconductor-Metal Transition of MoTe2 Thin Films Engineered by Strain. *Nano Lett* **16**, 188–193 (2016).

361. Qi, Y. *et al.* Recent Progress in Strain Engineering on Van der Waals 2D Materials: Tunable Electrical, Electrochemical, Magnetic and Optical Properties. *Advanced Materials* 2205714 (2022) doi:10.1002/adma.202205714.

362. Celebonovic, V. Strain tunable conductivity and reflectivity of low dimensional systems within the Hubbard model. in *Journal of Physics: Conference Series* vol. 2436 12010 (IOP Publishing, 2023).

363. Cosma, D. A., Wallbank, J. R., Cheianov, V. & Fal'Ko, V. I. Moiré pattern as a magnifying glass for strain and dislocations in van der Waals heterostructures. *Faraday Discuss* **173**, 137–143 (2014).

364. Khatibi, Z. *et al.* Impact of strain on the excitonic linewidth in transition metal dichalcogenides. *2d Mater* **6**, 015015 (2019).

365. Glazov, M. M. *et al.* Exciton fine structure splitting and linearly polarized emission in strained transition-metal dichalcogenide monolayers. *Phys Rev B* **106**, (2022).

366. Peelaers, H. & Van De Walle, C. G. Effects of strain on band structure and effective masses in MoS2. *Phys Rev B Condens Matter Mater Phys* **86**, 241401 (2012).

367. Chang, C.-H., Fan, X., Lin, S.-H. & Kuo, J.-L. Orbital analysis of electronic structure and phonon dispersion in MoS 2 , MoSe 2 , WS 2 , and WSe 2 monolayers under strain. *Phys Rev B* **88**, 195420 (2013).

368. Yun, W. S., Han, S. W., Hong, S. C., Kim, I. G. & Lee, J. D. Thickness and strain effects on electronic structures of transition metal dichalcogenides: 2H-MX 2 semiconductors (M = Mo, W; X = S, Se, Te). *Phys Rev B Condens Matter Mater Phys* **85**, 33305 (2012).

369. Sinner, A., Pantaleón, P. A. & Guinea, F. Strain-Induced Quasi-1D Channels in Twisted Moiré Lattices. *Phys Rev Lett* **131**, (2023).

370. Bi, Z., Yuan, N. F. Q. & Fu, L. Designing flat bands by strain. *Phys Rev B* **100**, 35448 (2019).

371. Bensmann, J. *et al.* Nanoimprint strain-engineering of 2D semiconductors. (2022).

372. Li, K.-H. *et al. Strain-Dependent Structural and Electronic Reconstructions in Long-Wavelength WS2 Moiré Superlattices*.

373. López, P. H. *et al.* Strain control of hybridization between dark and localized excitons in a 2D semiconductor. (2022).

374. Zheng, H. *et al.* Strain-tunable valley polarization and localized excitons in monolayer WSe 2. *Opt Lett* **48**, 2393 (2023).

375. Gelly, R. J. *et al.* Probing dark exciton navigation through a local strain landscape in a WSe2 monolayer. *Nat Commun* **13**, 1–19 (2022).

376. Hasz, K., Hu, Z., Park, K. D. & Raschke, M. B. Tip-Enhanced Dark Exciton Nanoimaging and Local Strain Control in Monolayer WSe2. *Nano Lett* **23**, 198–204 (2023).

377. Wang, Q. *et al.* Highly Polarized Single Photons from Strain-Induced Quasi-1D Localized Excitons in WSe2. *Nano Lett* **21**, 7175–7182 (2021).

378. Chen, Z., Luo, W., Liang, L., Ling, X. & Swan, A. K. Charge Separation in Monolayer WSe2by Strain Engineering: Implications for Strain-Induced Diode Action. *ACS Appl Nano Mater* **5**, 15095–15101 (2022).

379. So, J. P. *et al.* Electrically driven strain-induced deterministic single-photon emitters in a van der Waals heterostructure. *Sci Adv* **7**, (2021).

380. Han, J. *et al.* The Effect of the Pre-Strain Process on the Strain Engineering of Two-Dimensional Materials and Their van der Waals Heterostructures. *Nanomaterials* **13**, 833 (2023).

381. Bai, Y. *et al.* Excitons in strain-induced one-dimensional moiré potentials at transition metal dichalcogenide heterojunctions. *Nat Mater* **19**, 1068–1073 (2020).

382. Ge, A. *et al.* Unraveling the strain tuning mechanism of interlayer excitons in WSe2/MoSe2 heterostructure. *Nanotechnology* **35**, (2024).

383. Gao, Y., Xu, Q., Farooq, M. U., Xian, L. & Huang, L. Switching the Moiré Lattice Models in the Twisted Bilayer WSe2 by Strain or Pressure. *Nano Lett* **23**, 7921–7926 (2023).

384. Zeng, H. *et al.* Gradient-Strained Van Der Waals Heterojunctions for High-Efficient Photodetectors. *Adv Funct Mater* (2024) doi:10.1002/adfm.202400712.

385. Miao, F., Liang, S. J. & Cheng, B. Straintronics with van der Waals materials. *NPJ Quantum Mater* **6**, 2–5 (2021).

386. Iakovlev, Z. A. & Glazov, M. M. Fermi polaron fine structure in strained van der Waals heterostructures. *2d Mater* **10**, (2023).